Advancing Cathode Materials for Next-Generation Li/Na-ion Batteries: Transition-Metal Migration in Disordered Rock-Salts and Layered Oxides

Hang Xu

St Cross College

University of Oxford

A thesis submitted for the degree of
Doctor of Philosophy

Trinity 2025

Abstract

The development of next-generation rechargeable batteries hinges on advanced cathode materials with high capacity, stability, and efficiency. This thesis systematically investigates the structural and redox mechanisms that dictate the electrochemical performance of layered oxides and disordered rock-salt (DRX) compounds for Li- and Na-ion batteries. Layered oxides remain the most industrially mature and energy-dense cathodes, while DRX materials offer a promising alternative with higher compositional flexibility, stronger structural robustness, and the potential to access multi-electron redox reactions beyond the limits of conventional layered frameworks.

Firstly, in representative layered systems, $Na_{0.52}Li_{0.2}Mn_{0.8}O_2$ and its Li-exchanged analogue $Li_{0.56}Li_{0.2}Mn_{0.8}O_2$, the structural and electrochemical implications of transition metal (TM) migration are systematically investigated. A novel electrochemical descriptor "ΔP", is defined to investigate the relationship between electrochemical behavior, local structural transformations, and TM migration kinetics.

Secondly, in Mn-based DRX systems, $Li_2Mn_{0.75}W_{0.25}O_2F$ is studied compared to Li_2MnO_2F, revealing that high-valent d^0 cation W^{6+} simultaneously boost Mn redox activity with enhanced cycling stability and modulate local spinel ordering, at the cost of Li accessible sites and diffusion kinetics, evidenced by Monte Carlo simulations and spectroscopy

Finally, a comparative study of Ni-based DRXs, $Li_{1.2}Ni_{0.4}Nb_{0.4}O_2$ and $Li_{1.2}Ni_{0.5}W_{0.3}O_2$, reveals that the choice of d^0 cation significantly influences redox mechanisms and voltage hysteresis. LNNO supports cooperative Ni and O redox with minimal oxygen loss and low hysteresis, while LNWO exhibits limited Ni redox, higher voltage hysteresis, and irreversible O_2 release. Band structure analysis highlights the importance of cation electronegativity and charge transfer energy in stabilizing oxygen redox.

These insights provide mechanistic guidelines for designing robust cathode materials, advancing the development of high-capacity, low-hysteresis Li/Na-ion batteries.

Advancing Cathode Materials for Next-Generation Li/Na-ion Batteries: Transition-Metal Migration in Disordered Rock-Salts and Layered Oxides

Hang Xu
St Cross College
University of Oxford

A thesis submitted for the degree of
Doctor of Philosophy
Trinity 2025

Acknowledgements

Personal

First and foremost, I would like to express my deepest gratitude to my supervisor, Professor Sir Peter Bruce, for your exceptional insight, academic rigor, and unwavering support throughout my doctoral journey. You provided me incredible lab resources and supporting access to world-class synchrotron facilities which made this thesis possible.

I am also sincerely thankful to Professor Robert House for your mentorship and support during my PhD. Your sharp scientific insight, constructive feedback, and readiness to help have been a great source of inspiration. I would like to thank Dr. John-Joseph Marie and Dr. Liquan Pi for their early guidance and support, and Dr. Mikkel Juelsholt for advice on scattering techniques. I am also grateful to Dr. Gregory Rees for his assistance with NMR measurements.

I owe my deepest gratitude to Dr. Jun Chen for your incredible support and companionship throughout my PhD. I have learned so much from you about electron microscopy, beamtime preparation, and the practicalities of daily lab work. Dr. Yi Yuan, a lovely person and an outstanding collaborator, you have always offered valuable advice on electron microscopy and inspired me with creative solutions in the lab which made a real difference to my projects. Special thanks to Dr. De Sousa Coutinho for your support and critical advice at difficult times in my projects. Dr. Xueyan Hou, it was a pleasure working with you. Your expertise in coding and data analysis has inspired me to develop new skills. Dr. Longlong Wang, thank you for your continuous help with beam time and lab work, which was crucial for my projects.

It has been a great fortune to work alongside so many talented and helpful colleagues, including Dr Tammy Nimmo, Prof. Hui Gao, Professor Laidong Zhou, Chloe Chau, Yuan

Quan, Lechen Yang, Rui Qi, Dr. Daniel Dewar and Dr. Mingzhi Cai, all of whom have provided me with important help, both directly and indirectly, at critical points in my experiments.

I would like to thank my parents for their unwavering love and support throughout my life. Their unconditional care has given me the freedom to pursue my dreams and explore the world on my own terms. To my dearest Yeye, meeting you at neutron school in Oxford was an incredible stroke of luck. We have shared discussions about stacking faults, conversations about music and films, and journeys to many corners of the world. I look forward to discovering even more beautiful places together with you in the future.

Last but not least, I want to thank myself for not giving up during these four challenging years of my PhD. This has been far more than a journey of learning academic knowledge but also a profound journey of self-discovery.

Institutional

I thank the Diamond Light Source for the award of beam time as part of the Energy Materials Block Allocation Group SP14239. Thanks to Chien-Te Chen and Zhiwei Hu from TLS-11A, and to Chih-Wen Pao and Wei-Hsiang Huang from TPS-44A. Thanks to the CAESR SRF and Dr. William Myers (Scientific Applications Manager) for EPR measurement assistance. Thanks to Dr. Hiroki Suga from Spring-8 BL27SU as the local contact for the valuable support and assistance. Thanks to Dr. Henry Fischer from ILL-D4 as local contact for experimental training and help with data processing.

This thesis contains work carried out by the author in collaboration with several colleagues and facilities. Where measurements or sample preparation were performed by collaborators or external services, this is explicitly stated in the relevant chapters. In all cases, the analysis and scientific interpretation were either led or performed by the author unless otherwise noted.

Abstract

The development of next-generation rechargeable batteries hinges on advanced cathode materials with high capacity, stability, and efficiency. This thesis systematically investigates the structural and redox mechanisms that dictate the electrochemical performance of layered oxides and disordered rock-salt (DRX) compounds for Li- and Na-ion batteries. Layered oxides remain the most industrially mature and energy-dense cathodes, while DRX materials offer a promising alternative with higher compositional flexibility, stronger structural robustness, and the potential to access multi-electron redox reactions beyond the limits of conventional layered frameworks.

Firstly, in representative layered systems, $Na_{0.52}Li_{0.2}Mn_{0.8}O_2$ and its Li-exchanged analogue $Li_{0.56}Li_{0.2}Mn_{0.8}O_2$, the structural and electrochemical implications of transition metal (TM) migration are systematically investigated. A novel electrochemical descriptor "ΔP", is defined to investigate the relationship between electrochemical behavior, local structural transformations, and TM migration kinetics.

Secondly, in Mn-based DRX systems, $Li_2Mn_{0.75}W_{0.25}O_2F$ is studied compared to Li_2MnO_2F, revealing that high-valent d^0 cation W^{6+} simultaneously boost Mn redox activity with enhanced cycling stability and modulate local spinel ordering, at the cost of Li accessible sites and diffusion kinetics, evidenced by Monte Carlo simulations and spectroscopy.

Finally, a comparative study of Ni-based DRXs, $Li_{1.2}Ni_{0.4}Nb_{0.4}O_2$ and $Li_{1.2}Ni_{0.5}W_{0.3}O_2$, reveals that the choice of d^0 cation significantly influences redox mechanisms and voltage hysteresis. LNNO supports cooperative Ni and O redox with minimal oxygen loss and low hysteresis, while LNWO exhibits limited Ni redox, higher voltage hysteresis, and irreversible O_2 release. Band structure analysis highlights the importance of cation electronegativity and charge transfer energy in stabilizing oxygen redox.

These insights provide mechanistic guidelines for designing robust cathode materials, advancing the development of high-capacity, low-hysteresis Li/Na-ion batteries.

Contents

List of Figures

List of Tables

List of Abbreviations

ABF-STEM	Annular Bright Field-Scanning Transmission Electron Microscopy
ADF-STEM	Annular Dark Field-Scanning Transmission Electron Microscopy
AM	Alkali metal
CEI	Cathode electrolyte interphase
DEMS	Differential Electrochemical Mass Spectroscopy
DMC	Dimethyl carbonate
DRX	Disordered rock-salt
EC	Ethylene carbonate
EDX	Energy-dispersive X-ray spectroscopy
EMC	Ethyl methyl carbonate
EPR	Electron Paramagnetic Resonance
EXAFS	Extended X-ray Absorption Fine Structure
FD	Full discharge
FEC	Fluoroethylene carbonate
ICP-OES	Inductively Coupled Plasma-Optical Emission Spectrometry
IPFY	Inverse Partial Fluorescence Yield
ISE	Ion-selective electrode
LIBs	lithium-ion batteries
LMOF	Li_2MnO_2F

LMWOF	$Li_2Mn_{0.75}W_{0.25}O_2F$
LNNO	$Li_{1.2}Ni_{0.4}Nb_{0.4}O_2$
LNWO	$Li_{1.2}Ni_{0.5}W_{0.3}O_2$
MAS-NMR	Magic Angle Spinning-Nuclear Magnetic Resonance
NPDF	Neutron Pair Distribution Function
PND	Powder Neutron Diffraction
PTFE	Polytetrafluoroethylene
PXRD	Powder X-ray Diffraction
RIXS	Resonant Inelastic X-ray Spectroscopy
SAED	Selected Area Electron Diffraction
SEM	Scanning Electron Microscopy
SOCs	States of charge
SRO	Short-range order
TEM	Transmission Electron Microscopy
TEY	Total Electron Yield
TFY	Total Fluorescence Yield
TM	Transition metal
TOC	Top of charge
XANES	X-ray Absorption Near Edge Structure
XAS	X-ray Absorption Spectroscopy
XPDF	X-ray Pair Distribution Function

List of Publications

1. H. Xu, X. Hou, Y. Hu, H. Suga, Z. Hu, E. Dendrick, Y. Yuan, R. A. House and P. G. Bruce.[Manuscript “Temperature-Dependent Transition Metal Migration in Ribbon-Ordered Na(Li)-Mn-O Cathodes” in preparation for the work in Chapter 3]
2. H. Xu, J. Chen, S. D. S. Coutinho, Y. Yuan, G. J. Rees, R. A. House and P. G. Bruce. [Manuscript “The role of high-valent d^0 metal in electrochemistry of disordered rock-salt oxyfluoride cathode” in preparation for the work in Chapter 4]
3. M. Zhang, S. Xu, H. Xu, S. Kang, Z. Wen, W. Li, J. C. Li, A. Chen, J. Tian, R. Hou, Y. Wang, S. Guo and H. Zhou, *Advanced Energy Materials*, 2025, **15**, 2500577.
4. Y. Quan, D. Ji, Y. Yuan, H. Xu, R. Qi, S. D. S. Coutinho, S. Riedel, Z. Zhao-Karger, L. Song, A. W. Robertson, P. G. Bruce and R. A. House, *Journal of Materials Chemistry A*, 2024, **12**, 27303-27310.

1

Introduction

Contents

1.1 Research Background

Electrochemical energy storage is a cornerstone technology underpinning the global transition to renewable energy, sustainable transportation, and resilient electrical grids.[1] Among various energy storage solutions, rechargeable batteries, especially lithium-ion batteries (LIBs), have emerged as the dominant choice due to their high energy density, long cycle life, and versatility across applications ranging from portable electronics to electric vehicles and grid-scale storage.[2]

The evolution of LIBs has been marked by successive breakthroughs in cathode materials. The commercialization of the layered $LiCoO_2$ cathode by Sony in 1991 established the foundation for high-voltage rechargeable cells.[3] However, concerns over the cost, toxicity, and supply risk of cobalt spurred a rapid search for alternative materials.[4] This led to the development of nickel-rich layered oxides, including $LiNi_xMn_yCo_{1-x-y}O_2$ (NMC) and $LiNi_xCo_yAl_{1-x-y}O_2$ (NCA), which offered higher capacity and lower cobalt content, thus improving sustainability and affordability.[5, 6] To address limitations in cycle life and thermal stability, researchers also introduced spinel-type $LiMn_2O_4$ and olivine-structured $LiFePO_4$.[7-9] These materials enhanced safety and broadened the operating temperature window, though often at the expense of lower energy density.

Driven by the quest for ever higher capacities, the focus later shifted to so-called 'Li-rich' layered oxides with partial TM substituted by Li (formula: $Li_{1+x}TM_{1-x}O_2$), which leverage both TM and oxygen redox to obtain excess capacity.[10-14] While these Li-rich cathodes can deliver much greater capacity (> 250 mAh/g), they often suffer from voltage fade, lattice oxygen loss, and structural instability, which have hindered widespread

commercialization.

While LIBs have dominated the energy storage landscape, sodium-ion batteries (SIBs) are emerging as a promising alternative with quite similar working principles.[15] The concept of SIBs could be traced back to the 1980s, when layered oxide cathodes and Na-metal anodes were first explored,[16-18] although early development stalled due to the superior performance of LIBs.[15] Interest in SIBs has revived in recent years due to concerns over lithium resource availability and cost.[19, 20] SIBs offer distinct advantages for grid storage and cost-sensitive applications, benefiting from the abundance and wide geographic distribution of sodium, as well as the feasibility of using aluminum as both cathode and anode current collectors.[21, 22] Over the past decade, a range of cathode materials have been investigated for SIBs, including layered TM oxides, polyanionic compounds, and Prussian blue analogues.[15] Among these, layered oxides (notably the P2, O3, and mixed-phase types) have attracted particular attention due to their tunable structural chemistry and competitive electrochemical performance.[15]

From the perspective of cathode materials development, layered oxides stand out among the materials discussed above due to their significant role in both LIBs and SIBs and their competitive electrochemical performance. Their structural flexibility enables a wide range of compositions and electrochemical behaviors. In particular, slab gliding in layered materials facilitates phase transitions between different stacking sequences, which can be exploited to access metastable structures that are difficult to obtain via direct synthesis. This feature provides a unique opportunity for ion-exchange strategies between Na and Li systems.[23-25] In this thesis, such an approach is employed: as demonstrated in

Chapter 3, Na-layered materials with robust frameworks serve not only as high-performance SIB cathodes, but also as precursors for the ion-exchange synthesis of Li-based layered oxides. This enables a systematic investigation of oxygen redox and transition metal migration across both Na and Li systems.

More recently, disordered rock-salt (DRX) materials have emerged as a promising next-generation class of cathodes.[26, 27] Unlike their layered or spinel counterparts, DRX cathodes feature a highly disordered cation sublattice in which Li and TM randomly occupy the same sites and the choice of TMs is flexible and broad beyond Co or Ni.[28] Li^+ diffusion happens through the three-dimensional percolation networks given an excess of Li content.[29] Notably, DRXs can access extra capacity contributed from oxygen redox, pushing their performance beyond the limits of conventional cathodes.[26, 30-32] Despite progress, challenges persist in controlling TM migration, oxygen stability, and reducing voltage hysteresis. These issues are active areas of current research and will be the focus of Chapters 4 and 5 of this thesis.

1.2 Rechargeable Batteries Fundamentals

Figure 1.1 schematically illustrates the configuration and working mechanism of rechargeable LIBs and SIBs. A typical alkali-ion battery consists of a cathode (positive electrode), anode (negative electrode), electrolyte, separator, and current collectors.[33]

During the charging process, alkali ions (Li^+ or Na^+) are extracted (deintercalated) from the cathode host structure and transport through the electrolyte, across the separator, and are inserted (intercalated) into the anode material. Simultaneously, electrons flow externally from the cathode to the anode via the current collectors, ensuring charge balance.

During discharge, this process is reversed: alkali ions move from the anode back to the cathode, and electrons flow through the external circuit to power a device.

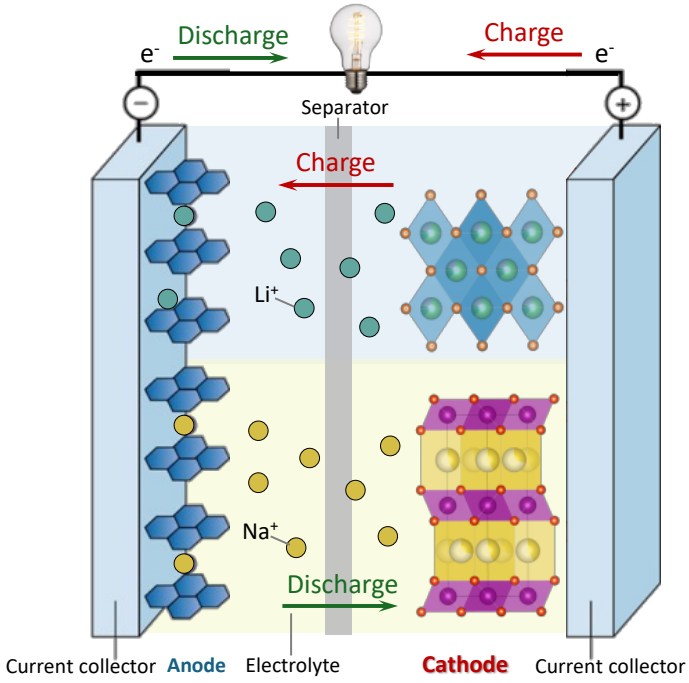

Figure 1.1: Schematic illustration of the main components and the working principles of rechargeable Li- and Na-ion batteries.

A functioning electrode, whether cathode or anode, typically consists of the active material (which stores alkali ions), a conductive additive (often carbon black or similar, especially for cathode materials with poor electronic conductivities), and a polymer binder to adhere the powders onto the current collector foil (typically aluminum for cathodes and copper for anodes in LIBs; aluminum can be used for both in SIBs).

In half-cell configurations, the anode is typically a metallic alkali metal (AM, Li for LIBs, Na for SIBs). While in full cells, graphite and hard carbon are used for LIBs and SIBs, respectively, due to their ability to reversibly host Li^+ or Na^+ ions. In battery research, half cells are widely used for evaluating the intrinsic properties of a specific electrode material since AM anode has constant 0 V reference potential, isolating the performance of

the electrode material.

The electrolyte is usually a non-aqueous solution containing a lithium or sodium salt, such as $LiPF_6$ or $NaPF_6$, respectively, in an organic carbonate solvent. The separator is a porous membrane, typically polyolefin-based, that prevents direct contact between the cathode and anode while allowing ion transport.

The equilibrium voltage of a Li- or Na-ion cell is fundamentally determined by the difference in chemical potentials of the two electrodes. It is approximated the difference in the redox potentials of the cathode and anode materials versus a common reference (*e.g.*, Li^+/Li or Na^+/Na). The equilibrium cell voltage can be expressed by the Nernst equation:

$$E^\circ = -\frac{\mu^+ - \mu^-}{zF} = -\frac{\Delta G}{zF} \tag{1.1}$$

where E° is the equilibrium cell voltage, μ^+ and μ^- are the chemical potentials of the positive and negative electrodes respectively, z is the charge of the carrier ion (1 for Li^+/Na^+), F is the Faraday constant (96485 C mol^{-1}) and ΔG is the Gibbs free energy of the system. During charging and discharging at finite current, the cell voltage deviates from equilibrium and is expressed as

$$E = E^\circ - \frac{RT}{zF} ln Q_r \tag{1.2}$$

where R is the ideal gas constant, T is the temperature, and Q_r is the reaction quotient described as

$$Q_r = \frac{a_{red}}{a_{ox}} \tag{1.3}$$

where a_{red} and a_{ox} are the chemical activities of the reductant and the oxidant, respectively. The activities are dependent of the concentration of alkali ions in the electrodes, corresponding to the states of charge (SOCs).

The cell voltage reflects the energy per unit charge that can be extracted from the battery. In general, Li-ion batteries exhibit higher cell voltages (typically 3.5–4.2 V) than Na-ion batteries (2.5–3.8 V), owing to the more negative standard reduction potential of Li^+/Li compared to Na^+/Na.

The specific capacity of a battery electrode is defined as the total amount of charge that can be stored and delivered per unit mass of the active material, typically expressed in the unit of mAh g^{-1}. It is based on the number of electrons (or alkali ions) that can be reversibly inserted into or extracted from the electrode's crystal structure during the charge and discharge processes. The theoretical specific capacity of an electrode material is calculated as:

$$Specific\ Capacity\ (mAhg^{-1}) = \frac{nF}{3.6M_w} \tag{1.4}$$

where n is the number of electrons (and alkali ions) transferred per formula unit, F is the Faraday constant, and M_w is the molar mass of the active material in grams. Materials capable of multi-electron transfer and/or involving both transition metal and oxygen redox can therefore achieve higher capacities.

The total energy stored or delivered by a battery during operation is calculated as the time integral of the instantaneous product of cell voltage and current, which is equivalently expressed as the integral of voltage with respect to capacity:

$$Total\ Energy\ (Wh) = \int_{Q_i}^{Q_f} V(Q)dQ \tag{1.5}$$

where $V(Q)$ is the cell voltage as a function of capacity Q, and the integration is performed from the initial to the final capacity. This equation highlights that the total energy output depends both on the cell voltage profile and the amount of charge (capacity) transferred

during the cycle. The energy density, either gravimetric (Wh kg^{-1}) or volumetric (Wh L^{-1}), is a critical parameter for evaluating the practical performance of batteries. In a full cell, the overall energy density is jointly determined by both the cathode and anode materials. While typical anodes such as graphite and lithium metal possess relatively high theoretical capacities of 372 mAh g^{-1} and 3860 mAh g^{-1},[5] respectively, conventional cathode materials, such as layered oxides (~150–250 mAh g^{-1}), spinels (~120 mAh g^{-1}), or olivines (~170 mAh g^{-1}), offer much lower capacities.[34, 35] Consequently, the major limitation to further improving the energy density of current lithium-ion batteries lies in the cathode. Therefore, developing cathode materials that combine high specific capacity with high average working voltage under practical operating conditions is essential for advancing next-generation battery technologies.

1.3 Oxygen Redox

1.3.1 Brief Introduction and History

The energy storage capacity of traditional cathode materials for Li- and Na-ion batteries, has long been governed by the redox chemistry of TM cations. Typified by $LiCoO_2$, Figure **1.2(a-b, e-f)** illustrates the crystal and band structure along with the first voltage profile. In such materials, the TM ions act as the primary electron reservoirs: during charging and discharging, electrons are removed from or added to the (M-O)* band which is of TM character, enabling reversible extraction and insertion of alkali ions.[36] However, the theoretical capacity of these cathodes is fundamentally limited by the number of electrons and alkali ions that can be exchanged through cationic redox alone.

A major breakthrough in cathode material design emerged with the discovery of anionic redox, where the oxygen sublattice in the cathode can also participate in reversible charge compensation. This process enables the extraction of more electrons and alkali ions per formula unit, nearly doubling the accessible capacity compared to conventional TM redox. The archetype for this mechanism is found in Li-rich layered oxides where the ratio of Li to TM is greater than 1 such as $Li_{1.2}Ni_{0.13}Mn_{0.54}Co_{0.13}O_2$ (Li-rich NMC). As shown in **Figure 1.2(c-d)**, these compounds contain excess Li within the TM layers in addition to the Li in the Li layers, and one of the O 2*p* orbitals (the one pointing towards Li) is weakly bonded due to its relatively small overlap with the Li 2*s* orbital. This so-called "Li-O-Li" linear configuration gives rise to unique O 2*p* non-bonding (O_{NB}) states which sit energetically above the (M-O) bonding band, as displayed in **Figure 1.2(h)**, allowing oxygen to act as an additional redox center at high potentials.[36, 37] **Figure 1.2(f-g)** compares

Figure 1.2: *The figure originally presented here cannot be made freely available via ORA because of copyright. The figure was sourced at bibliographic reference Assat et al.*[36]

the crystal structures and voltage profiles of conventional $LiCoO_2$ and Li-rich NMC. For

Li-rich NMC, the voltage profile exhibits a two-step charge process: an initial sloping region associated with TM oxidation, similar to $LiCoO_2$, followed by an extended plateau at approximately 4.5 V vs. Li^+/Li. This additional plateau reflects the contribution of oxygen redox to the overall capacity. During discharge, the voltage profile shows a characteristic S-shaped curve at a lower average voltage. The resulting voltage difference between charge and discharge, known as "voltage hysteresis", can be substantial in oxygen-redox systems. A pronounced hysteresis reduces the discharge energy density and overall battery efficiency.[36] Consequently, understanding the mechanistic origins of voltage hysteresis and developing strategies to mitigate it are essential steps toward the practical application of cathode materials exploiting oxygen redox.

The historical roots of anionic redox can be traced back to studies on chalcogenides (*e.g.*, TiS_2, FeS_2), where ligand (anion) participation in redox was identified via the concept of "ligand holes".[38] However, it was not until the late 1990s that similar behavior was suggested for oxides that anomalous capacity and structural changes in delithiated Li_xCoO_2 were proposed to be related to oxygen redox activity, as evidenced by synchrotron diffraction and *ab initio* study.[39, 40] The field began to gain momentum in the early 2000s, when researchers discovered electrochemical activity in Li_2MnO_3.[10] Later the study on a ternary phase containing Li_2MnO_3 and $LiMO_2$ end-members, formulated as $xLiMO_2 \cdot (1-x)Li[Li_{1/3}Mn_{2/3}]O_2$, exhibited remarkably high specific capacities exceeding 250 mAh g^{-1}, much higher than those of traditional layered oxides, although the underlying mechanism was not yet understood.[11, 41] Around 2010, Yabuuchi and co-workers proposed that the anomalously high capacity originated from irreversible oxygen loss during the first charge,

accompanied by partial reduction of manganese.[42] Subsequent investigations combining advanced spectroscopy and theoretical calculations in the early 2010s provided conclusive evidence that lattice oxygen can participate in reversible redox processes, contributing significantly to the overall charge compensation.[12, 43, 44] Today, oxygen redox is widely recognized as a promising strategy to breakthrough the cathode capacity limit imposed by TM-only redox and is actively investigated in both layered and disordered materials, as well as in Na-ion analogues.[14, 26, 37, 45, 46]

1.3.2 Fundamental Mechanism

Despite clear experimental evidence for high-capacity oxygen redox in Li-rich layered oxides, the exact nature of the oxidized oxygen species and its relationship with structural changes and degradation has remained a subject of intense debate and turned out to be material-dependent. Multiple theories have been proposed to explain how oxygen participates in charge compensation and why this process often leads to voltage hysteresis, structural disorder, and limited reversibility, as schematically summarized in **Figure 1.3.**

Figure 1.3(a) displays the formation of electron holes (O^{n-} species) in O_{NB} orbitals which are coordinated by Li upon delithiation in Li-rich TM oxides to high voltages.[13, 47] This model is supported by spectroscopic evidence indicating depopulation of O 2*p* states and the emergence of oxidized O signatures.[48, 49] This theory was further developed to explain the voltage hysteresis of oxygen redox by pointing out partially reversible out-of-plane TM migration as shown in **Figure 1.3(b)**.[50] The O_{NB} orbitals are stabilized by the coordinated Mn with π-type back-bonding **(Figure 1.3(c))**.[51]

Figure 1.3(d-e) illustrates the case of reductive coupling mechanism originally found

in 4*d* and 5*d* TM-based Li-rich layered oxides. TM overoxidation upon charging triggers oxidation of oxygen and the oxidized oxygen dimerizes with the neighboring oxygen to get a more stable electron structure, forming peroxo-like species O_2^{n-} ($0< n< 2$). O–O dimers have shorter distances (1.2 Å) compared to the distance between oxygen within the lattice,

Figure 1.3: *The figure originally presented here cannot be made freely available via ORA because of copyright. The figure was sourced at bibliographic reference House et al.*[54]

which can be visualized using TEM and neutron diffraction.[46] This dimerization process is coupled with TM reduction, as in TM receiving electrons from oxygen.[37, 45, 52] Out-of-plane TM migration is also involved in this theory, associated with the formation of short TM=O bonds and peroxides (O_2^{2-}) in Sn-substituted Li_2IrO_3, for instance.[53]

An alternative theory was proposed by Radin *et al*. that the extra capacities in Mn-based Li-rich layered oxides derive from the oxidation of Mn beyond +4 to +7 along with Mn migration into tetrahedral sites as illustrated in **Figure 1.3(f)**.[55]

Figure 1.3(g) illustrates the theory of molecular oxygen being trapped within vacancy clusters in the bulk. Upon charging, Li ions migrate from the TM layers into the AM layers, leaving vacancies behind. As a result, TM rearrange within the TM plane, forming vacancy clusters that can accommodate oxygen molecules. This Mn–η^1–O_2 (where η^1 indicates the hapticity, indicating end-on coordination of O_2 to a single Mn center) species can be identified using high-resolution Resonant Inelastic X-ray Scattering (RIXS), which reveals a vibrational progression with a frequency of ~1600 cm^{-1} typical of molecular oxygen with a bond length of 1.2 Å.[14, 48]

Figure 1.3(h) gives a supplementary explanation for the irreversible oxygen gas loss upon charging in Li-rich layered oxides. The oxidized oxygen gets dimerized with the neighbouring oxygen and loses enough electrons to form O_2, which is released from the surface. This process is accompanied by surface densification, where TMs migrate inwards from the surface to AM layers, forming rocksalt-like structure to compensate for the loss of O_2.[54]

Taken together, these mechanistic frameworks emphasize the strong coupling between oxygen redox, TM migration, and local structural transformations. For example, the formation of oxidized O species is frequently stabilized through local coordination rearrangement, either by cation migration that creates vacancies adjacent to oxygen, or through dimerization that modifies band structure of the O 2*p* states.

1.3.3 Strategies for Reversible Oxygen Redox

Oxygen redox holds immense promise for unlocking higher energy density in Li- and Na-ion batteries. However, its widespread application is hindered by cycling instability, large voltage hysteresis, and rapid capacity fade, which primarily originate from fundamental structural challenges such as TM migration, oxygen loss, and irreversible lattice transformations.

A range of strategies has been proposed to address these issues, including surface modification, pillaring the layered framework, and introducing electrochemically inactive ions into the TM layers to suppress detrimental structural evolution. **Figure 1.4** demonstrates two specific strategies that are directly connected to the research in this thesis.

Figure 1.4: *The figure originally presented here cannot be made freely available via ORA because of copyright. The figure was sourced at bibliographic reference House et al.*[48, 54]

(a) Superstructure Engineering and Temperature Control in Layered Materials

Controlling the superstructure within TM layers has emerged as a powerful method to stabilize oxygen redox. Traditional honeycomb ordering, though common in Li-rich and Na-rich layered cathodes, is highly susceptible to in-plane TM migration during cycling, leading to the formation of molecular O_2 within vacancy clusters and severe voltage hysteresis. Recent breakthroughs have shown that alternative superstructure motifs, such as the ribbon or mesh ordering, can effectively reduce TM migration and vacancy-cluster formation by increasing the migration distances, therefore stabilizing oxidized oxygen species in the bulk. House *et al*. demonstrated that ribbon-ordered $Na_{0.6}[Li_{0.2}Mn_{0.8}]O_2$ retains its high-voltage plateau during discharge, preventing the rapid voltage decay typical of honeycomb counterparts.[48]

In addition to superstructure design, controlling the operational temperature, as explored in Chapter 3 of this thesis, offers a practical approach to inhibiting unwanted TM migration, further prolonging the high-voltage discharge plateau and delaying structural degradation. Lower cycling temperatures slow down atomic diffusion, helping to maintain the integrity of the ribbon superstructure and supporting more stable oxygen redox behavior.

(b) Cation Disorder in DRX Cathodes

A second approach is to accept and leverage cation disorder, moving beyond layered arrangements to DRX frameworks. In these materials, Li (or Na) and TM ions are randomly distributed, frustrating the pathways for large-scale TM migration and major phase transitions. As shown in **Figure 1.4(b)**, DRX cathodes can sustain substantial alkali extraction and reversible oxygen redox without severe lattice destabilization or rapid amorphization. Chapters 4 and 5 of this thesis will systematically explore how the unique

cation disorder of DRX cathodes enables high-capacity, long-life performance with more manageable voltage hysteresis compared to layered analogues.

1.4 Layered Materials

1.4.1 Structure Classification

The layered materials have been widely studied as promising cathode candidates for both LIBs and SIBs. The common structure is composed of layers of edge-shared TMO_6 octahedra and alkali ions in between. Based on the classification rule proposed by Delmas *et al.*,[56] the layered materials can be named by the AM coordination environment (O: octahedral; P: prismatic; T: tetrahedral) and the number of crystallographically different layers to describe the unit cell.[15, 24]

Lithium TM layered oxide materials, like $LiCoO_2$, are mainly O3-type structure as displayed in **Figure 1.5**. The structure consists of a cubic close-packed (ccp) oxygen lattice framework with Li and TM accommodated in distinct octahedral sites, which is indexed to the space group $R\bar{3}m$.[15] For Li-rich materials with superstructure ordering within TM layers (like honeycomb ordering in Li_2MnO_3), the structure is indexed to the *C2/m* space group with monoclinic feature.[57] There are three different possible configurations of the TMO_2 layers: AB, CA and BC. O3-type structure could be seen as one of the cation-ordered rock-salt superstructure oxides where AM and TM layers alternately stack along the [111] axis.[58]

Since Na ions are relatively larger than Li ions, they can be accommodated in both octahedral and trigonal prismatic sites, depending on the amount of Na present.[15] Recent studies reported that cationic potential plays a significant role in determining whether the

structure will adopt an O3 or P2 configuration.[59] But in general, for stoichiometric Na content, like $NaFeO_2$, the structure is the O3 type, isostructural to $LiTMO_2$. When it comes to off-stoichiometry (typically $0.6< x< 0.7$ in Na_xTMO_2), the P2-type phase is more structurally stable. As shown in **Figure 1.5**, in the P2-type structure, there are two different TMO_2 layers, AB and BA, where Na ions are located at prismatic sites between the TM layers. The P2-type phase is typically indexed to a $P6_3/mmc$ space group. When there is distortion within the plane, the structure can turn into a monoclinic lattice (space group $C2/m$) like O'3-type $NaMnO_2$ or an orthorhombic lattice (space group *Cmcm*) like P'2-type

Figure 1.5: *The figure originally presented here cannot be made freely available via ORA because of copyright. The figure was sourced at bibliographic reference Yabuuchi et al.[15]*

Na_xMnO_2, using a prime symbol to mark the structural variation.[17, 60] Besides, the superstructure ordering within TM layers can also alternate the space group from $P6_3/mmc$ to $P6_3$ (like honeycomb ordering in $Na_{0.75}[Li_{0.25}Mn_{0.75}]O_2$), or $P2_1/c$ (like ribbon ordering in $Na_{0.6}[Li_{0.2}Mn_{0.8}]O_2$), or $P\bar{1}$ (like mesh ordering in $Na_2Mn_3O_7$).[48, 61]

1.4.2 Phase Transition and Stacking Faults

Due to the gliding feasibility of TMO_2 slabs without breaking TM-O bonds, the layered structures can undergo a phase transition into other types of layered stacking or generate local stacking faults.[17, 56] As shown in **Figure 1.5**, Na extraction or Na^+/Li^+ ion exchange can induce phase transitions. When partial Na is extracted from the O3-type phase, the off-stoichiometry of Na results in prismatic sites getting more energetically stable. Therefore, the oxygen packing changes from "AB CA BC" to "AB BC CA", leading to the formation of the P3-type phase.[56] P3-type phase could also be prepared via direct solid-state reaction at relatively lower temperatures than those for the P2-type phase.[62] What's more, the P3-type Na layered oxides can be the precursor to make O3-type Li layered oxides via ion exchange method since Li prefers to locate at octahedral sites.[25] When Li is extracted from the O3-type phase in Li cells, it may transform into O1 phase or have O1-type stacking fault with an oxygen packing configuration of "AB AB", although this is not displayed in the **Figure 1.5**.[63] As reported in charged Li_xCoO_2, an intergrown structure of the O1 and O3 phases exists and is named H1-3 phase.[64, 65] It is important to note that the O3/P3-type phase cannot transform into the P2-type phase in Na cells because it requires breaking and reforming TM-O bonds, which needs a higher temperature environment.[15]

The P2-type phase can evolve into the O2 phase after Na removal in Na cells or by Na^+/Li^+ ion exchange since large prismatic sites need to be energetically stabilized by large Na ions.[66-68] TMO_2 slabs glide to transform the oxygen packing from "AB BA" to "AB AC" which results in the formation of the octahedral sites between TM layers. There are two equivalent glide vectors of TMO_2 slabs: (1/3, 2/3, z) and (2/3, 1/3, z). This behavior can lead to different stacking faults in several reported materials, resulting in the emergence of

new variants such as T2 (from Li exchange for Na in the O2 phase), O4 (from Li exchange for Na in the OP4 phase), OP4 (an intergrowth of the O2 and P2 phases) and O6 (an intergrowth of the O2 and O2' phase).[23, 24, 66, 68-73]

1.5Disordered Rock-Salt Materials

1.5.1 Crystal Structure and Chemical Formula Feature

DRX and layered counterparts are both isostructural with rock salt (NaCl) where cations and anions were positioned at octahedral sites within two interpenetrating face-centered cubic (FCC) lattices. The difference between the two structures lies in the distribution of Li and TM ions on the cation sublattice, as shown in **Figure 1.6(a)**.[74] In the

Figure 1.6: *The figure originally presented here cannot be made freely available via ORA because of copyright. The figure was sourced at bibliographic reference Urban et al.*[28]

case of DRX compounds, Li and TM ions are theoretically distributed randomly, whereas layered counterparts exhibit an ordered distribution of Li and TM ions within alternating layers along the [111] axis. Apart from layered structure, Li and TM ions can be arranged

in other ordered configurations in rock-salt-type compounds, leading to spinel-like and γ-$LiFeO_2$ structures.

The cation-disordered structure generally forms at higher temperatures compared with other types of rock-salt materials. Urban *et al.* studied the factors that facilitate cation disorder at synthetically accessible low temperatures.[75] They suggested that the disordered distribution of Li and TM ions in octahedral sites leads to site distortions due to their different valences. Since Li^+ has no valence electron, it has no preference in an octahedral crystal field. Moreover, TM ions with no *d* electrons can accommodate these distortions with lower energy costs, despite the significant differences in ionic radii between the cations. In other words, a d^0 charge compensator (*e.g.* Ti^{4+}, Zr^{4+}, V^{5+}, Nb^{5+}, Mo^{6+}) is effective at stabilizing the DRX structure, which is consistent with the experimental findings of electrochemically active DRX compounds.[31, 76-81] Therefore, the majority of DRX oxides reported so far can be summarized using a unified chemical formula: $Li_{1+x}M'_{1-x-y}M''_yO_2$, where M'= redox-active metal, *e.g.* Mn, V, Ni, Mo, *etc.* and M''= d^0 elements. The presence of excess Li not only helps accommodate the distortions but also promotes long-term percolation, which will be discussed in the next section.

Another unique feature of DRX compounds is that the O anions can be partly substituted by F, which is proven to be an effective strategy to improve energy density and cycling stability. The general formula of DRX oxyfluorides is $Li_{1+x}M_{1-x}O_{2-y}F_y$. Richards *et al*. have explained the difference in F solubility of cation disordered LMOs and their layered counterparts.[82] In layered oxides, anion sites are surrounded by three TM nearest neighbors, which makes fluorine substitution less favorable due to the strong M-F bond. In

contrast, the cation-disordered structure can create metal-poor, lithium-rich sites that allow for more favorable integration of fluorine. In fact, more and more DRX oxyfluorides have been reported in various TM systems, with the incorporation of F in bulk lattice confirmed by element-specific techniques like ^{19}F NMR spectroscopy.[30, 76, 78, 83-88] Clement *et al*.[30, 76, 78, 83-88] revealed that 90% of F^- in $Li_{1.15}Ni_{0.45}Ti_{0.3}Mo_{0.1}O_{1.85}F_{0.15}$ are accommodated in configurations of either FLi_6 or FLi_5TM based on the combination of solid-state NMR and Monte Carlo simulations.[78] Fluorination can affect the local environment, such as short range order (SRO) in DRX materials, due to its tendency to attract Li, and influence Li diffusion and cycling performance. The degree of fluorination depends a lot on the synthesis method. It is suggested that the solubility limit of F in the DRX lattice is around 10% based on the solid-state method, with a practical temperature limit of around 1100 °C.[82] To achieve a F content exceeding 30%, the mechanochemical method is currently the only reported feasible option so far. Kitchaev *et al*. determined that the heuristic temperature of high-energy ball-milling is approximately 1750 °C by marking the reported successfully synthesized DRX compositions on the corresponding phase diagram.[76] Fluorination has significant impact on the properties of compounds, including Li^+ diffusion, redox character and consequent electrochemical performance.[89]

1.5.2 Li-ion Transport and Percolation Theory

In rock-salt $LiTMO_2$ compounds, Li^+ can only hop from one octahedral site to another octahedral site via an intermediate face-sharing tetrahedral site.[90-92] The process is termed as "O_h-T_d-O_h" diffusion, illustrated in **Figure 1.7(a)**.[29] When Li^+ hops into the tetrahedral site, it triggers the activated state with four face-sharing octahedral sites. Among them, two

sites should be where Li^+ comes from and moves into within hopping pathways, respectively. And the other two sites can be occupied by Li, TM or vacancy, leading to different configurations of tetrahedral cluster: 0-TM, 1-TM and 2-TM channels.[93] 0-TM means four face-sharing octahedral sites are all occupied by Li or vacancy, with no TM ions. Similarly, 1-TM and 2-TM configurations denote tetrahedral clusters in which the adjacent octahedral sites are occupied by one and two TM ions, respectively. The Li^+

Figure 1.7: *The figure originally presented here cannot be made freely available via ORA because of copyright. The figure was sourced at bibliographic reference Lee et al.*[29]

migration barrier in the tetrahedral cluster is generally determined by the electrostatic repulsion between activated Li^+ at intermediate T_d site and species of the other two sites, depending on the valence of the species and the space between Li^+ and the species (generally deemed as average tetrahedron height).[29, 93] For 2-TM channels which dominantly exist in γ-$LiFeO_2$, the electrostatic repulsion on activated Li^+ is too strong for active diffusion.[90, 94, 95] The 1-TM channels are the case for Li transport in layered $LiTMO_2$ compounds. The activation barriers for Li diffusion are around 300 meV given that the Li slab distances (Li-TM spacing) are usually 2.6-2.7 Å in layered structure.[95] In contrast, for DRX compounds, Lee *et al*. calculated the Li migration barriers for both 0-TM and 1-TM channels in a typical sample $Li_{1.211}Mo_{0.467}Cr_{0.3}O_2$, as shown in **Figure 1.7(b)**.[29] They found the barriers for 1-TM channels are around 500 meV, much higher compared with those in layered oxides. This can be ascribed to the relatively smaller average tetrahedron height of around 2.39 Å (Li-TM spacing), which leads to stronger electrostatic repulsion. In fact, typical tetrahedron heights are usually 2.35-2.45 Å in DRX structures, as shown in the shaded area of **Figure 1.7(a)**, much smaller than Li slab distances in layered structures.[93] Moreover, the barriers for 0-TM channels are below 300 meV due to the lower valence of the face-sharing octahedral Li^+ compared with TM ions. The results indicate that only 0-TM channels are active for reasonable Li^+ hopping rate in DRX structures.

However, the existence of 0-TM channels alone does not guarantee macroscopic lithium diffusion unless they are sufficiently interconnected throughout the entire bulk to form percolation networks.[29] To increase the number of 0-TM channels in DRX materials, the content of lithium must be increased. Based on Monte Carlo simulations, Lee *et al*.

calculated the 0-TM percolation probability and the accessible Li content to be extracted as a function of Li content and cation mixing in DRX $Li_xTM_{2-x}O_2$.[29] As shown in **Figure 1.7(c)**, there is a 0-TM percolation threshold at x~1.09 for fully cation-disordered oxides. In other words, when designing active DRX compounds, it is generally necessary to include at least ~10% excess Li to ensure a percolating network for Li-ion transport. This requirement explains why many reported stoichiometric disordered compounds exhibit little to no electrochemical capacity.[96-98] Notably, the percolation threshold can be reduced (to x~1.05) in DRXs composed of nano-sized particles, as the shorter Li transport distances facilitate percolation even at lower Li content.[99]

The simulations discussed earlier assume perfect cation disorder at each mixing level in $Li_xTM_{2-x}O_2$. However, in actual DRX materials, cations often exhibit local coordination preferences. For example, F substitution significantly influences the spatial distribution of Li ions. Lun *et al*. investigated the model system $Li_xMn_{2-x}O_{2-y}F_y$ and found that at low F content, fluorination hinders Li diffusion. This is attributed to the tendency of dilute F^- ions to attract Li^+, resulting in the formation of isolated Li-rich domains that do not contribute to long-range percolation.[89] As the F content increases beyond a critical threshold, these Li-rich domains become interconnected, enabling effective percolation. Furthermore, at relatively low Li content, higher levels of F substitution can facilitate Li percolation. It was also observed that the critical F content required for percolation rises with increasing Li content, and when Li content approaches ~1.33, further fluorination ceases to enhance percolation.

1.5.3 Current challenges

Capacity Decay and Voltage Fade

Despite significant advances, most DRX cathode materials still suffer from rapid capacity decay and energy density fade during cycling, severely limiting their practical application. The underlying degradation mechanisms are multifaceted but can be largely attributed to oxygen redox instability, structural amorphization, and particle fracture.

The primary challenge involves the instability of oxidized oxygen species generated during high-voltage charging in Li-rich DRX compounds. As illustrated in **Figure 1.8(a)**, operando Differential Electrochemical Mass Spectroscopy (DEMS) measurements reveal that in $Li_{1.3}Nb_{0.3}Mn_{0.4}O_2$, the oxidized oxygen cannot be stabilized within the lattice and is irreversibly released as O_2 gas.[100] This persistent oxygen loss leads to a series of detrimental effects, including the TM over-reduction and migration. This causes incomplete lithium reinsertion during discharge, resulting in capacity fade and average voltage decay. **Figure 1.8(b)** illustrates a vicious cycle of TM densification caused by oxygen loss and the spread process from surface to bulk during cycles.[101] In addition, Chen *et al*. pointed out the synergetic role of F densification (LiF-type domains on the surface) along with TM densification in the degradation of DRX oxyfluorides.[102] In **Figure 1.8(c),** Li *et al*. used Scanning Transmission Electron Microscopy (STEM) to detect the structural amorphization and void formation spreading from the particle surface of $Li_{1.2}Mn_{0.4}Ti_{0.4}O_2$, which can be mitigated by fluorination evidenced by the variant $Li_{1.2}Mn_{0.6}Ti_{0.2}O_{1.8}F_{0.2}$. The bulk structural transformation from rock-salt to spinel was also revealed by Annular Dark Field (ADF)-STEM image filtering, contributing to the capacity increase during cycling.[103] Kan *et al*. recorded the morphology evolution of the $Li_{1.3}Nb_{0.3}Mn_{0.4}O_2$ single-crystal particle during the

first charging using Scanning Electron Microscopy (SEM), as demonstrated in **Figure 1.8(d)**. As lithium is gradually extracted, more large cracks develop across the entire particle when $x<$ 0.9, ultimately leading to fracturing of the crystals. The number of cracks reaches the maximum when $x=$ 0.5-0.6, consistent with the occurrence of phase transformation (volume change) and oxygen redox processes.[104]

Figure 1.8: *The figure originally presented here cannot be made freely available via ORA because of copyright. The figure was sourced at bibliographic reference Chen et al[100], Chen et al[101], Li et al[103], and Kan et al.[104]*

Limited Volumetric/Gravimetric Energy Density

Nearly all reported DRX materials rely on reduced particle sizes, typically achieved via pulverization, to compensate for intrinsically low Li diffusivity. But small particles will

decrease the packing density and aggravate side reactions with the electrolyte. Another significant issue is the low content of active material in electrode composite. The most common weight ratio of active material, carbon conductor and binder in electrode composite reported is 70:20:10, and in some studies, the active material only accounts for around 60%. This limitation severely restricts the practical volumetric and gravimetric energy density of DRXs, despite their specific energy density looking competitive in the literature as shown in **Figure 1.9(a)**. The gravimetric energy density ($Wh/kg_{-cathode}$) is calculated by multiplying the specific energy density (Wh/kg_{-AM}) by the ratio of active material. The volumetric energy density ($Wh/L_{-cathode}$) is obtained by multiplying the gravimetric energy density ($Wh/kg_{-cathode}$) by the electrode density (g/cm^3). The electrode density is closely related to the composition and porosity. Given that the theoretical crystal density of DRXs ranges from 3.5 to 4.3 g/cm^3, whereas the densities of carbon and binder are 2.2 g/cm^3 and 1.76 g/cm^3, respectively.[79, 105, 106] For an electrode composed of 70% DRX, 20% carbon, and 10% binder, with 40% porosity, the calculated electrode density would be around 2.06 g/cm^3 (using a representative crystal density of 4 g/cm^3). This value is considerably lower than that of NMC layered oxides, primarily due to the high content of inactive materials, which reduces electrode density The electrode porosity will unsurprisingly increase with smaller particle size, with 20% for polycrystalline or single-

Figure 1.9: *The figure originally presented here cannot be made freely available via ORA because of copyright. The figure was sourced at bibliographic reference Clement et al[26] and Li et al.[105]*

crystal particles and reaching ~40% for nanoparticles.[105] **Figure 1.9(b-d)** illustrates the evaluated volumetric energy densities (Wh/L) of Mn-based DRXs as a function of the accessible gravimetric energy density (Wh/kg) and porosity with different electrode composition.[105] Therefore, for the specified composition of 70:20:10 with 40% porosity, the DRX active material with a gravimetric energy density of 800 Wh/kg will yield a cathode gravimetric energy density of 560 Wh/kg and a cathode volumetric energy density of about 1154 Wh/L. It is worth considering that the higher the gravimetric energy density, the greater the difference in volumetric energy densities with different electrode

composition. Therefore, when comparing specific energy and cycle life of DRX compounds, the electrode composition (electrode density) and particle size (porosity) need to be considered.

1.6 Thesis Objectives

The objective of this thesis is to systematically investigate the structural and electrochemical mechanisms that govern TM migration and oxygen redox processes in advanced cathode materials for Li- and Na-ion batteries. The thesis aims to provide new insights into the interplay between crystal structure, cation substitution, and redox chemistry, with a focus on layered oxides and DRX materials, to guide the rational design of high-capacity, stable-cycling cathode materials for LIBs and SIBs.

To this end, the specific objectives are:

1. To elucidate the role of TM migration and stacking sequence in layered oxide cathodes.

   By examining Na- and Li-based layered oxides as model systems, Chapter 3 develops and applies an electrochemical descriptor (ΔP) to correlate phase transitions, TM migration kinetics, and structural evolution, providing guidance for the design of layered oxides with enhanced stability.

2. To uncover the dual effects of high-valent d^0 cation substitution in Mn-based DRX oxyfluorides.

   Chapter 4 systematically investigates how d^0 cations (e.g., W^{6+}) influence both reversible TM redox capacity and Li-ion transport. Advanced spectroscopy and Monte Carlo simulations are used to better understand the trade-offs between redox activity and ionic mobility.

3. To clarify how cation substitution and electronic structure control redox mechanisms and reversibility in Ni-based DRXs.

   By comparing Nb- and W-substituted Ni-based DRX systems, Chapter 5 aims to establish a link between charge transfer energetics and electrochemical behaviors including oxygen redox process, voltage hysteresis, and cycling stability.

Through these objectives, this thesis aims to establish new design principles for next-generation cathode materials, balancing high reversible capacity with structural robustness and rate performance.

1.7 References

1. D. Larcher and J. M. Tarascon, *Nature Chemistry*, 2015, **7**, 19-29.
2. G. G. Njema, R. B. O. Ouma and J. K. Kibet, *Journal of Renewable Energy*, 2024, **2024**, 2329261.
3. T. Nagaura, *Progress in Batteries & Solar Cells*, 1990, **9**, 209.
4. G. Harper, R. Sommerville, E. Kendrick, L. Driscoll, P. Slater, R. Stolkin, A. Walton, P. Christensen, O. Heidrich, S. Lambert, A. Abbott, K. Ryder, L. Gaines and P. Anderson, *Nature*, 2019, **575**, 75-86.
5. J. M. Tarascon and M. Armand, *Nature*, 2001, **414**, 359-367.
6. N. Nitta, F. Wu, J. T. Lee and G. Yushin, *Materials Today*, 2015, **18**, 252-264.
7. A. K. Padhi, K. S. Nanjundaswamy and J. B. Goodenough, *Journal of the Electrochemical Society*, 1997, **144**, 1188.
8. M. M. Thackeray, W. I. David, P. G. Bruce and J. B. Goodenough, *Materials Research Bulletin*, 1983, **18**, 461-472.
9. M. S. Whittingham, *Chemical Reviews*, 2004, **104**, 4271-4302.
10. A. D. Robertson and P. G. Bruce, *Chemistry of Materials*, 2003, **15**, 1984-1992.
11. M. M. Thackeray, S. H. Kang, C. S. Johnson, J. T. Vaughey, R. Benedek and S. Hackney, *Journal of Materials Chemistry*, 2007, **17**, 3112-3125.

12. H. Koga, L. Croguennec, M. Ménétrier, P. Mannessiez, F. Weill and C. Delmas, *Journal of Power Sources*, 2013, **236**, 250-258.

13. K. Luo, M. R. Roberts, R. Hao, N. Guerrini, D. M. Pickup, Y. S. Liu, K. Edstrom, J. Guo, A. V. Chadwick, L. C. Duda and P. G. Bruce, *Nature Chemistry*, 2016, **8**, 684-691.

14. R. A. House, G. J. Rees, M. A. Pérez-Osorio, J. J. Marie, E. Boivin, A. W. Robertson, A. Nag, M. Garcia-Fernandez, K. J. Zhou and P. G. Bruce, *Nature Energy*, 2020, **5**, 777-785.

15. N. Yabuuchi, K. Kubota, M. Dahbi and S. Komaba, *Chemical Reviews*, 2014, **114**, 11636-11682.

16. G. H. Newman and L. P. Klemann, *Journal of the Electrochemical Society*, 1980, **127**, 2097.

17. C. Delmas, J. J. Braconnier, C. Fouassier and P. Hagenmuller, *Solid State Ionics*, 1981, **3**, 165-169.

18. C. Delmas, B. J. J. A. Maazaz and P. Hagenmuller, *Revue de Chimie Minerale*, 1982, **19**, 343-351.

19. S. Sangsinsorn, S. Dsoke and O. Cojocaru-Mirédin, *arXiv preprint arXiv:2411.10095*, 2024.

20. A. Yao, S. M. Benson and W. C. Chueh, *Nature Energy*, 2025, **10**, 404-416.

21. J. Y. Hwang, S. T. Myung and Y. K. Sun, *Chemical Society Reviews*, 2017, **46**, 3529-3614.

22. M. D. Slater, D. Kim, E. Lee and C. S. Johnson, *Advanced Functional Materials*, 2013, **23**, 947-958.

23. N. Yabuuchi, R. Hara, M. Kajiyama, K. Kubota, T. Ishigaki, A. Hoshikawa and S. Komaba, *Advanced Energy Materials*, 2014, **4**.

24. J. M. Paulsen, R. A. Donaberger and J. R. Dahn, *Chemistry of Materials*, 2000, **12**, 2257-2267.

25. J. Paulsen and J. Dahn, *Solid State Ionics*, 1999, **126**, 3-24.

26. R. J. Clément, Z. Lun and G. Ceder, *Energy & Environmental Science*, 2020, **13**, 345-373.

27. H. M. Hau, T. Holstun, E. Lee, B. L. D. Rinkel, T. P. Mishra, M. M. DiPrince, R. S. Mohanakrishnan, E. C. Self, K. A. Persson, B. D. McCloskey and G. Ceder, *Advanced Materials*, 2025, 2502766.

28. A. Urban, J. Lee and G. Ceder, *Advanced Energy Materials*, 2014, **4**, 1301453.

29. J. Lee, A. Urban, X. Li, D. Su, G. Hautier and G. Ceder, *Science*, 2014, **343(6170)**, 519-522.

30. R. A. House, L. Jin, U. Maitra, K. Tsuruta, J. W. Somerville, D. P. Förstermann, F. Massel, L. Duda, M. R. Roberts and P. G. Bruce, *Energy & Environmental Science*, 2018, **11**, 926-932.

31. N. Yabuuchi, M. Takeuchi, M. Nakayama, H. Shiiba, M. Ogawa, K. Nakayama, T. Ohta, D. Endo, T. Ozaki, T. Inamasu, K. Sato and S. Komaba, *Proceedings of the National Academy of Sciences of the United States of America*, 2015, **112**, 7650-7655.

32. M. A. Cambaz, A. Urban, S. A. Pervez, H. Geßwein, A. Schiele, A. A. Guda, A. L. Bugaev, A. Mazilkin, T. Diemant, R. J. Behm, T. Brezesinski and M. Fichtner, *Chemistry of Materials*, 2020, **32**, 3447-3461.

33. M. Winter and R. J. Brodd, *Chemical Reviews*, 2004, **104**, 4245-4270.

34. A. Manthiram, *Nature Communications*, 2020, **11**, 1550.

35. M. M. Thackeray and K. Amine, *Nature Energy*, 2021, **6**, 933-933.

36. G. Assat and J. M. Tarascon, *Nature Energy*, 2018, **3**, 373-386.

37. M. Ben Yahia, J. Vergnet, M. Saubanere and M. L. Doublet, *Nature Materials*, 2019, **18**, 496-502.

38. J. Rouxel, *Chemistry–A European Journal*, 1996, **2**, 1053-1059.

39. J. M. Tarascon, G. Vaughan, Y. Chabre, L. Seguin, M. Anne, P. Strobel and G. Amatucci, *Journal of Solid State Chemistry*, 1999, **147**, 410-420.

40. M. Aydinol, A. Kohan, G. Ceder, K. Cho and J. Joannopoulos, *Physical Review B*, 1997, **56**, 1354.

41. Z. Lu and J. R. Dahn, *Journal of the Electrochemical Society*, 2002, **149**, A815.

42. N. Yabuuchi, K. Yoshii, S. T. Myung, I. Nakai and S. Komaba, *Journal of the American Chemical Society*, 2011, **133**, 4404-4419.

43. H. Koga, L. Croguennec, M. Ménétrier, P. Mannessiez, F. Weill, C. Delmas and S. Belin, *The Journal of Physical Chemistry C*, 2014, **118**, 5700-5709.

44. M. Oishi, C. Yogi, I. Watanabe, T. Ohta, Y. Orikasa, Y. Uchimoto and Z. Ogumi, *Journal of Power Sources*, 2015, **276**, 89-94.

45. M. Sathiya, G. Rousse, K. Ramesha, C. P. Laisa, H. Vezin, M. T. Sougrati, M. L.

Doublet, D. Foix, D. Gonbeau, W. Walker, A. S. Prakash, M. Ben Hassine, L. Dupont and J. M. Tarascon, *Nature Materials*, 2013, **12**, 827-835.

46. E. McCalla, A. M. Abakumov, M. Saubanère, D. Foix, E. J. Berg, G. Rousse, M. L. Doublet, D. Gonbeau, P. Novák and G. J. S. Van Tendeloo, *Science*, 2015, **350**, 1516-1521.

47. D. H. Seo, J. Lee, A. Urban, R. Malik, S. Kang and G. Ceder, *Nature Chemistry*, 2016, **8**, 692-697.

48. R. A. House, U. Maitra, M. A. Perez-Osorio, J. G. Lozano, L. Jin, J. W. Somerville, L. C. Duda, A. Nag, A. Walters, K. J. Zhou, M. R. Roberts and P. G. Bruce, *Nature*, 2020, **577**, 502-508.

49. J. J. Marie, R. A. House, G. J. Rees, A. W. Robertson, M. Jenkins, J. Chen, S. Agrestini, M. Garcia-Fernandez, K. J. Zhou and P. G. Bruce, *Nature Materials*, 2024, **23**, 818-825.

50. W. E. Gent, K. Lim, Y. Liang, Q. Li, T. Barnes, S. J. Ahn, K. H. Stone, M. McIntire, J. Hong, J. H. Song, Y. Li, A. Mehta, S. Ermon, T. Tyliszczak, D. Kilcoyne, D. Vine, J. H. Park, S. K. Doo, M. F. Toney, W. Yang, D. Prendergast and W. C. Chueh, *Nature Communications*, 2017, **8**, 2091.

51. M. Okubo and A. Yamada, *ACS Applied Materials & Interfaces*, 2017, **9**, 36463-36472.

52. M. Saubanère, E. McCalla, J. M. Tarascon and M. L. Doublet, *Energy & Environmental Science*, 2016, **9**, 984-991.

53. J. Hong, W. E. Gent, P. Xiao, K. Lim, D. H. Seo, J. Wu, P. M. Csernica, C. J. Takacs, D. Nordlund, C. J. Sun, K. H. Stone, D. Passarello, W. Yang, D. Prendergast, G. Ceder, M. F. Toney and W. C. Chueh, *Nature Materials*, 2019, **18**, 256-265.

54. R. A. House, J. J. Marie, M. A. Pérez-Osorio, G. J. Rees, E. Boivin and P. G. Bruce, *Nature Energy*, 2021, **6**, 781-789.

55. M. D. Radin, J. Vinckeviciute, R. Seshadri and A. Van der Ven, *Nature Energy*, 2019, **4**, 639-646.

56. C. Delmas, C. Fouassier and P. Hagenmuller, *Physica B+C*, 1980, **99**, 81-85.

57. D. Mohanty, A. Huq, E. A. Payzant, A. S. Sefat, J. Li, D. P. Abraham, D. L. Wood, III and C. Daniel, *Chemistry of Materials*, 2013, **25**, 4064-4070.

58. G. C. Mather, C. Dussarrat, J. Etourneau and A. R. West, *Journal of Materials Chemistry*, 2000, **10**, 2219-2230.

59. C. Zhao, Q. Wang, Z. Yao, J. Wang, B. Sánchez-Lengeling, F. Ding, X. Qi, Y. Lu, X. Bai, B. Li, H. Li, A. Aspuru-Guzik, X. Huang, C. Delmas, M. Wagemaker, L. Chen and Y. S. Hu, *Science*, 2020, **370**, 708-711.

60. R. Stoyanova, D. Carlier, M. Sendova-Vassileva, M. Yoncheva, E. Zhecheva, D. Nihtianova and C. Delmas, *Journal of Solid State Chemistry*, 2010, **183**, 1372-1379.

61. B. C. Saha, A. K. Bera and S. M. Yusuf, *ACS Applied Energy Materials*, 2021, **4**, 6040-6054.

62. J. Paulsen and J. Dahn, *Journal of the Electrochemical Society*, 2000, **147**, 2478.

63. Z. Ruff, C. S. Coates, K. Märker, A. Mahadevegowda, C. Xu, M. E. Penrod, C. Ducati and C. P. Grey, *Chemistry of Materials*, 2023, **35**, 4979-4987.

64. A. Van der Ven, M. Aydinol, G. Ceder, G. Kresse and J. Hafner, *Physical Review B*, 1998, **58**, 2975.

65. Z. Chen, Z. Lu and J. Dahn, *Journal of the Electrochemical Society*, 2002, **149**, A1604.

66. Z. Lu and J. Dahn, *Journal of the Electrochemical Society*, 2001, **148**, A1225.

67. Z. Lu and J. R. Dahn, *Journal of the Electrochemical Society*, 2001, **148**, A710.

68. C. Delmas, J. J. Braconnier and P. Hagenmuller, *Materials Research Bulletin*, 1982, **17**, 117-123.

69. D. Carlier, I. Saadoune, L. Croguennec, M. Ménétrier, E. Suard and C. Delmas, *Solid State Ionics*, 2001, **144**, 263-276.

70. F. Tournadre, L. Croguennec, I. Saadoune, D. Carlier, Y. Shao-Horn, P. Willmann and C. Delmas, *Journal of Solid State Chemistry*, 2004, **177**, 2790-2802.

71. N. Yabuuchi, Y. Kawamoto, R. Hara, T. Ishigaki, A. Hoshikawa, M. Yonemura, T. Kamiyama and S. Komaba, *Inorganic Chemistry*, 2013, **52**, 9131-9142.

72. N. Yabuuchi, M. Kajiyama, J. Iwatate, H. Nishikawa, S. Hitomi, R. Okuyama, R. Usui, Y. Yamada and S. Komaba, *Nature Materials*, 2012, **11**, 512-517.

73. J. Paulsen, C. Thomas and J. Dahn, *Journal of the Electrochemical Society*, 2000, **147**, 861.

74. B. D. L. Campéon and N. Yabuuchi, *Chemical Physics Reviews*, 2021, **2**, 041306.

75. A. Urban, A. Abdellahi, S. Dacek, N. Artrith and G. Ceder, *Physical Review Letters*, 2017, **119**, 176402.

76. D. A. Kitchaev, Z. Lun, W. D. Richards, H. Ji, R. J. Clément, M. Balasubramanian,

D. H. Kwon, K. Dai, J. K. Papp, T. Lei, B. D. McCloskey, W. Yang, J. Lee and G. Ceder, *Energy & Environmental Science*, 2018, **11**, 2159-2171.

77. H. Ji, A. Urban, D. A. Kitchaev, D. H. Kwon, N. Artrith, C. Ophus, W. Huang, Z. Cai, T. Shi, J. C. Kim, H. Kim and G. Ceder, *Nature Communications*, 2019, **10**, 592.

78. R. J. Clément, D. Kitchaev, J. Lee and C. Gerbrand, *Chemistry of Materials*, 2018, **30**, 6945-6956.

79. J. Lee, D. A. Kitchaev, D. H. Kwon, C. W. Lee, J. K. Papp, Y. S. Liu, Z. Lun, R. J. Clement, T. Shi, B. D. McCloskey, J. Guo, M. Balasubramanian and G. Ceder, *Nature*, 2018, **556**, 185-190.

80. M. Nakajima and N. Yabuuchi, *Chemistry of Materials*, 2017, **29**, 6927-6935.

81. N. Yabuuchi, Y. Tahara, S. Komaba, S. Kitada and Y. Kajiya, *Chemistry of Materials*, 2016, **28**, 416-419.

82. W. D. Richards, S. T. Dacek, D. A. Kitchaev and G. Ceder, *Advanced Energy Materials*, 2018, **8**, 1701533.

83. J. Lee, J. K. Papp, R. J. Clément, S. Sallis, D. H. Kwon, T. Shi, W. Yang, B. D. McCloskey and G. Ceder, *Nature Communications*, 2017, **8**, 981.

84. Y. Shirazi Moghadam, A. El Kharbachi, T. Diemant, G. Melinte, Y. Hu and M. Fichtner, *Chemistry of Materials*, 2021, **33**, 8235-8247.

85. Z. Lun, B. Ouyang, D. A. Kitchaev, R. J. Clément, J. K. Papp, M. Balasubramanian, Y. Tian, T. Lei, T. Shi, B. D. McCloskey, J. Lee and G. Ceder, *Advanced Energy Materials*, 2019, **9**, 1802959.

86. N. Takeda, I. Ikeuchi, R. Natsui, K. Nakura and N. Yabuuchi, *ACS Applied Energy Materials*, 2019, **2**, 1629-1633.

87. H. Ji, D. A. Kitchaev, Z. Lun, H. Kim, E. Foley, D. H. Kwon, Y. Tian, M. Balasubramanian, M. Bianchini, Z. Cai, R. J. Clément, J. C. Kim and G. Ceder, *Chemistry of Materials*, 2019, **31**, 2431-2442.

88. Q. Wang, A. Sarkar, D. Wang, L. Velasco, R. Azmi, S. S. Bhattacharya, T. Bergfeldt, A. Düvel, P. Heitjans, T. Brezesinski, H. Hahn and B. Breitung, *Energy & Environmental Science*, 2019, **12**, 2433-2442.

89. Z. Lun, B. Ouyang, Z. Cai, R. J. Clement, D. H. Kwon, J. Huang, J. K. Papp, M. Balasubramanian, Y. Tian, B. D. McCloskey, H. Ji, H. Kim, D. A. Kitchaev and G. Ceder, *Chem*, 2020, **6(1)**, 153-168.

90. A. Van der Ven, *Electrochemical and Solid-State Letters*, 1999, **3**, 301.

91. A. Van der Ven, J. Bhattacharya and A. A. Belak, *Accounts of Chemical Research*, 2013, **46**, 1216-1225.

92. M. Catti, *Physical Review B*, 2000, **61**, 1795-1803.

93. A. Urban, J. Lee and G. Ceder, *Advanced Energy Materials*, 2014, **4**, 1400478.

94. K. Kang, S. Meng Ying, J. Bréger, P. Grey Clare and G. Ceder, *Science*, 2006, **311**, 977-980.

95. K. Kang and G. Ceder, *Physical Review B*, 2006, **74(9)**, 094105.

96. V. Pralong, V. Gopal, V. Caignaert, V. Duffort and B. Raveau, *Chemistry of Materials*, 2012, **24**, 12-14.

97. L. Zhang and H. Noguchi, *Journal of the Electrochemical Society*, 2003, **150**, A601.

98. K. Ozawa, Y. Nakao, L. Wang, Z. Cheng, H. Fujii, M. Hase and M. Eguchi, *Journal of Power Sources*, 2007, **174**, 469-472.

99. J. Lee, C. Wang, R. Malik, Y. Dong, Y. Huang, D.-H. Seo and J. Li, *Advanced Energy Materials*, 2021, **11**, 2100204.

100. D. Chen, J. Wu, J. K. Papp, B. D. McCloskey, W. Yang and G. Chen, *Small*, 2020, **16**, 2000656.

101. D. Chen, W. H. Kan and G. Chen, *Advanced Energy Materials*, 2019, **9**, 1901255.

102. D. Chen, J. Ahn, E. Self, J. Nanda and G. Chen, *Journal of Materials Chemistry A*, 2021, **9**, 7826-7837.

103. L. Li, Z. Lun, D. Chen, Y. Yue, W. Tong, G. Chen, G. Ceder and C. Wang, *Advanced Functional Materials*, 2021, **31**, 2101888.

104. W. H. Kan, D. Chen, J. K. Papp, A. K. Shukla, A. Huq, C. M. Brown, B. D. McCloskey and G. Chen, *Chemistry of Materials*, 2018, **30**, 1655-1666.

105. H. Li, R. Fong, M. Woo, H. Ahmed, D. H. Seo, R. Malik and J. Lee, *Joule*, 2022, **6**, 53-91.

106. D. H. Kwon, J. Lee, N. Artrith, H. Kim, L. Wu, Z. Lun, Y. Tian, Y. Zhu and G. Ceder, *Cell Reports Physical Science*, 2020, **1**, 100187.

2

Experimental Techniques

Contents

2.1 Materials Synthesis

2.1.1 Solid-State Method

Solid-state synthesis, also known as the ceramic method, is a chemical process where solid starting materials are reacted at high temperatures to form a new solid with a well-defined structure, including polycrystalline materials and single crystals which are widely used for energy and electronic applications.[1]

This thesis utilized solid-state method to synthesize layered oxide and DRX oxide materials. Stoichiometric (sometimes excess to compensate for the vaporisation at high temperature) metal-oxide (or carbonate/nitrate/hydroxide) powders are intimately wet-mixed in a certain amount of solvents (ethanol/acetone) to create a uniform precursor blend and reduce the diffusion length of ions during reaction. Mixing is typically accomplished by low-energy ball-milling (*e.g.* 200–500 rpm for 2–12 hrs). The dried mixture is then pressed into pellets (~10 mm diameter, 1–2 mm thick) under 2–5 tons hydraulic pressure, ensuring intimate particle contact and minimal porosity.

Pelletized precursors are heated in a tube or box furnace at 500–1500 °C for 10–48 hrs, depending on the targeted composition. During heating, ions gain sufficient thermal energy to overcome lattice barriers and diffuse across grain boundaries, allowing the formation of the desired mixed-metal oxide phase. The dwell temperature and time must be chosen to balance reaction kinetics against grain growth to obtain the targeted structure and crystalline size. Usually, the higher temperature and longer dwell time enable a bigger crystalline size.

The atmosphere for solid-state synthesis is a crucial factor that influences the reaction

and the final product, especially for tuning the TM oxidation states due to the oxygen partial pressure. The mechanism can be depicted by the following equation:

$$\mathrm{TM}_x\mathrm{O}_y(s) \leftrightarrow \mathrm{TM}_x\mathrm{O}_{y-z}(s) + \frac{z}{2}\mathrm{O}_2(g) \quad (2.1)$$

Common atmospheres, such as oxygen and high-pressure air, can have high oxygen partial pressure which shifts the equilibrium in Equation 2.1 to the left, resulting in higher oxidation states for the TMs. While gases like argon or nitrogen, despite being inert, can reduce the TMs during calcination due to the entropy gain from evolving O_2 gas, thus shifting the equilibrium to the right. Sometimes, mildly reducing gas (5 % H_2/Ar) can be used for further reduction of TMs.

Finally, the cooling profile, whether through rapid quenching or slow ramping, significantly influences the degree of short-range order. Quenching "locks in" high-temperature disorder. Synthesis of DRX materials usually applies quenching or nature colling. While slow cooling can encourage local ordering, like TM-layer superstructure in layered materials or SRO in DRXs.

2.1.2 Mechanochemical Ball-Milling

In battery research including this thesis, mechanochemical ball-milling is particularly useful for preparing DRX cathodes and fluoride-substituted materials, where kinetic stabilization of metastable phases is desired. This approach offers a greener alternative to traditional solution-based methods by eliminating the need for organic solvents and potentially reducing energy consumption. The process involves grinding solid reactants with milling balls, generating high shear forces, localised heating and high pressures. These conditions allow chemical bonds to break and facilitate the formation of new products,

including metastable phases that cannot be achieved by conventional solid-state method.[2]

In a typical procedure, precursor powders (*e.g.* metal, metal oxides, or halides that will not release gas during reaction) are combined with grinding balls in sealed hardened steel, zirconia, or tungsten jars. As shown in **Figure 2.1**, the jars are subjected to rapid oscillations or rotations at frequencies of 300–1000 rpm using a planetary or shaker-type mill. The resulting collisions between grinding balls and powder particles lead to particle size reduction, local heating, and the formation of high-energy defect states, all of which accelerate diffusion and reaction rates. Key parameters controlling the outcome of mechanochemical synthesis include milling time, rotation speed, ball-to-powder ratio (BPR), and the type and size of milling media. Longer milling durations and higher BPRs generally favour complete mixing and amorphization but may also lead to contamination or over-milling, especially with ductile materials.

Figure 2.1: Illustration of the planetary ball mill instrument and the reaction process for the material synthesis in this thesis. Part of figure from the user manual provided by Fritsch®.

2.1.3 Ion exchange

Ion exchange is a post-synthetic method widely employed to modify the AM content in layered oxide frameworks without disrupting the overall crystal structure. It enables the replacement of pre-existing cations (typically Na^+ or Li^+) in the interlayer sites with alternative alkali or alkaline-earth ions through topochemical reactions driven by differences in ionic radii and chemical potential. This method is particularly valuable for synthesizing metastable compositions or accessing phases that are difficult to obtain via direct solid-state routes.

In a typical ion exchange process, a parent compound, often a layered Na-based oxide with a well-defined structure, is intimately mixed with an excess of lithium sources and heated to promote reaction kinetics.[3] For low-temperature exchange, the parent oxide is refluxed for 10-100 hrs in a hexanol/methanol solution of LiCl/LiBr at 60-200 °C, enabling gradual replacement of Na^+ by Li^+.[4] Another procedure is to directly mix parent oxide with the liquid molten salt, for example a eutectic composition of $LiNO_3$-LiCl (typically 0.88:0.12 molar ratio) with melting point around 280 °C.[5]

In this thesis, the low-temperature reflux method was employed to convert ribbon-ordered $Na_{0.52}Li_{0.2}Mn_{0.8}O_2$ into its Li-based counterpart $Li_{0.56}Li_{0.2}Mn_{0.8}O_2$ while preserving the superstructure within TM layer, enabling a direct comparison of migration behavior and structural evolution between the two alkali compositions.

2.2 Long-range Structural Characterization

2.2.1 Powder X-ray and Neutron Diffraction

Diffraction is a fundamental wave behaviour that occurs when waves encounter

obstacles, particularly when the dimensions of such features are comparable to the wavelength of the incident wave. This phenomenon leads to the redistribution of wave intensity and forms the basis for a range of structural characterization techniques.

Powder X-ray Diffraction (PXRD)

The discovery of X-rays by Wilhelm C. Röntgen in 1895 marked a turning point in the development of structural science. Shortly thereafter, William H. Bragg and William L. Bragg demonstrated that crystalline materials could diffract X-rays, leading to the establishment of X-ray crystallography.[6] X-ray diffraction is based on the interaction of a monochromatic X-ray beam with the atoms of a crystalline solid material whose atomic structure exhibits long-range order. A crystalline material can be modelled as atomic planes separated by a distance *d*, as illustrated in **Figure 2.2**. These atomic planes are characterized by Miller indices, which are the inverse values of where the planes intercept with the *a*, *b* and *c* crystallographic axes respectively. The conditions for diffraction are given by Bragg's law:

$$n\lambda = 2d_{hkl} \sin\theta \qquad (2.2)$$

where λ is the wavelength of the incident radiation, d_{hkl} is the distance between lattice planes with Miller indices (hkl), θ is the angle of incidence, and n is an integer.

Constructive interference, and therefore the appearance of a diffraction peak, occurs when this condition is met, as shown in **Figure 2.2**. For direct comparison with diffraction data collected from X-rays or other neutron sources, diffraction patterns can be converted into intensity versus the scattering vector, a wavelength-independent unit, which can be calculated using the equation below:

$$\vec{Q} = \vec{G} = \frac{n2\pi}{\vec{d}_{hkl}} \tag{2.3}$$

Here $\vec{Q}$ represents the difference of incoming and scattered wavevector (in the common case of elastic scattering $\vec{Q}$ = 4πsin(θ)/λ and $\vec{G}$ is a vector of the reciprocal lattice.

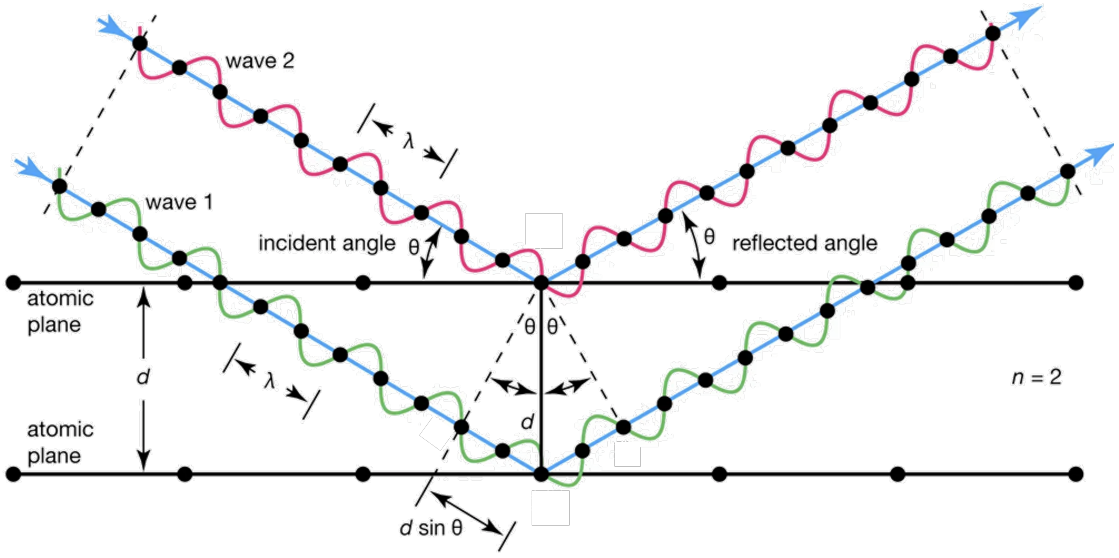

Figure 2.2: Illustration of Bragg's law for X-ray diffraction. Figure from ©Encyclopaedia Britannica, Inc.

Hence, Equation 2.2 indicates that diffraction occurs only when the momentum transfer from the incident wave to the crystal lattice corresponds to a reciprocal lattice vector. Each time this condition is satisfied, a Bragg reflection is observed. The intensity of each Bragg peak depends on the scattering power of the atoms occupying the corresponding crystallographic planes (hkl).

The diffracted intensity of a given peak is therefore closely linked to the atomic arrangement within the unit cell. Because X-rays interact primarily with electron clouds, atoms with higher atomic numbers contribute more strongly to the scattered intensity. This relationship is quantitatively described by the structure factor:

$$I_{hkl} \propto |F_{hkl}|^2 = \sum_{j=1}^{n} O_j f_j e^{i2\pi(hx_j+ky_j+lz_j)} \quad (2.4)$$

Here, f_j is the atomic form factor, (x_j, y_j, z_j) are the fractional coordinates of atom j, and O_j is the site occupancy. The summation accounts for the contributions of all atoms in the unit cell to the diffracted intensity.

It is worth noting that, while X-ray diffraction was initially developed for single-crystal studies, substantial advancements have since been made to enable the analysis of polycrystalline and powdered materials. Among these, PXRD has become a widely adopted technique for polycrystalline specimens with randomly oriented grains, such as those typically produced by solid-state synthesis.

When a monochromatic X-ray beam is directed onto a powdered sample, the condition for constructive interference is satisfied in all spatial orientations. As a result, PXRD can be viewed as effectively averaging over one angular dimension, leaving θ as the sole variable. The diffracted beams form cones that intersect a flat detector as a series of concentric rings, each appearing at a specific angle θ that satisfies Bragg's law. The angular positions of these rings provide information about interplanar spacings and, consequently, the unit cell parameters and space group of the material, while the intensity distribution within each ring reflects the atomic arrangement within the unit cell.

A major milestone in crystallographic analysis was the introduction of the Rietveld refinement method by Hugo Rietveld in 1969. This technique transformed the interpretation of PXRD data by enabling the quantitative refinement of complex structural models. Starting from an initial structural hypothesis reasonably close to the actual

configuration, the Rietveld method iteratively adjusts parameters to minimize the difference between the calculated and observed diffraction patterns. This iterative process continues until convergence is achieved, providing a highly reliable and self-consistent representation of the crystal structure. In this thesis, the refined parameters include atomic positions, lattice constants, occupancies, and thermal factors.

The quality of Rietveld refinements is commonly assessed using the weighted-profile R-factor (wR) and the goodness-of-fit (GOF). The wR value quantifies the agreement between observed and calculated patterns, with lower values indicating better fits (typically, values below 10% are considered good for crystalline materials). The GOF, or reduced chi-squared (χ^2), measures how well the model describes the data relative to experimental uncertainties. A GOF value close to 1.0 suggests an excellent fit within experimental error. Both metrics are reported throughout this thesis to ensure the reliability of the refined structural models.

Powder Neutron Diffraction

Neutrons are electrically neutral subatomic particles discovered by James Chadwick in 1932, residing within atomic nuclei. Unlike X-rays, which primarily interact with electron clouds, neutrons interact directly with atomic nuclei, granting them unique advantages for structural analysis. One important property is that neutron coherent scattering lengths vary irregularly with atomic number and even between isotopes, resulting in highly element-specific and sometimes isotope-specific contrast. This feature makes neutrons particularly sensitive to light elements such as lithium and oxygen and enhances the ability to distinguish between neighboring TMs, even when their atomic numbers are

similar.[7]

Additionally, because neutrons interact only weakly with matter, they possess high penetration depths, enabling true bulk-sensitive characterization with minimal beam-induced damage to the sample which is an important consideration for delicate electrode materials. However, this weak interaction also means that relatively large sample quantities (typically >1 g) are required to obtain sufficient signal intensity for neutron diffraction experiments. These properties make PND an invaluable technique for studying the structure and evolution of battery electrode materials, both in their pristine form and after electrochemical cycling.

The interaction of neutrons with matter can be categorized into three primary processes:

a) Coherent elastic scattering: This leads to diffraction and provides information on long-range order.
b) Incoherent elastic scattering: Results in isotropic background signals and arises from random phase relationships due to isotope mixtures.
c) Absorption: Certain elements (*e.g.*, boron, cadmium, lithium) exhibit high neutron absorption cross-sections and require careful consideration in experimental design.

In neutron diffraction, the intensity of a reflection is calculated using a similar formalism to X-ray diffraction, but with the atomic form factors f_j replaced by nuclear scattering lengths b, which quantifies the amplitude of the neutron–nucleus interaction.

2.2.2 Selected Area Electron Diffraction

Electron diffraction, particularly when performed within a transmission electron microscope, is a powerful technique used to characterize the crystal structure of materials by analysing the diffraction pattern produced when a beam of electrons elastically interacts with atoms.[8] Unlike X-ray diffraction, which provides an averaged structure over large volumes, electron diffraction enables high-resolution analysis of small volumes of material, capable of nanoparticle characterization, subtle superstructure identification and defect analysis.[9]

In this thesis, selected area electron diffraction (SAED) was employed to determine crystalline phase, extract lattice parameters, and probe local crystallographic features such as short-range order in DRXs and superstructure in layered oxides. A small amount of powdered sample was ultrasonicated in ethanol and drop-cast onto a lacey carbon-coated copper grid before being introduced into the TEM under high-vacuum conditions. Diffraction patterns were acquired using a selected area aperture to isolate crystalline domains of ~100–500 nm in size. The patterns were indexed against known structures or compared with simulated patterns to aid interpretation.

2.2.3 Scanning Electron Microscopy

SEM is a widely used technique for characterizing the morphology and surface features of cathode materials at micro- to sub-micrometre length scales. In SEM, a focused electron beam is rastered across the sample surface, generating secondary and backscattered electrons whose intensities provide topographical and compositional contrast.[10] This makes SEM particularly useful for assessing particle size, morphology, agglomeration, and surface texture, all of which influence the electrochemical behaviour

of battery materials.

In this thesis, SEM imaging was performed on loose powder samples, which were dispersed onto conductive carbon tape to minimize agglomeration and ensure representative imaging. The high spatial resolution of SEM enabled the visualization of primary particle sizes, surface roughness, and the presence of interparticle pores or cracks. Energy-dispersive X-ray spectroscopy (EDX) mapping was performed in conjunction with SEM. EDX mapping allowed for quantitative and spatially resolved identification of elemental distribution within the cathode powders, verifying both the uniformity of elemental incorporation and the absence of significant phase segregation or compositional inhomogeneity. The simultaneous collection of secondary electron images and EDX maps facilitates direct correlation between structural features and local composition, providing a robust means to confirm the efficacy of synthesis protocols, especially for multi-component or doped materials.

2.3 Short-range Structural Characterization

2.3.1 Total Scattering and Pair Distribution Function Analysis

Unlike conventional powder diffraction, which focuses solely on Bragg reflections and thus probes only the average long-range periodic structure, total scattering data contains both Bragg and diffuse scattering on an equal basis. Diffuse scattering, often ignored in traditional analysis, contains valuable information about local structural correlations and disorder.[11]

Fourier transformation of this total-scattering data into real space yields the atomic

pair distribution function (PDF), which describes the probability of finding pairs of atoms separated by a distance *r*. The peak positions in *G(r)* correspond to interatomic distances, their intensities are weighted by the scattering lengths of the contributing atom pairs, and their widths provide information on atomic disorder, displacements, and thermal vibrations. PDF analysis can probe local and intermediate-range structures, such as cation mixing, defect clustering, or local distortions, even in amorphous or highly disordered systems.

In this thesis, X-ray PDF analysis enables the detailed mapping of element occupancy, TM migration pathways, and local defect domains in DRX cathodes, providing essential insights into their electrochemical behavior.

2.3.2 Scanning Transmission Electron Microscopy

STEM provides atomic-scale structural and chemical information by combining the high-resolution imaging of TEM with a focused, scanned electron probe. In this mode, a finely converged electron beam is rastered across a thin specimen, and annular detectors collect the transmitted electrons to produce images with contrast that depends on atomic number, thickness, and diffraction effects.[12]

In this thesis, ADF-STEM, also known as Z-contrast imaging, was employed to visualize cation arrangements and local ordering motifs in layered oxide cathodes. Because the ADF signal intensity scales approximately with the square of the atomic number, this technique enables direct imaging of transition-metal distributions and the identification of short-range superstructures or slab gliding in layered materials. Annular bright-field (ABF)-STEM is another mode that is necessary when detecting lighter elements such as oxygen. STEM imaging provides critical insight into the atomic-scale disorder, cation

distribution, and defect domains in these cathode materials, complementing bulk-averaged techniques such as XRD and PDF.

2.3.3 Nuclear Magnetic Resonance

Solid-state nuclear magnetic resonance (NMR) spectroscopy provides element-specific insights into the local chemical and electronic environments of nuclei, making it particularly valuable for studying short-range structure, ion dynamics, and disorder in battery materials. In NMR, nuclei with non-zero spin placed in a static magnetic field absorb and re-emit radiofrequency energy at characteristic resonance frequencies determined by their local magnetic environment. These frequencies are influenced by shielding from surrounding electrons, dipolar and quadrupolar interactions, and paramagnetic effects from transition-metal ions.

In this thesis, ^{7}Li and ^{23}Na magic-angle spinning (MAS) NMR were employed to probe the local environments of alkali ions in layered oxide cathodes. MAS NMR is employed to rotate the sample at 54.74° relative to the external magnetic field to average out anisotropic interactions, improving spectral resolution. For paramagnetic systems, the broadening and shifting of NMR resonances provided qualitative and semi-quantitative information about cation coordination and short-range ordering. These measurements were particularly useful for distinguishing alkali-ion occupancies in different crystallographic sites (*e.g.*, AM vs TM layers) and for detecting local disorder or ion-exchange heterogeneity that may not be captured by different techniques.

2.3.4 Electron Paramagnetic Resonance

Electron paramagnetic resonance (EPR) spectroscopy is a sensitive technique for detecting unpaired electron spins, providing information about oxidation states, electronic configurations, and the local environments of paramagnetic centers. EPR is analogous to NMR, although it is sensitive to electron spins rather than nuclear spins. Both techniques rely on the interaction of magnetic moments with an external magnetic field to probe the structure and dynamics of materials.[13]

When a sample is placed in a static magnetic field and exposed to microwaves, resonance absorption occurs when the energy matches the Zeeman splitting of spin states, which can be expressed as

$$h\nu = g\mu_B B \tag{2.5}$$

where h is Planck's constant, ν is the microwave frequency, μ_B is the Bohr magneton, B is the magnetic field strength, and g is the spectroscopic splitting factor (g-factor), which reflects the local electronic environment of the paramagnetic species. Deviations of g from the free electron value (2.0023) provide insight into covalency, ligand field effects, and local symmetry distortions.

In this thesis, EPR was employed to detect paramagnetic species in Ni-based DRX cathodes at various SOCs, with a particular focus on identifying oxidized oxygen species at high SOCs.

2.4 Spectroscopic Characterization

2.4.1 X-ray Absorption Spectroscopy

X-ray Absorption Spectroscopy (XAS) is an element-specific technique that provides

insights into the electronic structure and local chemical environment of atoms in materials. When a monochromatic X-ray beam irradiates a sample, core-level electrons can be excited when the incident photon energy matches or exceeds their binding energy, leading to the ejection of a photoelectron and the creation of a core hole (**Figure 2.3**).

Figure 2.3: *The figure originally presented here cannot be made freely available via ORA because of copyright. The figure was sourced at bibliographic reference Chantler et al.*[14]

The nature of the transition depends on the initial and final states of the electron. **Figure 2.4** illustrates common X-ray absorption edges, labelled by the atomic orbital according to the principal quantum number of the initial electron state. For instance, the K-edge corresponds to the excitation of a 1*s* electron, while the L-edge corresponds to 2*p* electrons. The transitions obey the dipole selection rules, primarily allowing $\Delta l = \pm 1$. This means that K-edge excitations probe unoccupied *p*-like states (*e.g.*, Mn/Ni $1s \rightarrow 4p$, Nb $1s \rightarrow 5p$, O $1s \rightarrow 2p$), while L-edge transitions are sensitive to unoccupied *d* states (*e.g.*, W $2p \rightarrow 5d$). The probability of quadrupolar transitions ($\Delta l = \pm 2, 0$) is about 100 times smaller than that of dipole transitions, which sometimes give rise to the pre-edge feature reflecting the coordination geometry.

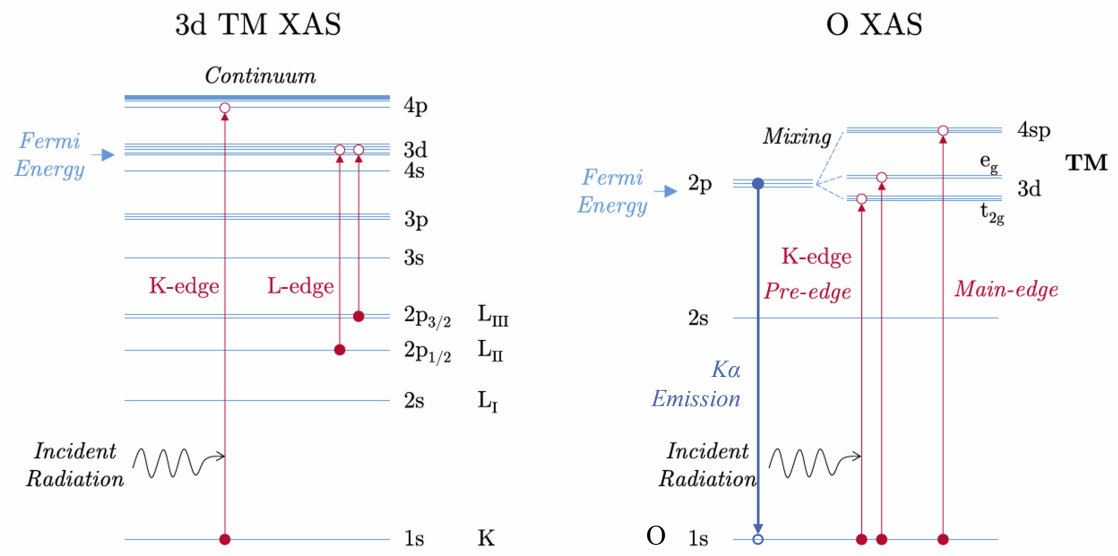

Figure 2.4: *The figure originally presented here cannot be made freely available via ORA because of copyright. The figure was sourced at bibliographic reference House et al.*[15]

The attenuation of the X-ray beam by the sample is described by the Beer–Lambert law:

$$I_t = I_0 e^{-\mu(E)\rho x} \tag{2.6}$$

$$\mu(E) \propto \log\left(\frac{I_0}{I_t}\right) \tag{2.7}$$

where I_o and I_t are the measured intensities of the incident and transmitted (or reflected) light respectively, $\mu(E)$ is the absorption coefficient, ρ is the material density, and x is the thickness of sample. In experimental measurements, the density and thickness of sample must be carefully optimized to ensure that the transmitted intensity is sufficiently high for reliable detection, but not so high as to cause detector saturation. The X-ray absorption coefficient increases sharply at the threshold energy, resulting in an absorption edge. The position and shape of this edge provide a distinct signature of the electronic and structural

environment of the absorber.

Since the attenuation coefficient μ(E) is energy-dependent, the effective probe depth changes accordingly with the incident energy. Soft XAS typically operates in the 100–2000 eV range, making it highly surface-sensitive and suitable for probing low-energy absorption edges such as O K-edge or TM L-edges. Hard XAS, with photon energies above 2 keV, penetrates deeper into materials and is typically used for TM K-edges and heavy element L-edges (*e.g.*, Nb K-edge at ~19 keV, W L_3-edge at ~10 keV). Due to the energy-dependent penetration depth, experiments with hard X-ray radiation can often be performed in transmission mode, reflecting the bulk nature of the particles, whereas soft X-rays are generally restricted to reflection geometries, like fluorescence yield mode. **Figure 2.5** shows the setup of these two detection modes.

Figure 2.5: *The figure originally presented here cannot be made freely available via ORA because of copyright. The figure was sourced at bibliographic reference Chantler et al.*[14]

XANES and EXAFS (Hard X-ray Absorption Spectroscopy)

For hard X-ray absorption, the spectrum is typically divided into two regions: X-ray Absorption Near Edge Structure (XANES) and Extended X-ray Absorption Fine Structure (EXAFS), as shown in **Figure 2.6**.

Figure 2.6: *The figure originally presented here cannot be made freely available via ORA because of copyright. The figure was sourced at bibliographic reference Chantler et al*[14] *and from Figure Munzarin at English Wikipedia, CC BY-SA 3.0.*

XANES (~−20 to +50 eV relative to the edge) provides information on the oxidation state, coordination geometry, and unoccupied density of states. Pre-edge features can indicate specific orbital hybridizations (*e.g.*, 1s → 3d quadrupole transitions).

EXAFS (50–1000 eV beyond the edge) contains oscillatory features arising from

interference between the outgoing photoelectrons from the absorbing atom and those scattered by neighboring atoms, allowing quantitative determination of interatomic distances, coordination numbers, and structural disorder.

Soft X-ray Absorption Spectroscopy

Soft X-ray Absorption Spectroscopy (sXAS) probes light elements (*e.g.*, O K-edge) and TM L-edges, offering insights into valence states and metal–ligand interactions. Detection typically uses Total Electron Yield (TEY), Total Fluorescence Yield (TFY), or Inverse Partial Fluorescence Yield (IPFY), each with different sensitivities to surface versus bulk contributions.[16] TEY measures the drain current generated by the emission of electrons from the surface, resulting in a probing depth of only a few nanometers and thus providing highly surface-sensitive information. TFY, in contrast, collects the emitted X-ray fluorescence photons from a greater depth, yielding more bulk-sensitive information. However, TFY can suffer from self-absorption effect, which arise when the emitted fluorescence photons are reabsorbed by the sample itself before escaping. For example, in 3*d* TM layered oxides, the emission energy of fluorescence photons from TM is close to the absorption energy of O. This effect distorting the spectral intensity and reducing quantitative accuracy, especially for concentrated or thick samples.[17] To overcome these limitations, IPFY mode frequently employed to more accurately probe the bulk electronic structure. IPFY data are typically extracted from mRIXS datasets. In the case of TM-L IPFY, the intensity of the O Kα emission generated following the excitation at TM-L edge is measured and then mathematically inverted, producing a spectrum close to the true X-ray absorption coefficient.

Experimental Setup

XAS experiments in this study were performed at synchrotron radiation facilities due to their high-brightness and tunable X-ray sources. Monochromatic X-rays were selected using a double-crystal monochromator, ensuring a narrow energy bandwidth. Measurements were conducted in either transmission or fluorescence detection mode, depending on sample concentration and thickness.

For transmission measurements, samples were prepared as homogeneous pellets (mixed with boron nitride if required) and mounted in appropriate holders. For dilute or highly absorbing samples, fluorescence detection using a multi-element solid-state detector was employed to improve sensitivity. Reference metal foils (*e.g.*, Ni or Mn foils) were measured simultaneously for energy calibration.

Data Analysis

The acquired raw absorption spectra were first normalized by subtracting pre-edge baselines and scaling post-edge regions to unity using the ATHENA program within the Demeter software package.[18] The energy scale was calibrated using the simultaneously measured metal foil reference. For EXAFS analysis, background subtraction and isolation of $\chi(k)$ oscillations were performed in k-space (photoelectron wavevector), followed by Fourier transformation to R-space to obtain radial distribution functions around the absorbing atom. Quantitative fitting of the EXAFS data was carried out using the ARTEMIS module, with theoretical scattering paths generated by the FEFF code. Structural parameters such as interatomic distances, coordination numbers, and Debye–Waller factors were refined iteratively to achieve the best agreement between experimental and theoretical

spectra.

2.4.2 Resonant Inelastic X-ray Scattering

RIXS is an element- and orbital-selective technique that probes two-photon resonant processes by measuring the energy difference between incident and scattered X-ray photons across the selected absorption edge.[19] As illustrated in **Figure 2.4 (right)**, the incident energy is tuned to a core-level absorption edge (*e.g.*, the O-K edge for oxygen redox studies), resonantly exciting an electron to an unoccupied state, leaving a core-hole in the O1*s* orbital. The subsequent radiative decay produces an emitted photon from the filled valence states down into the core-hole with an energy loss that reflects various elementary excitations, such as dd-excitations, charge-transfer processes, and vibrational modes.

In battery materials, high-resolution O-K edge RIXS has proven especially powerful for identifying oxidized oxygen species. Of particular interest is the detection of molecular O_2 formed during high-voltage charging. This is recognized by a series of sharp, intense peaks in the low-energy-loss region (typically 0.01–1 eV). Illustration in **Figure 2.7** reveals that the energy spacing between successive peaks gradually decreases with increasing energy loss, consistent with the anharmonic vibrational behavior of diatomic molecules approaching bond dissociation. Notably, the spacing between the first two peaks (≈0.192 eV, or ≈1550 cm^{-1}) matches the fundamental vibrational frequency of molecular O_2.[20]

Mechanistically, after photon absorption (*e.g.*, at ~531 eV), O_2 is promoted to an electronically excited state. When this state relaxes via radiative decay, the molecule can settle into a higher vibrational energy level of its electronic ground state. This energy difference reduces the emitted photon energy by an amount equal to the vibrational

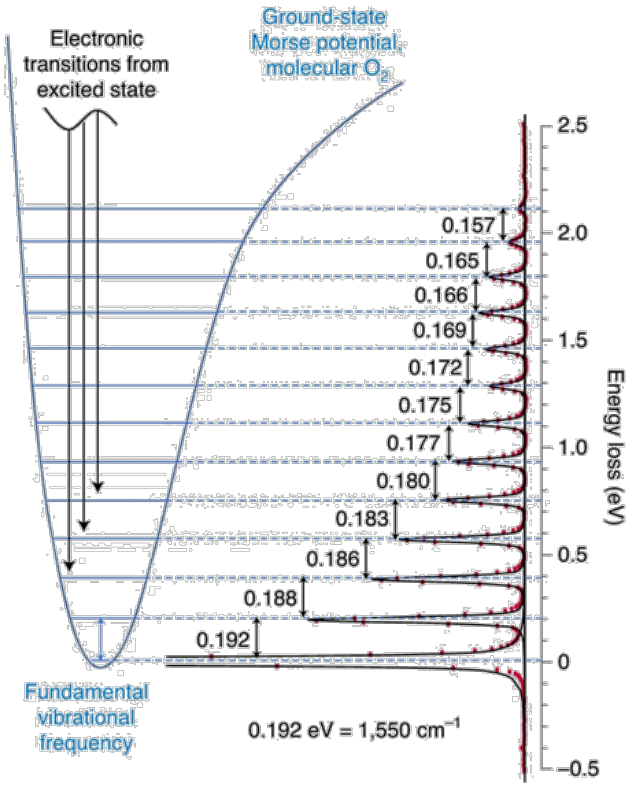

Figure 2.7: Schematic illustrating the origin of the RIXS peak progression derived from the vibrational energy levels of an anharmonic oscillating O_2 diatomic. Figure adapted from House *et al.*[20]

transition, giving rise to the observed vibrational progression in the RIXS spectrum. This phenomenon parallels infrared or Raman vibrational spectroscopy, but here the vibrational progression is revealed through an electronic decay process rather than vibrational transitions alone.

In this thesis, high-resolution RIXS was used alongside XAS to characterize the evolution of oxygen states in disordered rock-salt cathodes at high charge. This combined approach provided direct evidence for oxygen participation in the redox process, distinguishing molecular O_2 species from conventional transition-metal redox contributions.

2.5 Composition Analysis Methods

2.5.1 Inductively Coupled Plasma-Optical Emission Spectrometry

Inductively coupled plasma–optical emission spectrometry (ICP-OES) is a quantitative analytical technique used to determine elemental composition in solid or liquid samples with high sensitivity and accuracy. The sample is first dissolved, typically in strong acids such as HCl or HNO_3, then diluted to a predefined concentration. This solution is then introduced into the ICP-OES system as an aerosol formed by a nebulizer and ejected through an argon plasma torch. At plasma temperatures of 6000–10,000 K, the sample's constituent atoms and ions are excited to higher electronic states. As a result, when they relax back to lower energy states, they emit photons at characteristic wavelengths unique to each element.

The emitted light is dispersed and detected by a spectrometer, the intensity of these emission lines being directly proportional to the elemental concentration in the sample. Calibration against standards of known composition enables quantitative determination of target elements, often down to parts-per-million levels.

In this thesis, ICP-OES was employed to determine the precise elemental ratios of TMs and alkali ions in synthesized cathode materials. These measurements were crucial for confirming nominal stoichiometry, assessing the efficiency of ion-exchange reactions, and ensuring the reproducibility of solid-state synthesis routes.

2.5.2 Fluoride Ion-Selective Electrode

Fluoride ion–selective electrode (F^--ISE) are potentiometric devices used to determine the concentration of free fluoride ions in solution. The electrode consists of a lanthanum

fluoride (LaF_3) crystal membrane doped with europium(II), which selectively conducts fluoride ions.[21] When immersed in a sample solution, the electrode develops a potential difference relative to a reference electrode, governed by the Nernst equation:

$$E = E^0 - \frac{RT}{nF}\ln[\mathrm{F}^-] \tag{2.8}$$

where E is the measured potential, E^0 is the standard potential, R is the gas constant, T is the temperature, n is the charge of the ion (−1 for fluoride), F is the Faraday constant, and $[F^-]$ is the fluoride ion concentration.

To ensure measurement accuracy, a Total Ionic Strength Adjustment Buffer (TISAB) was used to maintain constant ionic strength and pH, preventing interference from polyvalent cations and enabling reliable fluoride activity measurement.

In this thesis, F^--ISE measurements were performed using METTLER TOLEDO SevenExcellence™ benchtop meter accompanied with perfectION™ Combination Fluoride Electrode to quantify the fluorine content in oxyfluoride cathode materials after sample dissolution. This method provided the verification of the fluoride content in the synthesized DRX oxyfluoride compounds.

2.5.3 Iodometry Titration

Iodometric titration is a classical redox titration technique used to determine the average oxidation state of TMs, particularly in mixed-valent oxide materials.[22] The method relies on the reduction of higher-valent transition-metal ions by iodide in an acidic solution, producing iodine according to:

$$2\mathrm{I}^- \rightarrow \mathrm{I}_2 + 2e^- \tag{2.9}$$

The liberated iodine is then titrated with a standardized sodium thiosulfate solution:

$$I_2 + 2S_2O_3^{2-} \rightarrow 2I^- + S_4O_6^{2-} \quad (2.10)$$

The endpoint is typically detected using a starch indicator, which forms a deep blue complex with iodine that disappears when all free iodine has been reduced.

In this thesis, iodometric titration was employed to verify the oxidation state of Mn in disordered rock-salt oxyfluorides and further confirm the concise composition of as-prepared material with the combination of ICP and F^--ISE. To ensure accurate measurements, the entire process was carried out under an Ar flow to prevent unwanted oxidation or reduction reactions. This information was critical for validating synthesis outcomes, and supporting the interpretation of electrochemical and spectroscopic data.

2.6 Electrochemical Techniques

2.6.1 Coin Cell Assembly and Measurement

In this thesis, cathode electrodes were fabricated as free-standing films composed of the active cathode material, acetylene black (Alfa Aesar, 99.9+%) as the electronic conductor, and polytetrafluoroethylene (PTFE, ICI G1) as the binder. The specific component ratios were adjusted according to experimental requirements. Initially, the active material was thoroughly mixed with acetylene black, followed by the incorporation of the PTFE binder to form a cohesive, self-supporting electrode film. The resulting film was then calendared to a uniform thickness of approximately 0.1 mm, with typical active material loadings in the range of 5–10 mg cm^{-2}.

For cell assembly, lithium or sodium metal disks (MTI Corporation) served as the anodes for Li- and Na-based cells, respectively. The cathode and anode were separated by

two glass microfiber separators (Whatman) soaked in a liquid electrolyte, $LiPF_6$ or $NaPF_6$ dissolved in a carbonate-based solvent. All CR2032 coin cells were assembled in an argon-filled glovebox with O_2 and H_2O levels maintained below 0.5 ppm. The internal configuration of the coin cells and the assembly sequence are schematically illustrated in **Figure 2.8**.

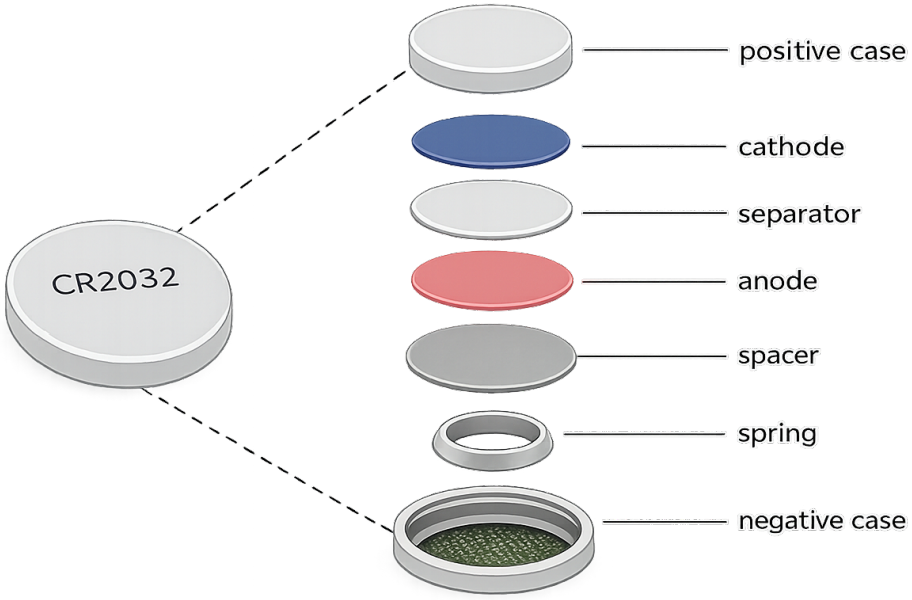

Figure 2.8: Schematic instruction of CR 2032 coin cell assembly.

Cells were galvanostatically cycled on Bio-Logic or Maccor battery cyclers at constant current densities, typically normalized to the active-material mass with a unit mA g^{-1}. Specialized cells for *ex-situ* PXRD and XPDF were prepared using a powder mixture of active material and acetylene black as the cathode without binder. Unless otherwise stated, all electrochemical tests were performed at 30 °C.

2.6.2 Differential Electrochemical Mass Spectroscopy

DEMS monitors gas evolution during electrochemical cycling, providing real-time

analysis of parasitic reactions and oxygen-redox processes. In this technique, gases generated within a sealed electrochemical cell are continuously transferred to a quadrupole mass spectrometer via a capillary line under controlled Ar flow. This setup allows for sensitive detection of species such as O_2, CO_2, and other volatile products.

In this thesis, a custom-modified electrochemical cell from EL-CELL® was utilized. **Figure 2.9** illustrates the external appearance and internal configuration of the cell. The electrode film and lithium metal served as the cathode and anode, respectively, separated by two glass microfiber separators. 1 M $LiPF_6$ in propylene carbonate (PC) was used as the electrolyte. All components were assembled in the sequence shown and sealed using the top compression screw. The entire assembly process was carried out inside an Ar-filled glovebox.

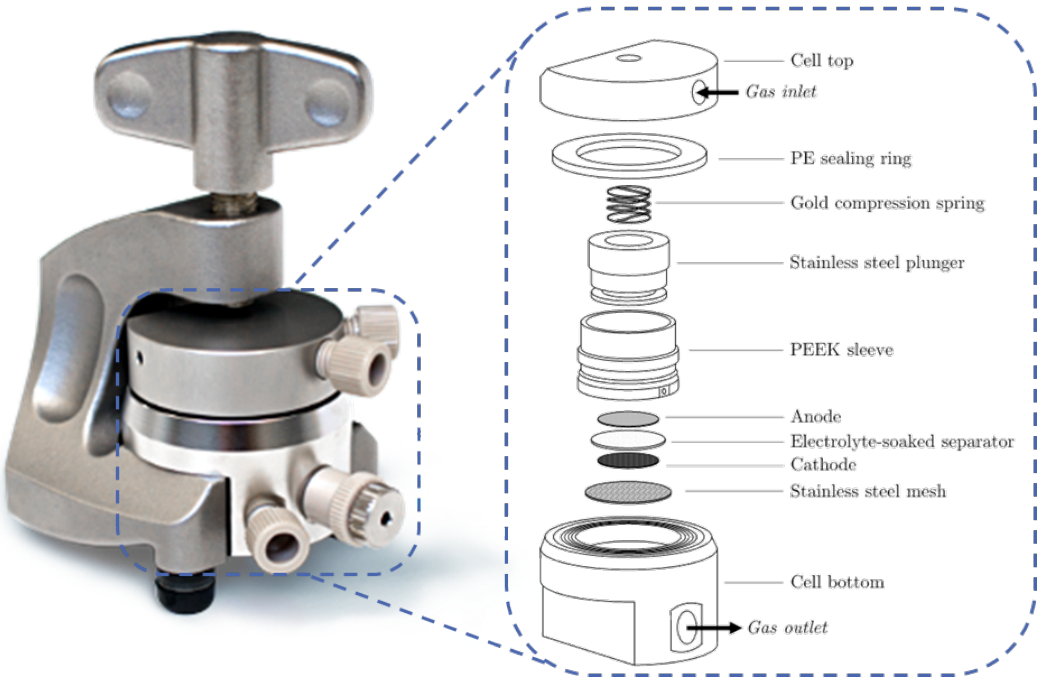

Figure 2.9: Schematic illustration of the construction of the DEMS cell used in this thesis. Figure from EL-CELL®.

The DEMS cell was connected to the mass spectrometer through a capillary inlet. Argon carrier gas was introduced at a constant flow rate to maintain equilibrium between evolved and sampled gases. The ion currents corresponding to different mass-to-charge (m/z) values were recorded and calibrated against reference gases, allowing quantitative evaluation of gas evolution as a function of state of charge.

This operando approach enabled direct correlation between gas evolution events and electrochemical processes. For example, by distinguishing reversible lattice-oxygen redox from irreversible oxygen release, thereby providing critical mechanistic insights into oxygen activity in high-voltage cathode materials.

2.7 References

1. V. Grover, B. P. Mandal and A. K. Tyagi, *Handbook on Synthesis Strategies for Advanced Materials : Volume-I: Techniques and Fundamentals*, Springer Singapore, Singapore, 2021.
2. M. Sopicka-Lizer, *High-energy ball milling: mechanochemical processing of nanopowders*, Elsevier, 2010.
3. C. Delmas, J. J. Braconnier and P. Hagenmuller, *Materials Research Bulletin*, 1982, **17**, 117-123.
4. A. R. Armstrong and P. G. Bruce, *Nature*, 1996, **381**, 499-500.
5. K. S. Tan, M. V. Reddy, G. V. S. Rao and B. V. R. Chowdari, *Journal of Power Sources*, 2005, **147**, 241-248.
6. R. Heimann and A. Hunt, *X-ray powder diffraction (XRPD)*, Oxford University Press, Oxford, UK, 2017.
7. E. H. Kisi and C. J. Howard, *Applications of neutron powder diffraction*, Oxford University Press, 2012.
8. X. Zhou and G. E. Thompson, *Reference Module in Materials Science and Materials Engineering*, Elsevier, 2017.
9. L. A. Bendersky and F. W. Gayle, *Journal of Research of the National Institute of*

Standards and Technology, 2001, **106**, 997-1012.

10. T. Kato, K. Goto, T. Niwa, T. Shimizu, A. Fujii, B. Okumura, H. Oka and H. Kadoura, *Scientific Reports*, 2025, **15**, 5428.

11. S. J. L. Billinge, *Zeitschrift für Kristallographie - Crystalline Materials*, 2004, **219**, 117-121.

12. S. J. Pennycook and P. D. Nellist, *Scanning transmission electron microscopy: imaging and analysis*, Springer Science & Business Media, 2011.

13. J. A. Weil and J. R. Bolton, *Electron paramagnetic resonance: elementary theory and practical applications*, John Wiley & Sons, 2007.

14. C. T. Chantler, G. Bunker, P. D'Angelo and S. Diaz-Moreno, *Nature Reviews Methods Primers*, 2024, **4**, 89.

15. R. House, University of Oxford, 2019.

16. D. Asakura, E. Hosono, Y. Nanba, H. Zhou, J. Okabayashi, C. Ban, P. A. Glans, J. Guo, T. Mizokawa, G. Chen, A. Achkar, D. Hawthron, T. Regier and H. Wadati, *AIP Advances*, 2016, **6**, 035105.

17. A. J. Achkar, T. Z. Regier, H. Wadati, Y. J. Kim, H. Zhang and D. G. Hawthorn, *Physical Review B*, 2011, **83**.

18. B. Ravel and M. Newville, *Synchrotron Radiation*, 2005, **12**, 537-541.

19. F. M. F. de Groot, M. W. Haverkort, H. Elnaggar, A. Juhin, K. J. Zhou and P. Glatzel, *Nature Reviews Methods Primers*, 2024, **4**, 45.

20. R. A. House, J. J. Marie, M. A. Pérez-Osorio, G. J. Rees, E. Boivin and P. G. Bruce, *Nature Energy*, 2021, **6**, 781-789.

21. M. C. C. D. Ignacio, G. W. Curtzwiler, M. R. Early, K. M. Updegraff and K. L. Vorst, *Methods and Protocols*, 2023, **6**, 10.

22. A. I. Vogel and G. H. Jeffery, *Vogel's textbook of quantitative chemical analysis*, Wiley, 1989.

3

Temperature-Dependent Transition Metal Migration in Ribbon-Ordered Na(Li)-Mn-O Cathodes

Contents

3.1 Introduction

TM migration is one of the major degradation pathways in layered oxide cathodes, often leading to structural instability, voltage hysteresis, and poor capacity retention during electrochemical cycling.[1, 2] This issue is especially critical in oxygen-redox-active cathodes for LIBs and SIBs, where the reversibility of the electrochemical process strongly depends on the preservation of the local TM environment and layered framework.[3-5] A deeper understanding of TM migration is therefore essential for clarifying the origin of electrochemical degradation and for developing mitigation strategies in next-generation high-energy cathodes.

Among oxygen-redox cathodes, ribbon-ordered layered manganese oxides provide a particularly useful model platform for investigating TM migration. Compared with other ordering motifs, ribbon superstructures have been shown to better suppress irreversible TM rearrangement and to retain a more reversible high-voltage plateau, making them especially suitable for studying the structural origin and kinetic nature of migration processes.[6, 7] In addition, these materials allow direct comparison between different alkali-layer coordination environments while preserving a closely related TM-layer framework.[6-10]

On this basis, this chapter focuses on $Na_{0.52}Li_{0.2}Mn_{0.8}O_2$ and its Li-exchanged analogue $Li_{0.56}Li_{0.2}Mn_{0.8}O_2$. These two compounds were selected as representative model systems because they share the same ribbon-ordered TM framework but differ fundamentally in the coordination environment of the AM layer: the Na-based phase contains prismatic AM-layer sites, whereas the Li-exchanged phase contains octahedral AM-layer sites. This structural contrast provides an opportunity to isolate how AM-layer

coordination geometry influences Li migration, TM rearrangement, and the resulting structural evolution during cycling.

To quantitatively track these processes, a new electrochemical descriptor, the plateau capacity proportion (P), and its difference between charge and discharge (ΔP), is introduced in this chapter. This descriptor links the evolution of the high-voltage plateau to the degree of TM migration and superstructure loss, thereby bridging electrochemical signatures with local structural changes. By examining the temperature dependence of ΔP and applying Arrhenius analysis, the apparent kinetic barrier associated with TM migration can be evaluated.

Combining electrochemical characterization with *ex-situ* and *operando* XRD and complementary atomistic modelling, this chapter investigates how local coordination geometry governs migration pathways in these two layered systems. In the Na-based material, the initial prismatic AM-layer environment makes Li migration energetically unfavorable and requires slab gliding to generate octahedral sites that can accommodate Li ions during charge. In contrast, the Li-exchanged phase already contains octahedral AM-layer sites, enabling more direct Li migration and facilitating subsequent Mn rearrangement within the TM layer. Through this comparison, the chapter establishes TM migration as a kinetically controlled process and identifies coordination geometry as a key structural factor governing migration behavior in ribbon-ordered oxygen-redox cathodes.

3.2 Experimental Section

3.2.1 Material Synthesis and Composition Analysis

Na-based ribbon-ordered cathode material, $Na_{0.6}Li_{0.2}Mn_{0.8}O_2$, was synthesized via solid-state reaction reported previously. The stoichiometric amounts of precursors Na_2CO_3 (≥99.0%, Aldrich), Li_2CO_3 (≥99.0%, Aldrich) and MnO_2 (≥99.0%, Aldrich) were ball-milled for 12 hrs at 300 rpm using a Retsch PM100, pressed into pellets, and calcined at 800 °C for 12 hrs under oxygen. The heating and cooling rates were 10 °C min^{-1} and 2 °C min^{-1}, respectively.

The Li counterpart $Li_{0.6}Li_{0.2}Mn_{0.8}O_2$ was prepared through an ion-exchange reaction, refluxing $Na_{0.6}Li_{0.2}Mn_{0.8}O_2$ (500 mg) overnight in hexanol containing a large excess of LiBr (5g) at 140 °C. After cooling and vacuum filtration, the remaining solid was washed with ethanol and dried in the vacuum oven at 60 °C.

Both samples were sent to Butterworth Laboratories for ICP-OES analysis via a mail-in service. Sample preparation (powder dissolved in hydrochloric acid) and ICP-OES measurements were carried out by the laboratory, while the author performed the subsequent data analysis. All powder handling prior to submission was conducted in a glovebox to prevent air or moisture exposure.

3.2.2 Electrochemistry

Cathode electrodes were prepared by mixing active material, acetylene black, and PTFE binder in a mass ratio of 8:1:1, with typical active material loadings ranging from 5 to 10 mg cm^{-2}. The mixture was homogenized using a mortar and pestle and subsequently calendared to a uniform thickness of approximately 0.1 mm. Samples designated for *ex-situ* XRD characterization were prepared in powder form, using an active material to acetylene black ratio of 8:2 without binder.

Electrochemical testing was carried out using CR2032 coin cells assembled in an argon-filled glovebox. Na-metal and Li-metal disks (MTI Corporation) were employed as the anodes in the respective Na-based and Li-based coin cells. Both cell types utilized two glass microfiber separators (Whatman). For each Na cell, the electrolyte was 140 μL of 1M $NaPF_6$ in EC: DMC: EMC = 1:1:1 vol% with 5% FEC (DodoChem). For each Li cell, the electrolyte was 140 μL of 1M $LiPF_6$ in EC: EMC = 30:70 vol% electrolyte (DodoChem). Electrochemical charge-discharge measurements were typically performed between 2–4.8 V (for Li cell) and 2–4.5 V (for Na cell) at a current density of 10 mA g^{-1} using a Maccor Series 4000.

3.2.3 Structural Characterization

PXRD was employed to analyze the bulk long-range crystalline structure. In-house XRD was collected using a Rigaku SmartLab diffractometer using Cu $K_{\alpha 1}$ radiation (λ= 1.54051 Å) equipped with a Ge (220) double bounce monochromator. Synchrotron PXRD was measured at the I11 and I15-1 beamlines of Diamond Light Source. The diffraction data were analysed using the FAULTS module within the FullProf software package to resolve the stacking faults in the Li counterpart $Li_{0.6}Li_{0.2}Mn_{0.8}O_2$ sample obtained by ion-exchange.[11, 12]

The superstructure layout within the TM layer of both Na and Li samples was investigated by ADF-STEM and ED. The structure model was created and optimized using VESTA and SingleCrystal®.[13] TEM samples were prepared and data were collected by the collaborator, while the author carried out the subsequent data analysis, including structure model building, with advice from the collaborator.

ADF-STEM imaging was performed using an aberration-corrected JEOL ARM 200F microscope operated at an accelerating voltage of 200 kV. The emission current was 5μA and beam current was 35 pA. A convergence semi-angle of 22 mrad was used, with a collection semi-angle of 69.6–164.8 mrad (ADF). Fast-acquisition and multi-frame image stacks were recorded and subsequently corrected for drift and scan distortions using the SmartAlign software. To prevent exposure to air, samples were transferred to the STEM microscope using a vacuum transfer suitcase.

ED patterns were collected by a high vacuum JEOL 2100 under 200 kV. The sample was transferred to the TEM column using a Gatan vacuum transfer holder, which ensures complete isolation from air and moisture throughout the process.

The local coordination environment of alkaline ions was detected by solid state Nuclear Magnetic Resonance (NMR). ^{7}Li magic angle spinning (MAS, υ_R = 37037 Hz) solid state NMR were completed at 9.45 T ($\upsilon_0{}^{7}$Li = 155.53 MHz, $\upsilon_0{}^{23}$Na = 105.86 MHz) using a Bruker Avance III HD spectrometer and a 1.9 mm double air bearing MAS probe. All ^{7}Li spectra were calibrated using a 1 M LiCl(aq) solution in D_2O as an external reference at 0 ppm. All spectra were recorded using a Hahnecho ($^{\pi}/_{2}$-τ-π-τ) sequence, where τ is $1/\upsilon_R$ and $^{\pi}/_{2}$ is 250 kHz. The resultant free induction decay (FID) signal is processed as a half echo. The ^{7}Li spectra were achieved with a recycle delay of 300 ms. The isotropic resonance was determined by varying the spinning speed between 30-39 kHz to isolate the spinning sidebands.

3.2.4 Morphology

SEM images were captured using a Carl Zeiss Merlin field emission analytical

scanning electron microscope at an operating voltage of 10 keV. Na and Li cathode powders were mounted on a stub using carbon tape.

Unless otherwise stated, the material synthesis, electrochemical testing, and data analysis presented in this chapter were performed by the author. Specific contributions from collaborators are identified in the relevant sections, particularly for advanced characterization measurements and external analytical services. The interpretation and integration of the results were carried out by the author.

3.3 Results and Discussion

3.3.1 Background and Kinetics Study of P2-$Na_{0.6}Li_{0.2}Mn_{0.8}O_2$

Ribbon-ordered $Na_{0.6}Li_{0.2}Mn_{0.8}O_2$ ($P2_1/c$ space group) was prepared via the solid-state method. The ICP result confirmed the composition as $Na_{0.52}Li_{0.2}Mn_{0.8}O_2$. The schematic structural diagram in **Figure 3.1(a)** illustrates the stacking sequence (side view along the [100] direction) and the superstructure arrangement within the TM layers (top view along the [001] direction). Here, [100] and [001] denote viewing directions rather than the crystallographic planes. It is a P2-type layered oxide according to the classification proposed by Delmas *et al*.[14] The superstructure leads to extra diffraction peaks in XRD pattern highlighted by the shaded blue area in **Figure 3.1(b)**. The previous study formulated the evolution of TM layers and loss of superstructure during cycling as illustrated in **Figure 3.1(a)**.[6] During charge shown under the pink title, the Li migrates out of the TM layers, leaving vacancies behind. Mn subsequently migrates within the TM layer, forming vacancy clusters. Oxidized lattice oxygen then dimerizes and transforms to molecular O_2 trapped in

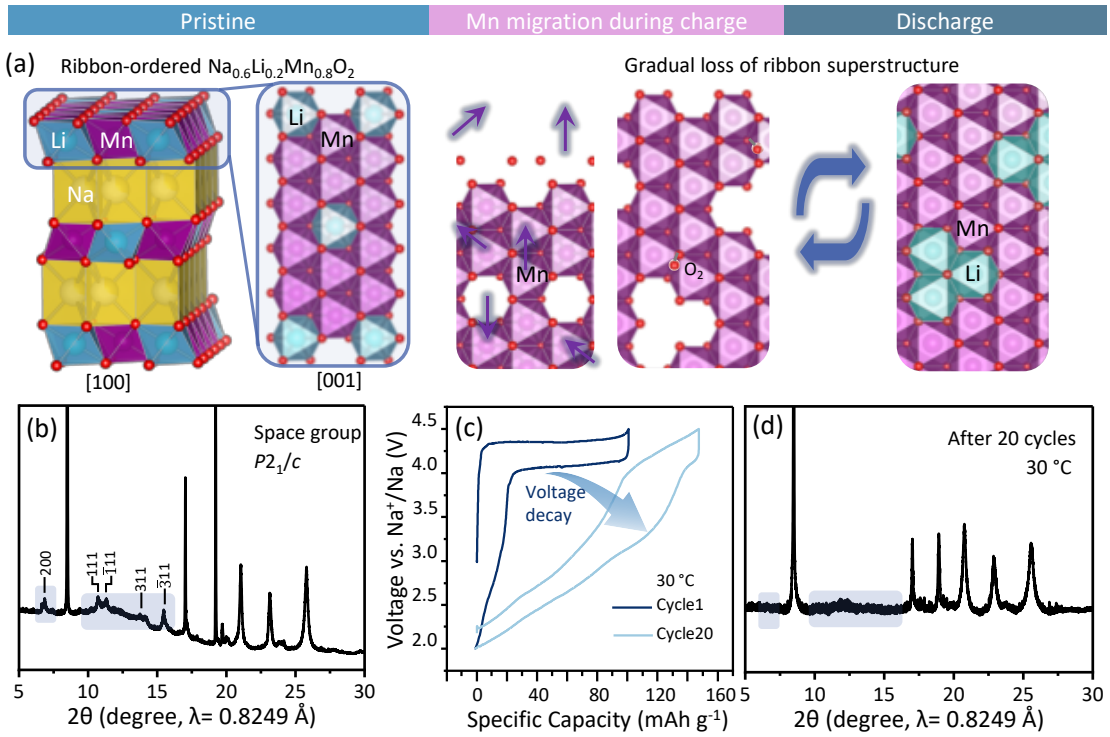

Figure 3.1: (a) Schematic illustration of the crystal structure of ribbon-ordered $Na_{0.6}Li_{0.2}Mn_{0.8}O_2$ along the [100] view and a zoom-in [001] view of the superstructure layout within the TM layers and its evolution during charge and discharge due to Mn migration; (b) Synchrotron XRD pattern of pristine $Na_{0.6}Li_{0.2}Mn_{0.8}O_2$ with superstructure peaks marked; (c) The first and 20th load curve of $Na_{0.6}Li_{0.2}Mn_{0.8}O_2$ at 30 °C; (d) Synchrotron XRD pattern of $Na_{0.6}Li_{0.2}Mn_{0.8}O_2$ after 20 cycles at 30 °C.

the vacancy clusters. During discharge, Li comes back and fills the vacancy clusters rather than the original positions. Meanwhile, molecular O_2 get reduced at relatively low potential and back to the lattice accompanied with voltage hysteresis and loss of discharge plateau.[6] As the cycling continues, the clusters increase along with the loss of oxygen redox plateaus, as shown in **Figure 3.1(c)**. The XRD pattern after 20 cycles under 30 °C in **Figure 3.1(d)** clearly displays the disappearance of superstructure reflections, evidencing the severe migration of Mn in TM layers.

To investigate whether Mn Migration and the subsequent loss of ribbon-ordered superstructure are driven by kinetic factors, electrochemical tests were conducted at

multiple temperatures from -30°C up to 30°C. The first five load curves obtained at 30 °C, 0 °C, and -20 °C are shown in **Figure 3.2(a-c)**. Clearly, cycling at lower temperatures maintains the discharge plateau and reduces voltage decay. Corresponding XRD patterns of $Na_{0.52}Li_{0.2}Mn_{0.8}O_2$ at pristine and after 20 cycles at 30 °C and -20 °C are shown in **Figure 3.2(d-f)**. Notably, the superstructure peaks remain intact after cycling at -20 °C but disappear entirely at 30 °C. This observation establishes a direct relationship between the

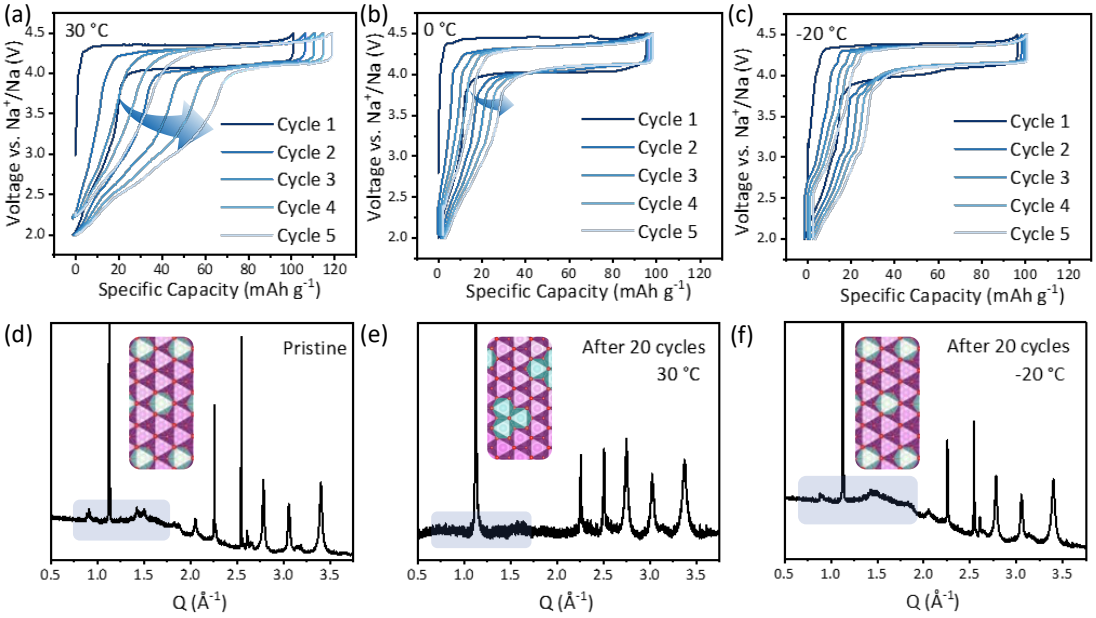

Figure 3.2: (a–c) Voltage profiles of ribbon-ordered $Na_{0.6}Li_{0.2}Mn_{0.8}O_2$ during the first five cycles at (a) 30 °C, (b) 0 °C, and (c) -20 °C. (d-f) Synchrotron XRD patterns of $Na_{0.6}Li_{0.2}Mn_{0.8}O_2$ in the pristine state and after 20 cycles at 30 °C and -20 °C, respectively. The highlighted regions indicate peaks associated with the TM layer superstructure. Cycling at lower temperatures slows the kinetics of Mn migration, thereby preserving both the superstructure and the high-voltage plateau.

preservation of the ribbon superstructure and the maintenance of the high-voltage plateau, demonstrating that reduced Mn migration kinetics at lower temperatures significantly contribute to the maintenance of superstructure.

Based on the temperature-dependent electrochemical behavior **(Figure 3.2(a–c))** and

the corresponding evolution of superstructure peaks in XRD (**Figure 3.2(d–f)**), a direct relationship between kinetics, structural stability, and electrochemical performance is established. To quantify this relationship, the first-cycle load curves of $Na_{0.52}Li_{0.2}Mn_{0.8}O_2$ were collected over a temperature range from -30 to 30 °C. The proportion of plateau capacity relative to the total capacity during charge/discharge serves as an effective descriptor to present the contribution of reversible oxygen redox (oxygen coordinated to two Mn atoms rather than molecular O_2 within vacancy clusters), avoiding the interference from the capacity variations due to different temperatures and cells. As illustrated in **Figure 3.3 (a–b)**, the plateau capacity proportion P_{ch}/P_{dis} is defined as the ratio of charge/discharge plateau capacity to the total charge/discharge capacity, respectively. To quantify the plateau capacity, the derivative of the voltage–capacity curve was analyzed to identify characteristic turning points separating the sloping and plateau regions. During charge, the onset of the high-voltage plateau was defined by the turning point, and the plateau capacity was calculated from this point to the end of charge. During discharge, the plateau was observed at the beginning of the curve and its end was defined by the corresponding turning point. The plateau capacity was therefore obtained from the start of discharge to this boundary. In both cases, the plateau capacity was normalized by the total charge or discharge capacity to obtain P_{ch} and P_{dis}, respectively. The difference in plateau proportions, $\Delta P = P_{ch} - P_{dis}$, serves as a quantitative descriptor of TM migration and the associated loss of ribbon superstructure, thereby linking electrochemical behavior with structural evolution. As shown in **Figure 3.4,** while P_{ch} remains relatively stable across temperatures, P_{dis} decreases markedly at elevated temperatures, leading to an increase in ΔP. This trend

directly indicates enhanced irreversibility during discharge, consistent with increased Mn migration at higher temperatures.

The temperature dependence of ΔP follows an Arrhenius relationship. As shown in **Figure 3.3(c)**, the linear fit of ln(ΔP) versus 1000/T yields an activation energy (E_a) of 102 meV, confirming that Mn migration is a kinetically controlled process. Complementary experiments involving prolonged resting of samples at TOC revealed no significant changes in electrochemistry or structure, ruling out a thermodynamic driving force for the observed structural evolution.

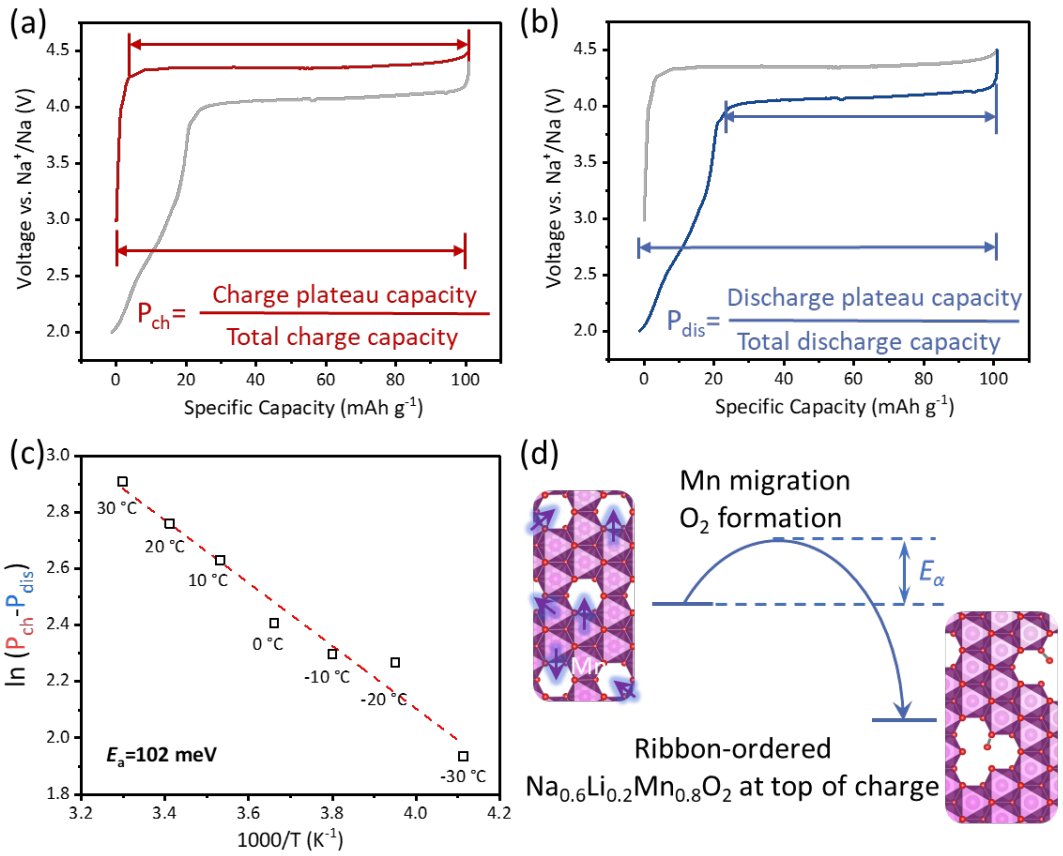

Figure 3.3: (a–b) Schematic definition of charge (P_{ch}) and discharge (P_{dis}) plateau proportions, calculated as the ratio of plateau capacity to total capacity during charge and discharge, respectively. The difference in plateau proportion, $\Delta P = P_{ch} - P_{dis}$, serves as an indicator of TM migration and the associated loss of superstructure. (c) Arrhenius plot of ln(ΔP) versus 1000/T for $Na_{0.6}Li_{0.2}Mn_{0.8}O_2$

during the first cycle at various temperatures. The linear fit indicates that TM migration follows an Arrhenius law, with an activation energy (E_a) of 102 meV. (d) Schematic illustration of the Mn migration at TOC, enabled by Li migration into the AM layer and the subsequent formation of vacancies. The progressive Mn migration leads to the fading of the ribbon-ordered superstructure.

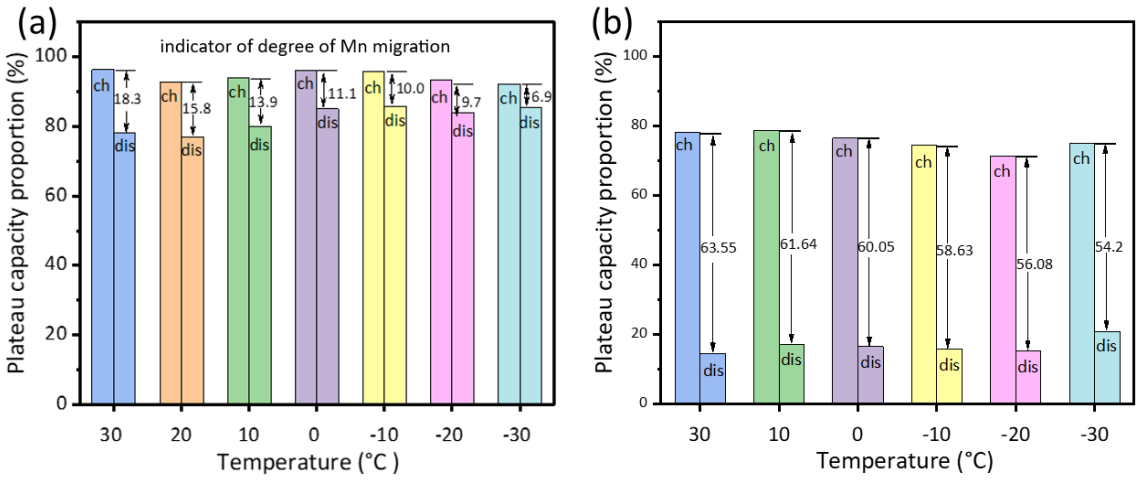

Figure 3.4: Plateau capacity proportion P during charge/discharge under different temperatures extracted from the first load curves of (a)$Na_{0.52}Li_{0.2}Mn_{0.8}O_2$ and (b) $Li_{0.56}Li_{0.2}Mn_{0.8}O_2$.

3.3.2 Structure Solution and Kinetics Study of O6-$Li_{0.56}Li_{0.2}Mn_{0.8}O_2$

The Arrhenius law observed in the Na-based system motivates further exploration of its applicability to other related layered oxide systems.. The Li-exchanged analogue is an ideal candidate for comparative analysis. To preserve the ribbon-type superstructure within the TM layers, the Li-exchanged material was synthesized via ion exchange at a relatively low temperature (140 °C), as detailed previously in Section 3.2.1.

The synchrotron XRD patterns of $Na_{0.52}Li_{0.2}Mn_{0.8}O_2$ and its Li-exchanged analogue are compared in **Figure 3.5(a-b)**, showing an evident shift of the (002) reflection for the latter toward higher diffraction angles, compared with the Na parent sample, indicating a reduction in interlayer spacing since Li^+ is smaller than Na^+. The broadening and asymmetry of diffraction peaks at higher angles are ascribed to stacking faults, commonly

encountered in layered materials derived from the Na-based P2 phase after ion exchange.[15-17] Structural refinement and detailed discussion of these stacking faults are discussed later.

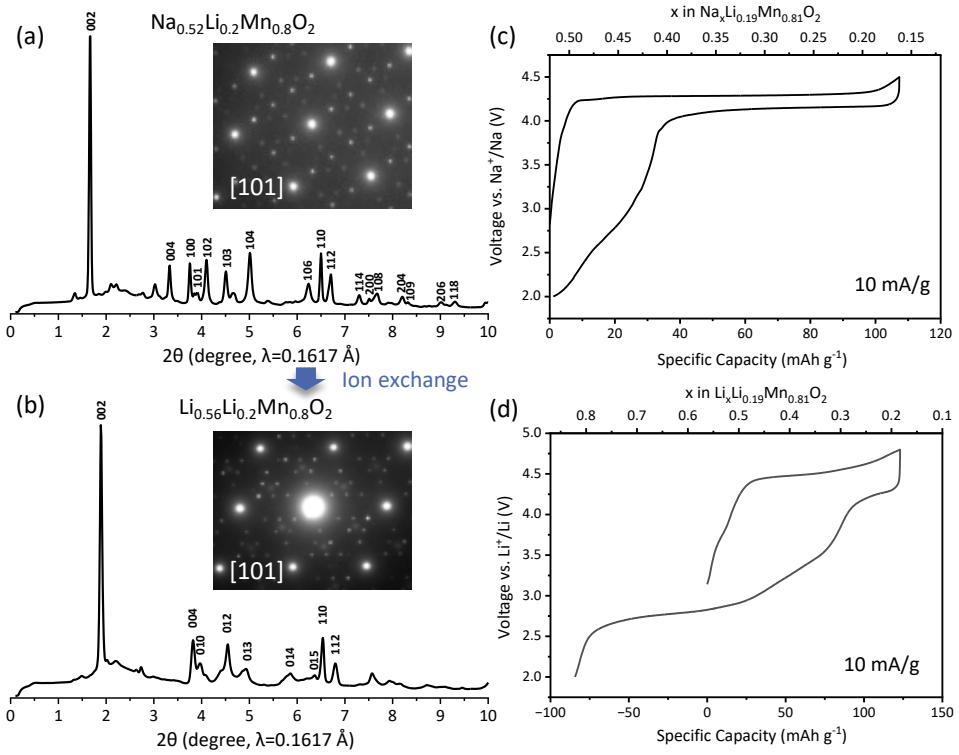

Figure 3.5: (a-b) Synchrotron PXRD patterns with corresponding selected area electron diffraction (SAED) patterns viewed along the [101] zone axis for ribbon-ordered $Na_{0.52}Li_{0.2}Mn_{0.8}O_2$ and its Li-exchanged analogue $Li_{0.56}Li_{0.2}Mn_{0.8}O_2$, respectively; (c–d) First galvanostatic charge-discharge curves at a current density of 10 mA g^{-1} for $Na_{0.52}Li_{0.2}Mn_{0.8}O_2$ and $Li_{0.56}Li_{0.2}Mn_{0.8}O_2$, respectively.

SEM images of both the Na-based and Li-exchanged samples (presented in **Figure S3.1**) confirmed comparable particle sizes, generally within a few micrometers. ICP analysis determined a cation ratio of Li:Mn = 0.76:0.8, consistent with the target composition. The ED patterns viewed along the [101] zone axis for both samples, depicted in **Figure 3.5(a–b)**, exhibited remarkably similar features, affirming the successful retention of ribbon-type ordering within the TM layers upon ion exchange. Additionally, solid-state NMR analysis of the pristine Li sample, displayed in **Figure S3.2(b)**, further

validated the presence of Li ions occupying TM-layer sites. Consequently, the chemical formula of the Li-exchanged compound can be represented as $Li_{0.56}Li_{0.2}Mn_{0.8}O_2$.

The galvanostatic charge-discharge profile for $Li_{0.56}Li_{0.2}Mn_{0.8}O_2$ at a current density of 10 mA g^{-1} (**Figure 3.5(d)**) was characterized by an extended charge plateau corresponding to approximately 0.3 Li extraction per unit formula, followed by a noticeably shorter discharge plateau compared with Na. The overall discharge capacity measured within the voltage window of 2.0–4.8 V reached approximately 200 mAh g^{-1}.

To elucidate the crystal structure of $Li_{0.56}Li_{0.2}Mn_{0.8}O_2$, structural determination was divided into two critical steps: interlayer and intralayer ordering. First, the c-axis stacking sequence of TM and AM layers was identified, and second, the superstructure ordering within TM layers and their relative displacements were carefully considered.

The ion-exchange transformation from Na-based compounds to Li-based analogues has been widely studied.[15, 18-23] Typically, achieving an ideal P2-to-O2 structural conversion is challenging due to the inherent freedom of TM-layer gliding. Two equivalent glide vectors, (1/3, 2/3, z) and (2/3, 1/3, z), are possible to form suitable octahedral sites for Li ions, as illustrated in **Figure 3.6**.[15, 17, 18] This structural ambiguity often leads to stacking faults, since TM layers may alternate their gliding directions unpredictably, governed by the competing kinetics between the initiation of ion-exchange reaction centers and the growth of stable O2 domains.[15, 17]

As depicted in **Figure 3.7**, several potential structural variants derived from the P2 exchange, such as the O2, O2', and O6 phases, are illustrated along with their oxygen layer stacking sequences.[14] The alkali ions are accommodated at the octahedral (O) sites between

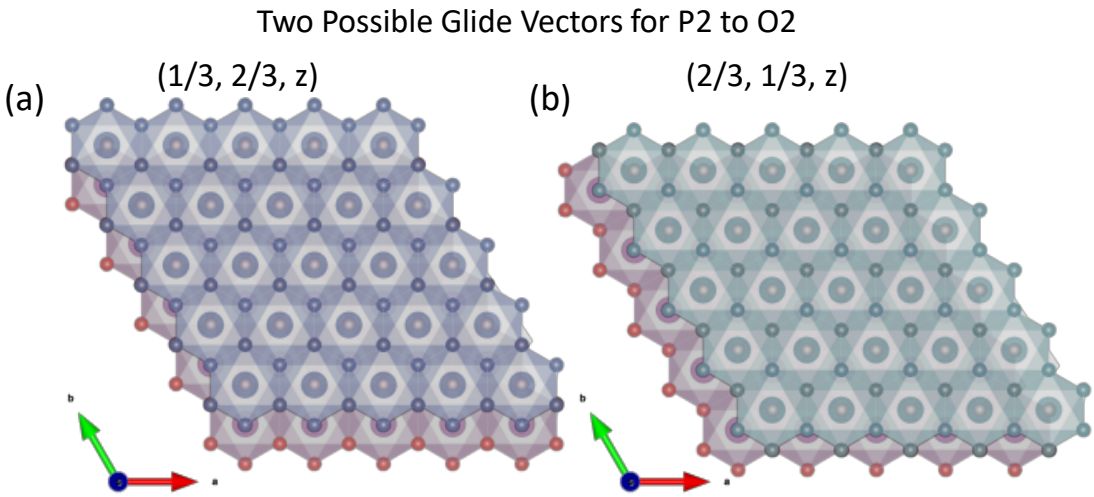

Figure 3.6: Schematic illustration of the two possible glide vectors to transform the P2 structure into the O2-type stacking structure.

TMO_2 layers. Notably, the O6 phase represents a 50/50 intergrowth of O2 phase and its vertically inverted counterpart, O2'. In the case of the $Li_{0.56}Li_{0.2}Mn_{0.8}O_2$ compound studied herein, significant peak broadening observed at higher diffraction angles (**Figure 3.8**)

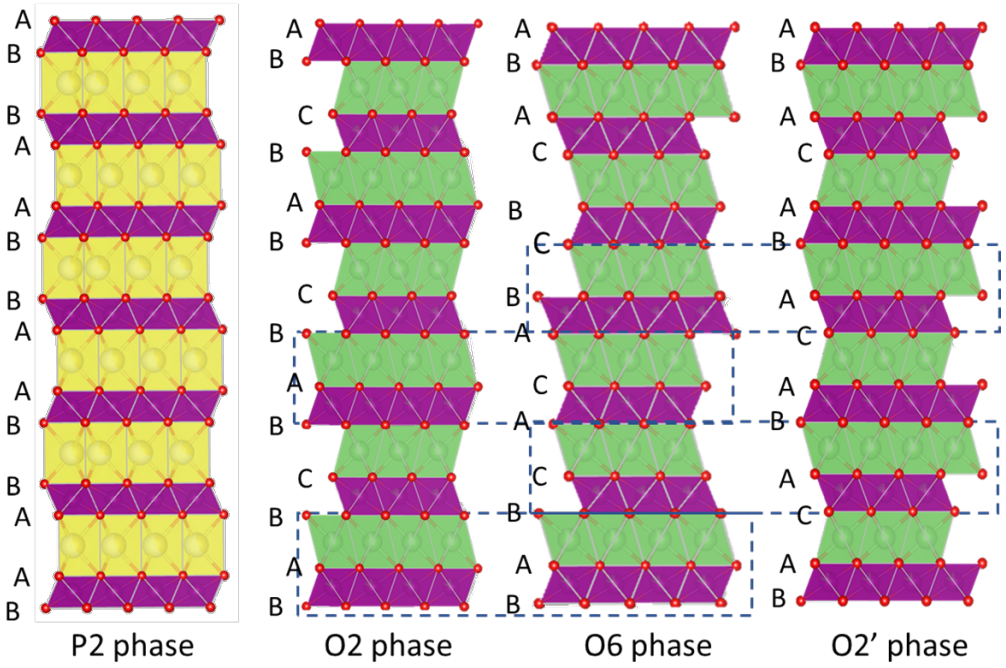

Figure 3.7: Schematic illustration of the crystal structure of P2-type phase, and of O2, O2', O6 phases that are potentially derived from the P2-type phase by Na/Li ion exchange.

aligns well with structural models involving O2&O6-type stacking faults.

XRD pattern simulations of mixtures between O2 and O6 phase, as shown in **Figure 3.8(a)**, were conducted using the FAULTS module within the FullProf suite,[11] explicitly accounting for stacking faults resulting from intergrowth between these two phases. Essential atomic coordinates utilized for the stacking fault modeling are summarized in **Table S3.1**, and representative schematics of possible layer transitions between O2 and O6 stacking are illustrated in **Figure S3.3**.

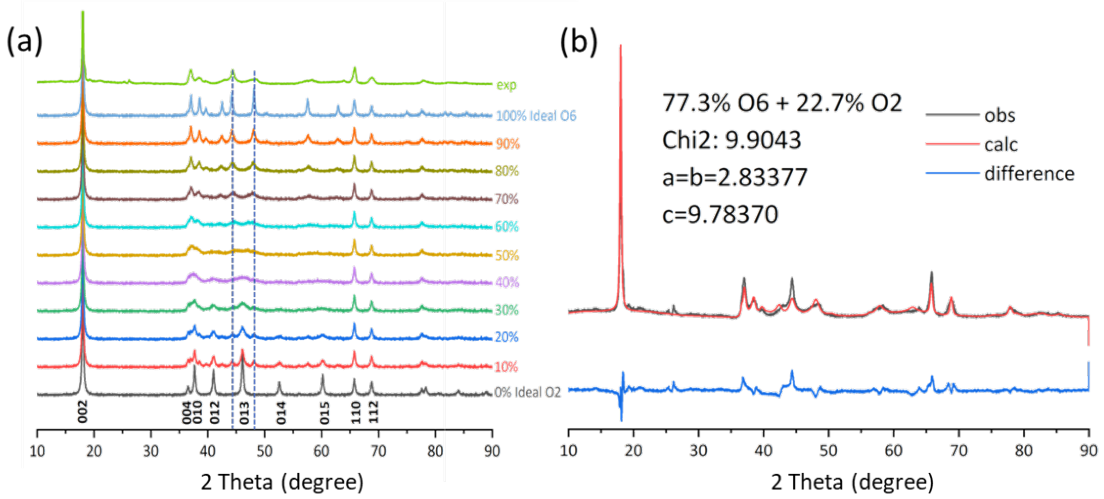

Figure 3.8: (a) Simulations of XRD patterns (Cu *Kα* source) illustrating progressive phase mixtures between O2 and O6 structures, compared with the experimentally measured XRD pattern of $Li_{0.56}Li_{0.2}Mn_{0.8}O_2$ (top pattern in green); (b) Corresponding structural refinement of $Li_{0.56}Li_{0.2}Mn_{0.8}O_2$ performed using the FAULTS module within the FullProf software package. Note that the refinement excludes consideration of the superstructure ordering (located at 20–30 degrees in XRD pattern) within the transition-metal layers.

Based on this systematic stacking-layer modelling approach, a successful refinement of the experimental XRD pattern of the Li sample was achieved, revealing that the $Li_{0.56}Li_{0.2}Mn_{0.8}O_2$ structure comprises approximately 77.3% O6-type stacking and 22.7% O2-type stacking (**Figure 3.8(b)**). Detailed refinement parameters are presented in **Table**

S3.2. It is noteworthy that this refinement did not explicitly incorporate the superstructure peaks around 26° due to the countless possibilities of relative displacements of ribbon ordering.

To accurately resolve the relative displacement of the ordered TM layers, the ADF-STEM image was acquired along the specific [$\bar{1}\bar{1}0$] zone axis, clearly distinguishing Li and Mn atomic columns, as shown in **Figure 3.9(a)**. The STEM image reveals periodic stacking displacements, wherein groups of six layers exhibit a consistent two-column lateral shift between successive layers, separated by regions containing two perfectly aligned TM layers. Images collected along additional zone axes are provided in **Figure 3.10**. The atomic structure determined from these observations is illustrated in **Figure 3.9(b–d)** from different zone axes. The yellow line in **Figure 3.9(b)** specifically highlights the Li positions, which correspond to the darker contrast points in the STEM image.

From the [001] zone axis shown in **Figure 3.9(d)**, Li positions are systematically displaced along the [110] direction by two atomic columns between adjacent layers. Given the Li: Mn ratio of 1:4 within the TM layers, the structure adopts a 5×5 supercell configuration, requiring five consecutive lateral shifts of Li sites to revert to an analogous cation arrangement as initially observed in layer 1. However, despite identical cation positions, layers 1 and 6 differ in their oxygen coordination environments, as visualized from the schematic stacking pattern along the [100] zone axis in **Figure 3.9(c)**. This subtle but significant difference necessitates a minimum unit cell comprising six distinct layers to achieve complete crystallographic periodicity. Consequently, the repeating structural units align layers 1 and 6 when viewed along the [$\bar{1}\bar{1}0$] zone axis (**Figure 3.9(b)**). Interestingly,

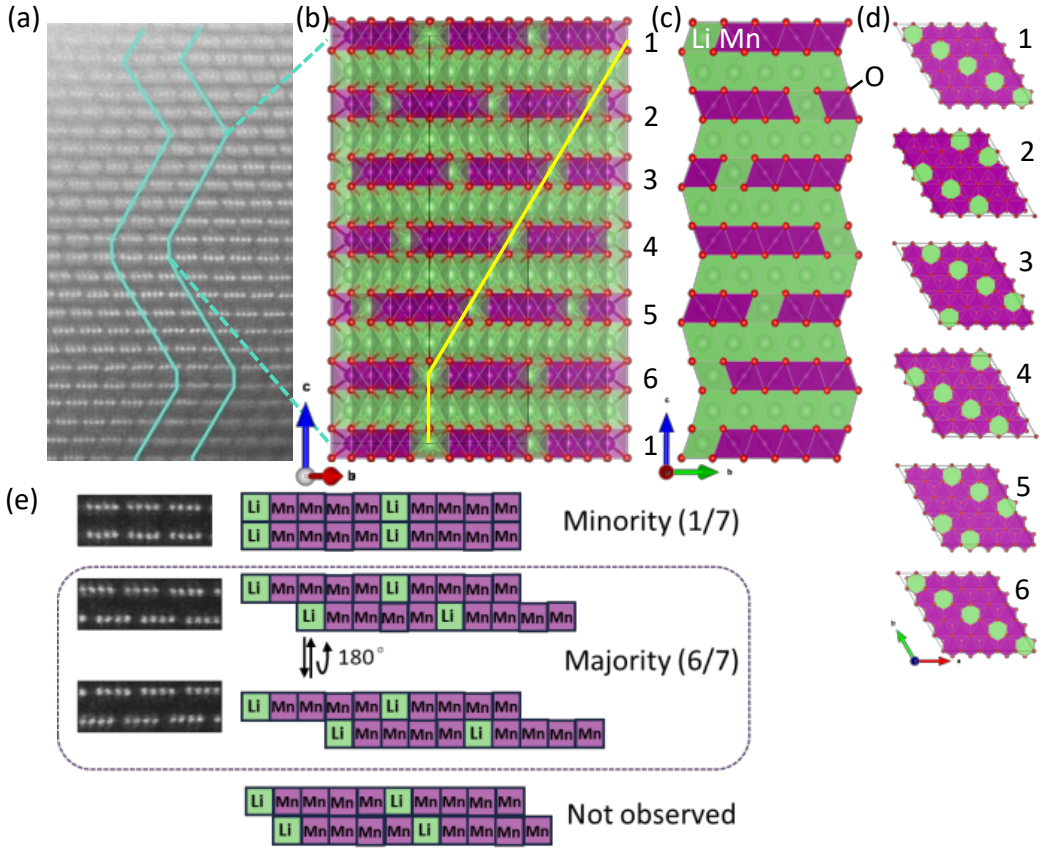

Figure 3.9: (a) ADF-STEM image of $Li_{0.56}Li_{0.2}Mn_{0.8}O_2$ taken along the [$\bar{1}$10] zone axis, highlighting the periodic lateral stacking displacement of the ribbon-type superstructure; (b–c) Corresponding atomic models illustrating the resolved crystal structure viewed along (b) the [$\bar{1}$10] and (c) [100] zone axis. The yellow line in (b) identifies Li positions correlating with the dark contrast in the STEM image; (d) Individual atomic layer configurations viewed along the [001] zone axis, emphasizing the systematic two-column lateral displacement of Li sites within successive TM layers; (e) Schematic summary depicting the observed stacking patterns and relative positions of neighboring TM layers, showing the dominant six-layer repeating blocks with occasional vertical inversions, and noting that aligned stacking configurations occur in approximately one-seventh of the total observed structures.

periodic blocks composed of six-layer units occasionally appear vertically inverted, stacking from layer 6 up to layer 1. **Figure 3.9(e)** summarizes the observed relative stacking configurations of neighboring TM layers. The overall structure predominantly consists of these six-layer blocks, occasionally inverted, along with a minority of perfectly aligned

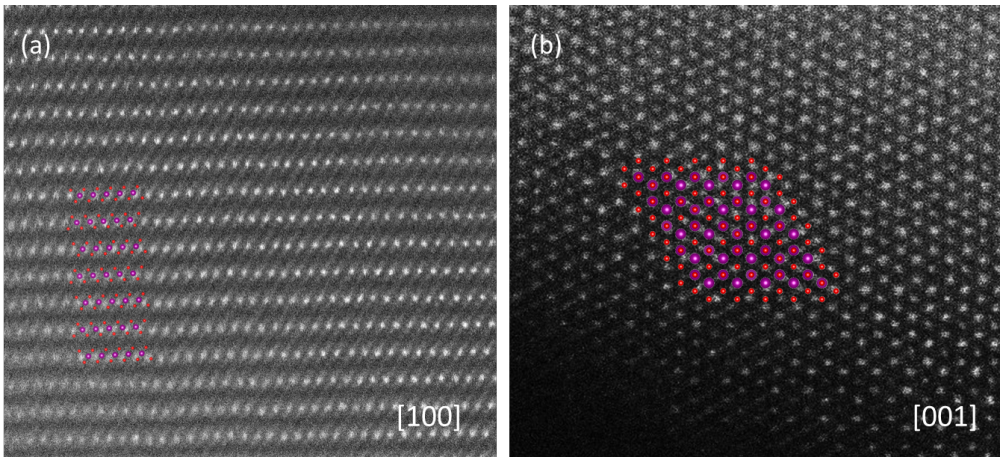

Figure 3.10: ADF-STEM image along (a) [100] and (b) [001] zone axis of $Li_{0.56}Li_{0.2}Mn_{0.8}O_2$. TM and O are in purple and red, respectively.

configurations, accounting for approximately one-seventh of the observed structures. Furthermore, the simulated ED pattern along the [101] zone axis, derived from the constructed structural model, shows good qualitative agreement in terms of reflection positions and symmetry with the experimentally obtained ED pattern (**Figure 3.11),** with

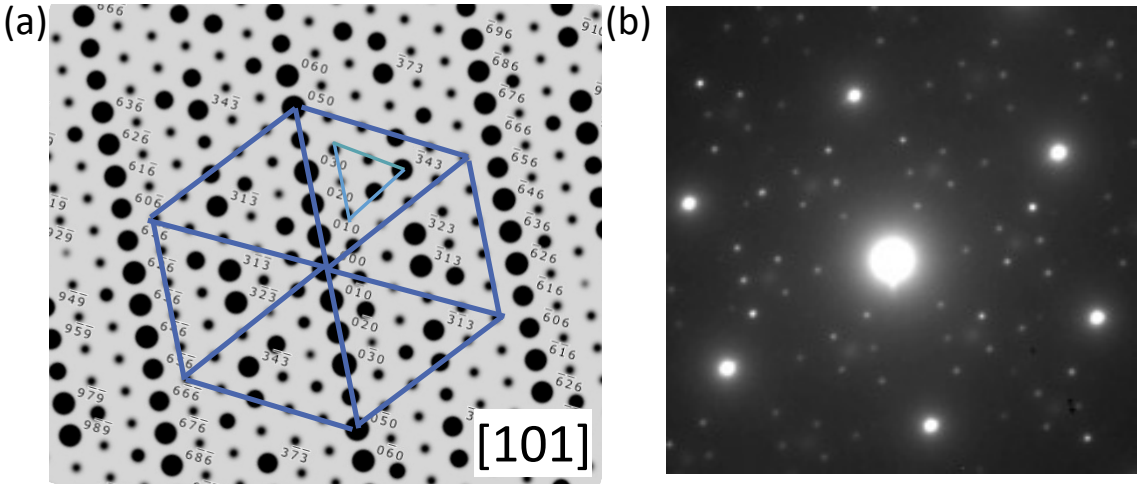

Figure 3.11: (a) Simulated ED pattern along the [101] zone axis based on the created crystal structure of $Li_{0.56}Li_{0.2}Mn_{0.8}O_2$; (b) Experimental ED pattern of $Li_{0.56}Li_{0.2}Mn_{0.8}O_2$.

minor intensity differences likely arising from dynamical scattering effects, thereby supporting the proposed structural model**.** Both patterns distinctly exhibit a characteristic smaller triangular motif nested within a larger triangle, forming part of a hexagonal

diffraction pattern. The inner triangle-shaped scattering derived from the superstructure lateral displacement between adjacent TM layers.

Following the structural elucidation of $Li_{0.56}Li_{0.2}Mn_{0.8}O_2$, a subsequent investigation was conducted to evaluate Mn migration mechanism in this Li-exchanged analogue, as presented in **Figure 3.12**. The same electrochemical descriptor ΔP used previously for the kinetic study of $Na_{0.52}Li_{0.2}Mn_{0.8}O_2$, was employed to quantify Mn migration-related structural degradation. ΔP represents the difference between charge and discharge plateau proportions.

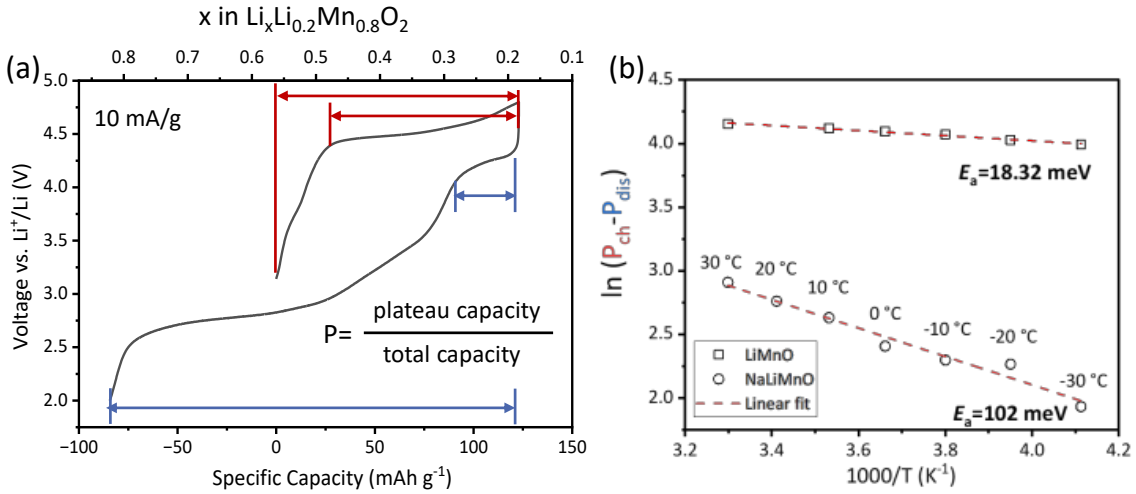

Figure 3.12: (a) Definition of charge (P_{ch}) and discharge (P_{dis}) plateau proportions for $Li_{0.56}Li_{0.2}Mn_{0.8}O_2$, calculated as the ratio of the plateau capacity to the total capacity during the charge and discharge process respectively; (b) Arrhenius plot depicting ln(ΔP) versus 1000/T for $Li_{0.56}Li_{0.2}Mn_{0.8}O_2$ cycled across various temperatures compared with the Na counterpart. The linear fitting using an Arrhenius equation gives a Mn migration activation energy (E_a) of 18.32 meV for $Li_{0.56}Li_{0.2}Mn_{0.8}O_2$.

The data follow the Arrhenius law, indicating thermally activated migration behavior consistent with prior observations in the analogue Na-based system. Notably, the calculated activation energy for Mn migration in $Li_{0.56}Li_{0.2}Mn_{0.8}O_2$ was significantly lower, measured

at 18.32 meV, substantially reduced compared to the Na-based counterpart. This suggests that Mn migration occurs more readily in the Li system, prompting further exploration into the underlying structural factors that facilitate the Mn transport. Potential origins may include differences in oxygen coordination environments and layer spacing. A detailed structural comparison is presented in the following sections.

3.3.3 Structural factors contributing to the mobility of TM-layer ions

The distinct TM migration activation energy observed between $Na_{0.52}Li_{0.2}Mn_{0.8}O_2$ and its Li-exchanged counterpart $Li_{0.56}Li_{0.2}Mn_{0.8}O_2$ could be rationalized through their structural evolution and cation accommodation geometry. To verify this hypothesis, a multi-faceted investigation involving *ex-situ*/*operando* XRD, thermal-assisted phase refinement and atomistic modelling was carried out to reveal critical differences in how these layered oxides respond to alkali-ion extraction and subsequent structural rearrangement.

To elucidate the evolution of stacking pattern upon Na^+ extraction, *ex-situ* XRD patterns of $Na_{0.52}Li_{0.2}Mn_{0.8}O_2$ were collected at various SOCs (**Figure 3.13(a)**). Particular attention was paid to the (002) reflection as it directly reflects changes in layer spacing and stacking order along the c-axis. As shown in **Figure 3.13(b)** (top), the (002) peak shifts systematically to higher angles and broadens during charging, indicating decreased interlayer spacing and the disruption of long-range stacking order.

To provide a quantitative interpretation of this evolution, simulated profiles of the (002) reflection were generated with models containing an increasing amount of O2-layer intergrowth randomly distributed within the main P2-type layers (**Figure 3.13(b)**, bottom).

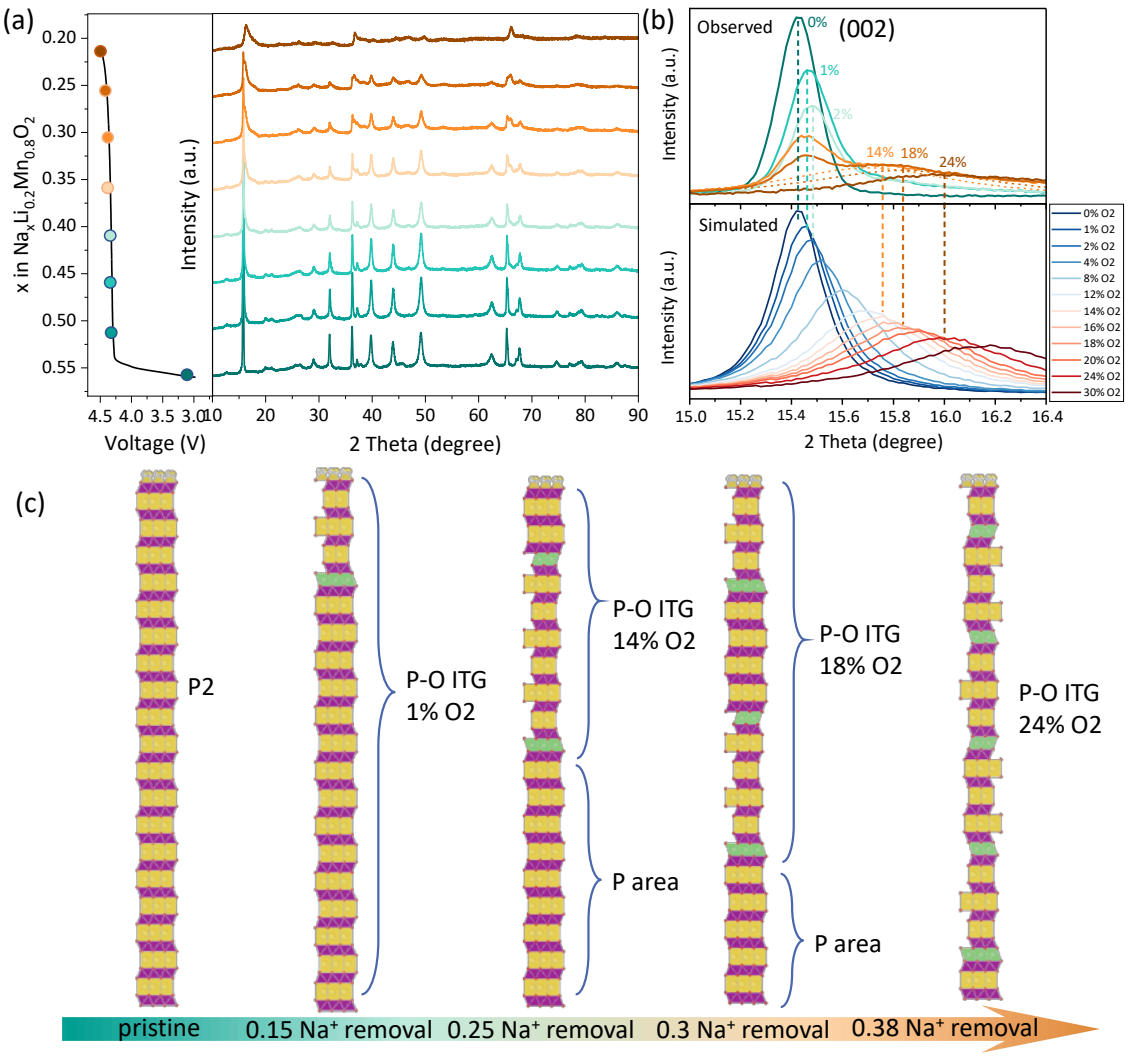

Figure 3.13: (a) *Ex-situ* XRD patterns of $Na_{0.52}Li_{0.2}Mn_{0.8}O_2$ collected at various SOCs during galvanostatic charging at a current density of 10 mA g^{-1}. (b) Top: Enlarged view of the (002) reflection highlighting the progressive peak shift and broadening associated with reduced interlayer spacing and the emergence of O-type stacking faults within the P2-type stacking upon Na extraction. Dashed lines present deconvoluted peak components corresponding to P-O intergrowth (ITG). Bottom: Simulated profiles of the (002) reflection for structures with varying proportions of random intergrowth of P2 and O2-type layers, matching with the experimental observations. (c) Schematic depiction of the structural evolution pathway during charging, illustrating the increasing fraction of O2-type layers domain in $Na_{0.52}Li_{0.2}Mn_{0.8}O_2$ as a function of the extent of Na^+ extraction.

The simulation was performed using the FAULTS module in the FullProf package. The detailed parameters and models employed for these simulations are listed in **Tables S3.3**

and **Table S3.4**. The simulated profiles closely match the experimental peak evolution, indicating a progressive increase in O2-type stacking faults as charging proceeds, reaching approximately 24% O2 at the top of charge.

The schematic illustration in **Figure 3.13(c)** summarizes this structural evolution in details. Initially, the pristine structure exhibited a well-ordered P2 stacking pattern. O2 stacking faults first emerged and grew to approximately 2% following the extraction of 0.15 Na^+ per formula unit (approximately 45 mAh g^{-1}). Upon further Na removal, the (002) reflection went through peak splitting, consisting of a lower-angle component of nearly pristine P2-type domains (with minimal O2-type layers) and a higher-angle component indicative of P-O intergrowth domains with greater O2-type layer content. This peak splitting arose from the random nucleation of layer gliding, which initially generated a heterogeneous distribution of O2-rich and O2-poor domains. As charging processed, the proportion of O2 domains increased continuously, alongside a decrease in regions dominated by P2-type layers. This process also led to an expansion of the P–O intergrowth structure, where the O2 content increased from 14% at a removal of 0.25 Na^+ per formula unit to 24% at TOC.

To further substantiate these structural observations, an additional heat treatment was applied to the fully charged sample to enhance the crystallinity of both P and O-type layer domains and enable more accurate dual-phase refinement. **Figure 3.14(a)** presents XRD patterns collected from $Na_{0.52}Li_{0.2}Mn_{0.8}O_2$ at the top-of-charge state (cycled at 30 °C) before and after heating at 100 °C for 4 hours. The increased intensity of Bragg reflections after heating indicates that the thermal treatment effectively relieved local lattice strain and

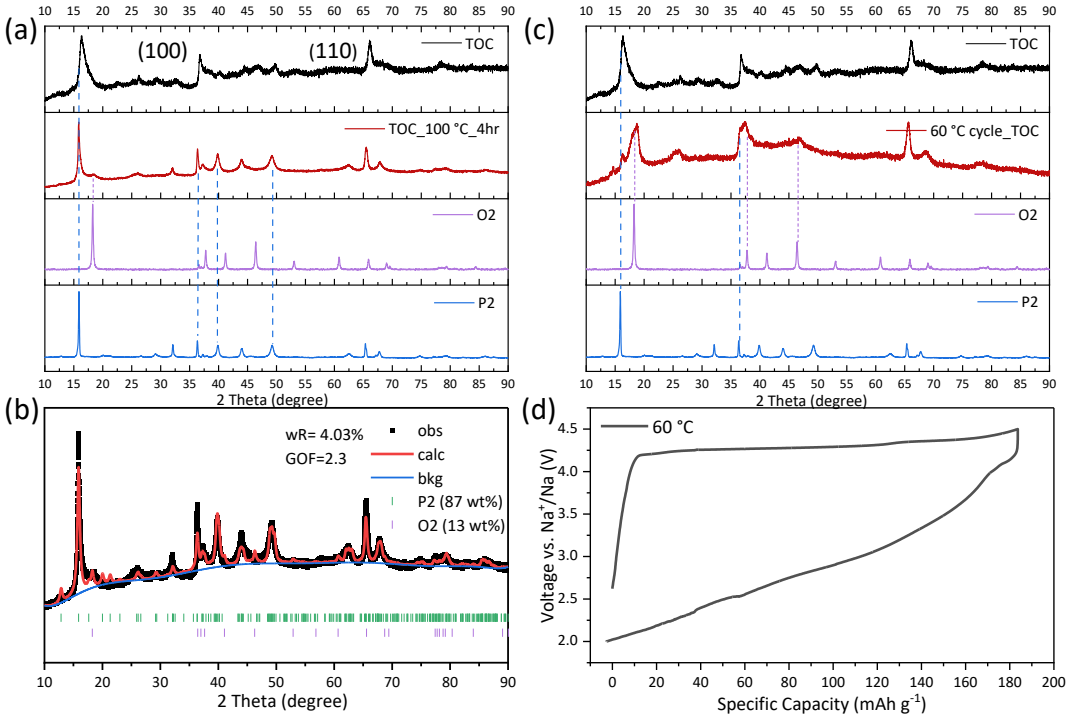

Figure 3.14: (a) XRD patterns of $Na_{0.52}Li_{0.2}Mn_{0.8}O_2$ at TOC (cycling at 30 °C) before and after heating at 100 °C for 4 hrs, shown together with reference patterns of ideal P2 and O2 phases; (b) Two-phase (P2 and O2) Rietveld refinement of the $Na_{0.52}Li_{0.2}Mn_{0.8}O_2$ sample heated at 100 °C for 4 hrs, confirming the growth of O2 phase; (c) XRD patterns comparing $Na_{0.52}Li_{0.2}Mn_{0.8}O_2$ charged to 4.5 V at 30 °C and 60 °C, illustrating the enhanced formation of O2-type stacking at higher temperatures; (d) Galvanostatic charge-discharge profile (10 mA g^{-1}) of $Na_{0.52}Li_{0.2}Mn_{0.8}O_2$ cycled at 60 °C, highlighting the loss of discharge plateau due to severe structural rearrangement associated with increased O2-type stacking faults.

distortions, resulting in a greater phase separation. Dual-phase Rietveld refinement using combined P2 and O2 models (**Figure 3.14(b)**) confirmed a significant proportion (approximately 13%) of O2 phase at the top of charge after heat treatment. The experimentally determined O2 content after thermal relaxation (13%) is lower than the previously simulated value (24%). This discrepancy likely results from the thermal treatment, which promotes lattice relaxation and reduces internal strain, potentially driving the structure toward a more energetically favorable state. The observed reduction in O2

proportion suggests that the P2 phase may be intrinsically more stable than the O2 phase, consistent with the notion that slab gliding required for O2 domain formation needs overcoming an energy barrier.

To explicitly link increased O2-type stacking to electrochemical consequences, comparative XRD analyses of samples charged at ambient (30 °C) and elevated temperatures (60 °C) are provided in **Figure 3.14(c)**. The increase of O2-type domains at elevated temperature is evidenced by intensified characteristic O2 (002) reflection. This structural transition correlates with reduced electrochemical performance, especially the loss of the high-voltage plateau, as demonstrated by the charge-discharge profile measured at 60 °C (**Figure 3.14(d)**). The pronounced reduction in the discharge plateau at elevated temperature underscores the detrimental impact of severe structural rearrangements associated with increased O2 stacking faults. From these experimental observations, it becomes clear that the formation of O-type coordination is the prerequisite for out-of-plane Li migration and subsequent in-plane Mn rearrangement, given that the energy barrier for Li accommodation in prismatic sites in P2-type phase is excessively large.[2, 24, 25]

To further understand the contrasting structural response upon alkali-ion extraction, operando XRD analysis was performed on $Li_{0.56}Li_{0.2}Mn_{0.8}O_2$ during galvanostatic charging (**Figure 3.15(a)**). Unlike the pronounced stacking transitions observed in the Na-based analogue, the operando XRD patterns of $Li_{0.56}Li_{0.2}Mn_{0.8}O_2$ exhibited only minimal shifts and negligible peak broadening, reflecting the structural stability and minimal interlayer rearrangement during Li^+ extraction. The schematic depiction provided in **Figure 3.15(b)** illustrates the mechanism explicitly: upon charging, Li ions originally occupying TM-layer

sites migrate into accessible octahedral AM-layer sites, leaving vacancies behind (highlighted in blue).

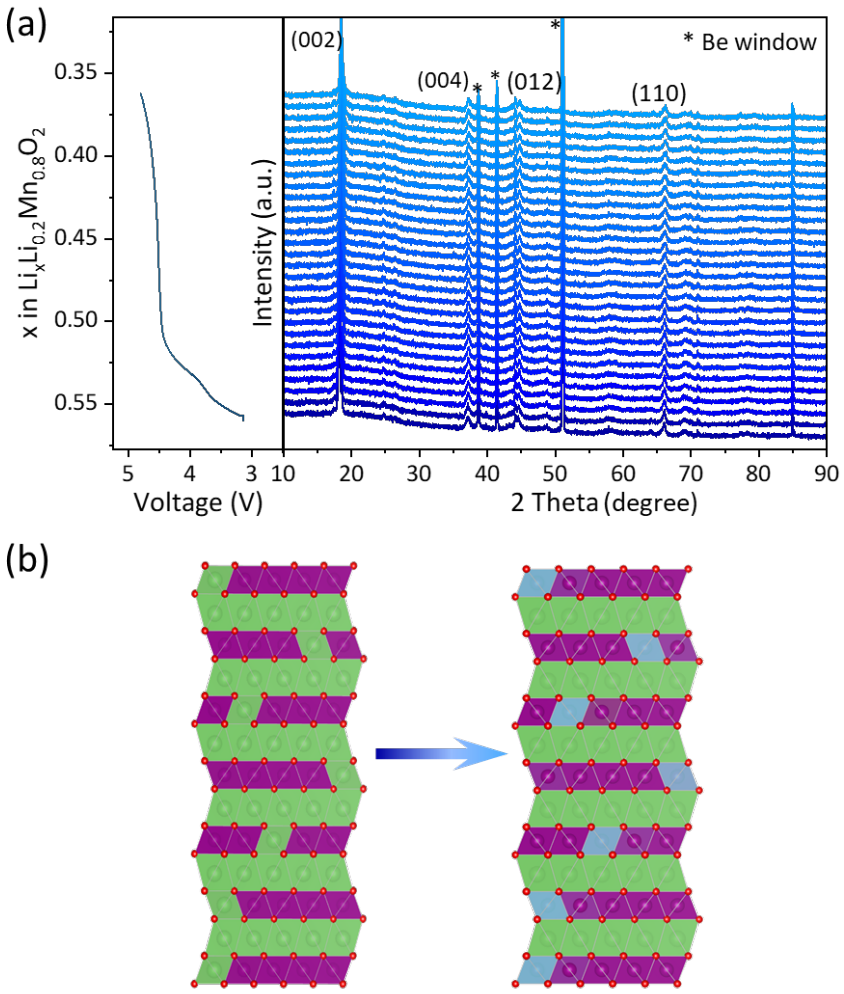

Figure 3.15: (a) *Operando* XRD pattern of $Li_{0.56}Li_{0.2}Mn_{0.8}O_2$ during charge with a current density of 10 mA g^{-1}; (b) Schematic illustration of structural evolution of $Li_{0.56}Li_{0.2}Mn_{0.8}O_2$ upon charge where the Li in TM layers migrates to AM layers, leaving vacancies highlighted with blue.

The structural evolution analysis in this section explains the significantly lower Mn migration activation energy and the enhanced mobility of TM ions observed in $Li_{0.56}Li_{0.2}Mn_{0.8}O_2$ compared to its Na counterpart, as evidenced by the previously discussed Arrhenius analysis (**Figure 3.12**). **Figure 3.16** schematically compares the enlarged coordination environment and Li migration pathways in Na-based and Li-based layered

oxides.

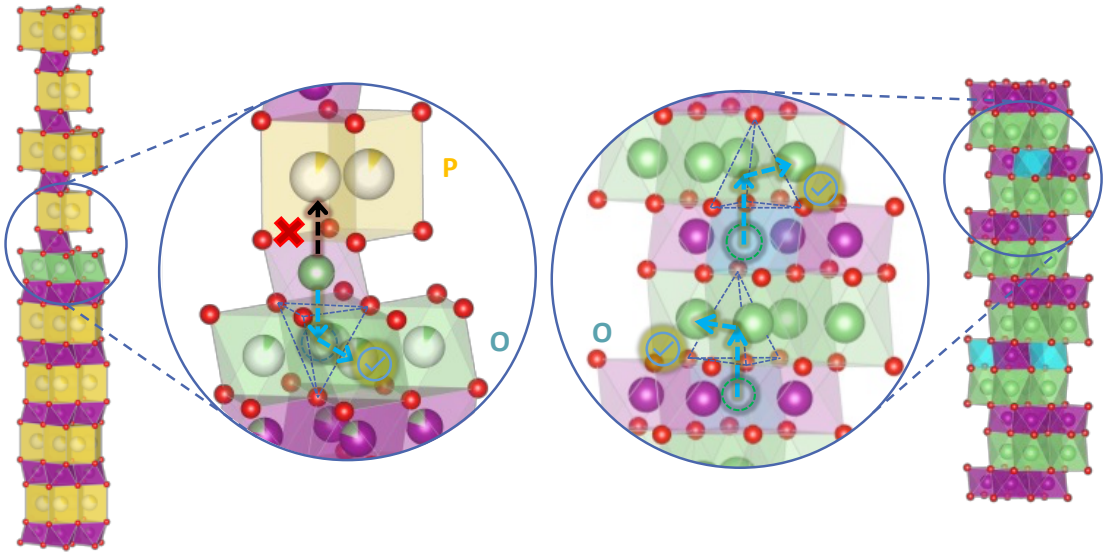

Figure 3.16: Schematic comparison of Li migration feasibility between Na-based and Li-based layered oxides. **Left**: In $Na_{0.52}Li_{0.2}Mn_{0.8}O_2$, prismatic (P) coordination in AM layers hinders Li^+ migration from the TM layers into the neighboring prismatic layers, due to geometric incompatibility (red cross).[24, 25] Structural gliding of TM slabs is necessary to transform P-type stacking into O-type coordination to accommodate Li^+. **Right**: In $Li_{0.56}Li_{0.2}Mn_{0.8}O_2$, octahedral sites in AM layers are already available, enabling direct out-of-plane Li^+ migration (blue arrows with checkmarks). This creates Li vacancies in TM layers, which facilitate local in-plane Mn^{4+} rearrangement, thereby facilitating TM migration without large-scale structural distortion.

As shown in the left panel, the initial prismatic coordination environment within AM layers of $Na_{0.52}Li_{0.2}Mn_{0.8}O_2$ inherently makes Li migration less favorable in energy.[24, 25] Li cannot move out of TM layers until TM slab gliding induced upon charging generates octahedral sites that can accommodate Li ions in the expanding O2 domains. Then Mn has space to migrate within the TM layers, leading to the loss of superstructure pattern.

While the right panel provides the detailed migration pathway in $Li_{0.56}Li_{0.2}Mn_{0.8}O_2$ with the lowest energy barrier: Li ions in TM layers first hop into the face-shared tetrahedral

sites in AM layers and then hop to the adjacent octahedral sites.[26] The left vacancies subsequently enable local rearrangement of neighboring Mn^{4+} ions within the TM layers. The inherent availability of octahedral sites in the AM layers, facilitating direct Li^+ migration from the TM layers without requiring energetically costly slab gliding.

These results provide broader insight into one of the central bottlenecks of oxygen-redox cathodes. Although oxygen redox has been widely explored as a route to higher energy density in next-generation layered cathodes, its practical implementation is often limited by voltage hysteresis, structural degradation, and poor cycling reversibility.[27] A major origin of this instability is TM migration during charge, which disrupts the local structure and undermines the reversibility of the oxygen-redox process.[6] In this context, $Na_{0.52}Li_{0.2}Mn_{0.8}O_2$ and its Li-exchanged analogue $Li_{0.56}Li_{0.2}Mn_{0.8}O_2$ serve as representative model systems for understanding the structural origin and kinetic nature of TM migration in ribbon-ordered oxygen-redox materials.

A key outcome of this chapter is the establishment of the electrochemical descriptor ΔP, which bridges charge/discharge plateau evolution, local structural transformation, and TM migration. This provides a practical way to quantify migration behavior directly from electrochemical data and connect it to structural evolution. Combined with *ex-situ* and *operando* diffraction analysis, reveals that TM migration is not merely a structural consequence of charging, but a kinetically governed process that follows Arrhenius law. The extracted activation energy therefore provides a quantitative measure of migration kinetics in these layered systems.

Comparison between the Na-based and Li-exchanged materials further shows that

cation coordination geometry plays a decisive role in controlling migration. In $Na_{0.52}Li_{0.2}Mn_{0.8}O_2$, the initial prismatic coordination in the AM layer makes Li migration energetically unfavorable, so TM migration is strongly coupled to slab gliding and the formation of O2 domains during charge. By contrast, in $Li_{0.56}Li_{0.2}Mn_{0.8}O_2$, the availability of octahedral AM-layer sites lowers the kinetic barrier for Li migration and consequently facilitates Mn rearrangement. This comparison highlights that the local coordination environment is not a passive structural feature, but an active kinetic regulator of TM migration and oxygen-redox reversibility.

3.4 Conclusion

This chapter systematically investigated the structural and electrochemical implications of TM migration in layered oxygen-redox cathodes, using $Na_{0.52}Li_{0.2}Mn_{0.8}O_2$ and its Li-exchanged counterpart $Li_{0.56}Li_{0.2}Mn_{0.8}O_2$ as representative model systems. A central outcome of this work is the introduction of the electrochemical descriptor ΔP, defined from the difference between charge and discharge plateau-capacity proportions. This descriptor links electrochemical behavior with local structural evolution and provides a quantitative measure of TM migration kinetics. The Arrhenius behavior of ΔP further enabled extraction of the apparent activation energy for migration.

In the P2-type Na-based layered oxide, the prismatic coordination environment in the AM layer initially suppresses Li migration from the TM layers. Upon charging, Na extraction triggers TM slab gliding, which progressively induces the formation of octahedral O2-type sites necessary to accommodate Li ions , thereby enabling subsequent Mn migration and loss of ribbon superstructure. This process is accompanied by increasing

stacking disorder and reduced plateau reversibility, particularly at elevated temperatures, confirming that TM migration is kinetically accelerated under conditions that favor structural rearrangement.

In contrast, the Li-exchanged analogue inherently contains octahedral AM-layer sites that can directly accommodate Li ions leaving the TM layer. This lowers the kinetic barrier for Li migration and facilitates local Mn rearrangement without the need for extensive slab gliding. As a result, TM migration occurs more readily in the Li-based material, consistent with its lower apparent activation energy and its shorter discharge plateau. These results demonstrate that cation coordination geometry and stacking sequence fundamentally control the migration pathway and kinetics.

This work advances understanding of the structural origin of irreversible oxygen-redox behavior in layered cathodes. By showing that TM migration is a kinetically controlled process and by quantitatively linking it to both electrochemical signatures and local structural evolution, this chapter provides a more mechanistic framework for interpreting voltage hysteresis and structural degradation in oxygen-redox materials.

From a materials-design perspective, the identification of TM migration as a kinetically controlled process suggests clear strategies for mitigation. One approach is to engineer TM-layer motifs that increase the migration distance or geometrically frustrate in-plane rearrangement, as exemplified by more robust ordered frameworks such as $Na_2Mn_3O_7$ systems.[28] Another is to introduce electrochemically inactive or less mobile cations that act as kinetic obstacles along migration pathways, thereby suppressing vacancy-assisted TM rearrangement during charge. These strategies may help retain the

reversibility of oxygen redox while reducing voltage hysteresis and structural degradation. More generally, the descriptor developed here provides a useful framework for evaluating migration kinetics in future layered cathodes and for guiding the design of higher-energy materials with improved structural stability.

3.5 Appendix

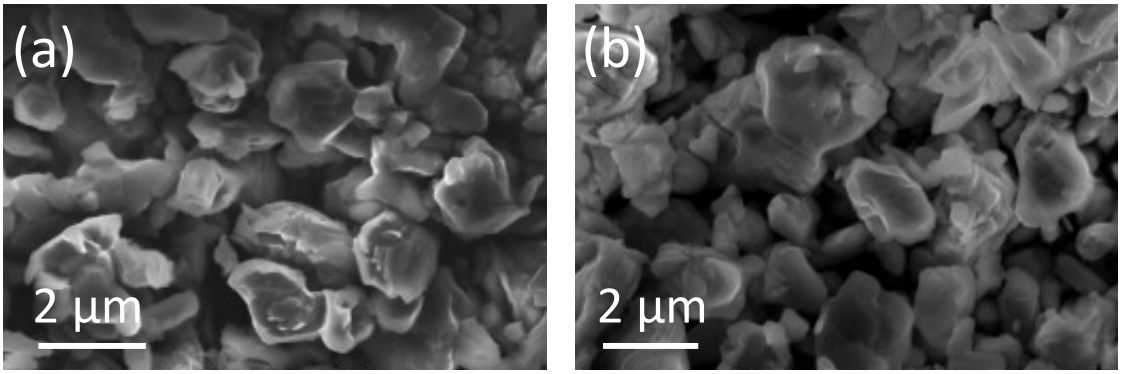

Figure S3.1: SEM images of (a) pristine $Na_{0.52}Li_{0.2}Mn_{0.8}O_2$ and (b) pristine $Li_{0.56}Li_{0.2}Mn_{0.8}O_2$.

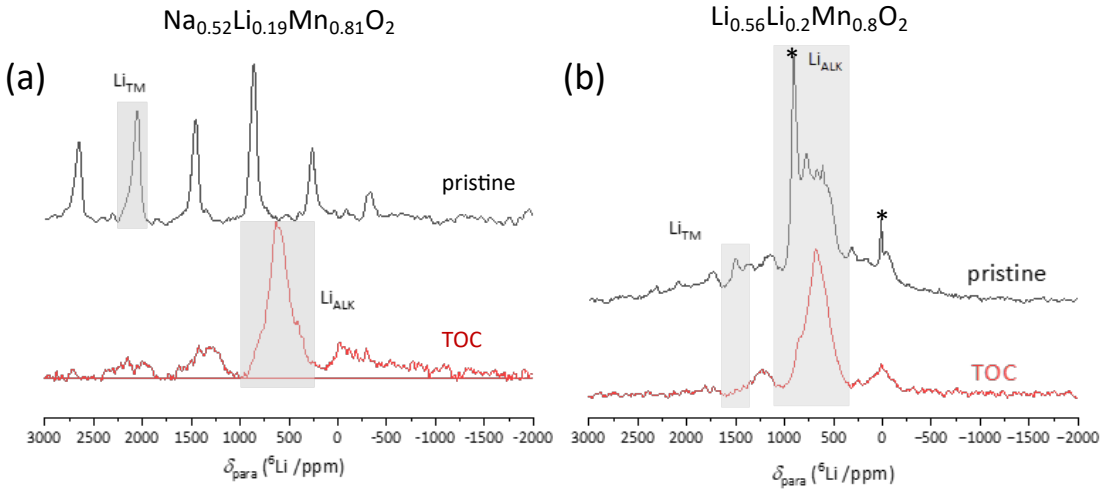

Figure S3.2: (a) ^{7}Li magic angle spinning (MAS, υ_R = 37037 Hz) solid state NMR spectra of $Na_{0.52}Li_{0.2}Mn_{0.8}O_2$ at pristine and TOC. (b) ^{7}Li MAS NMR spectra of pristine $Li_{0.56}Li_{0.2}Mn_{0.8}O_2$ and TOC sample. The sharp peaks marked with an asterisk arise from the bromide salt residual from ion-exchange synthesis.

Table S3.1: Atomic coordinates of the layers required for describing O2-O6 stacking faults for $Li_{0.56}Li_{0.2}Mn_{0.8}O_2$ in the FAULTS program.

Layer 1					
Number	Atom name	x	y	z	Occupancy
1	Mn4+	0	0	0	0.8
2	Li1+	0	0	0	0.2
3	O2-	1/3	-1/3	0.105	1
4	O2-	-1/3	-2/3	-0.105	1
5	Li1+	0	0	0.25	0.56
Layer 2					
Number	Atom name	x	y	z	Occupancy
1	Mn4+	1/3	-1/3	0	0.8
2	Li1+	1/3	-1/3	0	0.2
3	O2-	0	0	0.105	1
4	O2-	-1/3	-2/3	-0.105	1
5	Li1+	2/3	1/3	0.25	0.56
Layer 3					
Number	Atom name	x	y	z	Occupancy
1	Mn4+	2/3	1/3	0	0.8
2	Li1+	2/3	1/3	0	0.2
3	O2-	0	0	0.105	1
4	O2-	1/3	-1/3	-0.105	1
5	Li1+	2/3	1/3	0.25	0.56
Layer 4					
Number	Atom name	x	y	z	Occupancy
1	Mn4+	0	0	0	0.8
2	Li1+	0	0	0	0.2
3	O2-	-1/3	-2/3	0.105	1

4	O2-	1/3	-1/3	-0.105	1
5	Li1+	1/3	-1/3	0.25	0.56
Layer 5					
Number	Atom name	x	y	z	Occupancy
1	Mn4+	1/3	-1/3	0	0.8
2	Li1+	1/3	-1/3	0	0.2
3	O2-	-1/3	-2/3	0.105	1
4	O2-	0	0	-0.105	1
5	Li1+	1/3	-1/3	0.25	0.56
Layer 6					
Number	Atom name	x	y	z	Occupancy
1	Mn4+	2/3	1/3	0	0.8
2	Li1+	2/3	1/3	0	0.2
3	O2-	1/3	-1/3	0.105	1
4	O2-	0	0	-0.105	1
5	Li1+	0	0	0.25	0.56
Layer 7					
Number	Atom name	x	y	z	Occupancy
1	Mn4+	1/3	-1/3	0	0.8
2	Li1+	1/3	-1/3	0	0.2
3	O2-	0	0	0.105	1
4	O2-	-1/3	-2/3	-0.105	1
5	Li1+	1/3	-1/3	0.25	0.56
Layer 8					
Number	Atom name	x	y	z	Occupancy
1	Mn4+	1	0	0	0.8
2	Li1+	1	0	0	0.2
3	O2-	2/3	1/3	0.105	1
4	O2-	1/3	-1/3	-0.105	1

5	Li1+	1	0	0.25	0.56
Layer 9					
Number	Atom name	x	y	z	Occupancy
1	Mn4+	2/3	-2/3	0	0.8
2	Li1+	2/3	-2/3	0	0.2
3	O2-	1/3	-1/3	0.105	1
4	O2-	0	-1	-0.105	1
5	Li1+	2/3	-2/3	0.25	0.56
Transition Vector between layers					
$[t_x\ t_y\ t_z]=[0\ 0\ 0.5]$					

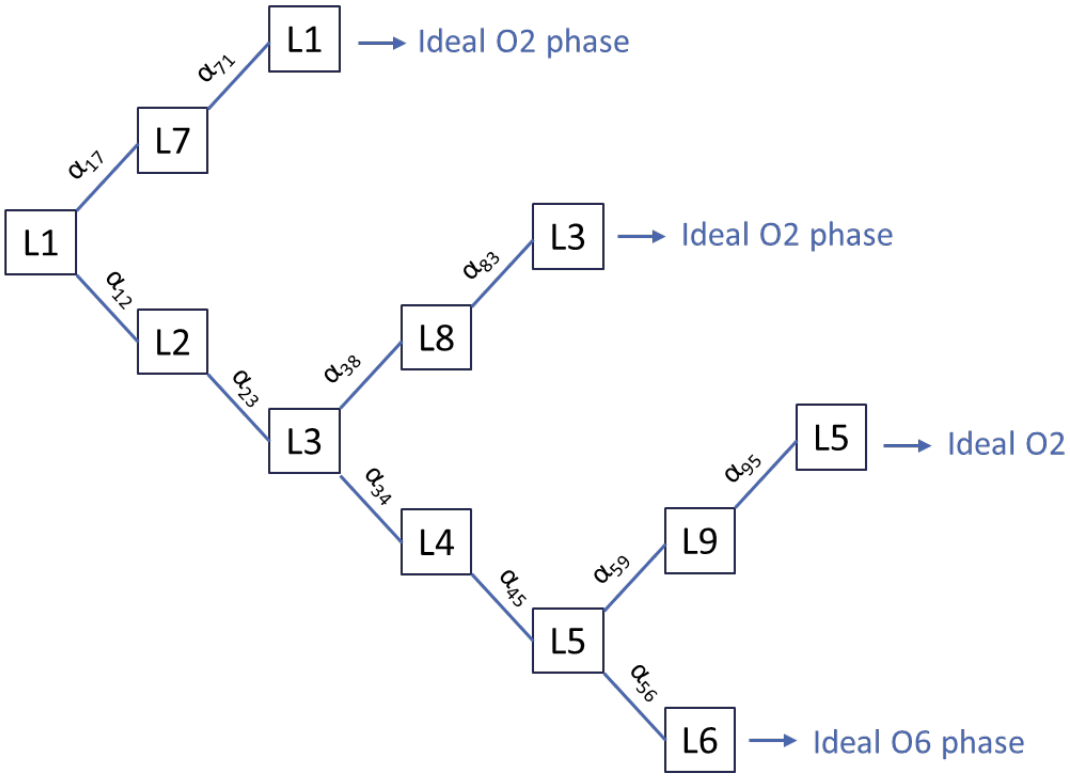

Figure S3.3: Possible layer transitions for $Li_{0.56}Li_{0.2}Mn_{0.8}O_2$ containing O2-O6 type stacking faults, where α_{ij} is the probability of transition from layer i to layer j.

Table S3.2: Rietveld refinement results of the XRD pattern of $Li_{0.56}Li_{0.2}Mn_{0.8}O_2$ using FAULTS within the FullProf software package.

$$\alpha_{ij} = \begin{bmatrix} 0 & 0.76926 & 0 & 0 & 0 & 0 & 0.23074 & 0 & 0 \\ 0 & 0 & 1 & 0 & 0 & 0 & 0 & 0 & 0 \\ 0 & 0 & 0 & 0.76926 & 0 & 0 & 0 & 0.23074 & 0 \\ 0 & 0 & 0 & 0 & 1 & 0 & 0 & 0 & 0 \\ 0 & 0 & 0 & 0 & 0 & 0.76926 & 0 & 0 & 0.23074 \\ 1 & 0 & 0 & 0 & 0 & 0 & 0 & 0 & 0 \\ 1 & 0 & 0 & 0 & 0 & 0 & 0 & 0 & 0 \\ 0 & 0 & 1 & 0 & 0 & 0 & 0 & 0 & 0 \\ 0 & 0 & 0 & 0 & 1 & 0 & 0 & 0 & 0 \end{bmatrix}$$

$a = b = 2.83377$ Å; $c = 9.78370$ Å; Chi2 = 9.9043; R-Factor = 4.7493%

Table S3.3: Atomic coordinates of the layers required for describing P2-O2 stacking faults for $Na_{0.52}Li_{0.2}Mn_{0.8}O_2$ in the FAULTS program. Layers 1 and 2 had transition vectors that would make P2-type layers, whereas layers 3–6 had transition vectors that would make O2-type layers.

Layer 1					
Number	Atom name	x	y	z	Occupancy
1	Mn4+	0	0	0	0.8
2	Li1+	0	0	0	0.2
3	O2-	2/3	1/3	0.188	1
4	O2-	1/3	2/3	-0.188	1
5	Na1+	0	0	0.5	0.26
6	Na1+	1/3	2/3	0.5	0.26
Layer 2					
Number	Atom name	x	y	z	Occupancy
1	Mn4+	0	0	0	0.8
2	Li1+	0	0	0	0.2
3	O2-	1/3	2/3	0.188	1
4	O2-	2/3	1/3	-0.188	1

5	Na1+	2/3	1/3	0.5	0.26
6	Na1+	0	0	0.5	0.26
Layer 3					
Number	Atom name	x	y	z	Occupancy
1	Mn4+	0	0	0	0.8
2	Li1+	0	0	0	0.1
3	O2-	2/3	1/3	0.188	1
4	O2-	1/3	2/3	-0.188	1
5	Li1+	0	0	0.42	0.1
Layer 4					
Number	Atom name	x	y	z	Occupancy
1	Mn4+	0	0	0	0.8
2	Li1+	0	0	0	0.1
3	O2-	1/3	2/3	0.188	1
4	O2-	2/3	1/3	-0.188	1
5	Li1+	0	0	0.42	0.1
Layer 5					
Number	Atom name	x	y	z	Occupancy
1	Mn4+	0	0	0	0.8
2	Li1+	0	0	0	0.1
3	O2-	2/3	1/3	0.188	1
4	O2-	1/3	2/3	-0.188	1
5	Li1+	1/3	2/3	0.42	0.1
Layer 6					
Number	Atom name	x	y	z	Occupancy
1	Mn4+	0	0	0	0.8
2	Li1+	0	0	0	0.1
3	O2-	1/3	2/3	0.188	1
4	O2-	2/3	1/3	-0.188	1

5	Li1+	2/3	1/3	0.42	0.1

Table S3.4: Transition probability matrix and transition vectors to describe the layer transitions of $Na_{0.52}Li_{0.2}Mn_{0.8}O_2$ containing P2-O2 intergrowth while varying the percentage of O2-type layers randomly interspersed within the structure.

α_{ij}: transition probability from layer *i* to layer *j*
$\alpha_{ij} = \begin{bmatrix} 0 & 1-x & 0 & x/2 & 0 & x/2 \\ 1-x & 0 & x/2 & 0 & x/2 & 0 \\ 0 & 1-x & 0 & x/2 & 0 & x/2 \\ 1-x & 0 & x/2 & 0 & x/2 & 0 \\ 0 & 1-x & 0 & x/2 & 0 & x/2 \\ 1-x & 0 & x/2 & 0 & x/2 & 0 \end{bmatrix}$, x is varied from 0 (ordered P2) to 1 (ordered O2)
T_{ij}: transition vectors from layer *i* to layer *j*
$T_{ij} = \begin{bmatrix} (000) & (001) & (000) & (001) & (000) & (001) \\ (001) & (000) & (001) & (000) & (001) & (000) \\ (000) & (\frac{2}{3},\frac{1}{3},0.84) & (000) & (\frac{2}{3},\frac{1}{3},0.84) & (000) & (\frac{1}{3},\frac{2}{3},0.84) \\ (\frac{1}{3},\frac{2}{3},0.84) & (000) & (\frac{1}{3},\frac{2}{3},0.84) & (000) & (\frac{2}{3},\frac{1}{3},0.84) & (000) \\ (000) & (\frac{1}{3},\frac{2}{3},0.84) & (000) & (\frac{2}{3},\frac{1}{3},0.84) & (000) & (\frac{1}{3},\frac{2}{3},0.84) \\ (\frac{2}{3},\frac{1}{3},0.84) & (000) & (\frac{2}{3},\frac{1}{3},0.84) & (000) & (\frac{1}{3},\frac{2}{3},0.84) & (000) \end{bmatrix}$

3.6 References

1. W. Li, E. M. Erickson and A. Manthiram, *Nature Energy*, 2020, **5**, 26-34.

2. N. Yabuuchi, K. Kubota, M. Dahbi and S. Komaba, *Chemical Reviews*, 2014, **114**, 11636-11682.

3. W. E. Gent, K. Lim, Y. Liang, Q. Li, T. Barnes, S. J. Ahn, K. H. Stone, M. McIntire, J. Hong, J. H. Song, Y. Li, A. Mehta, S. Ermon, T. Tyliszczak, D. Kilcoyne, D. Vine, J. H. Park, S. K. Doo, M. F. Toney, W. Yang, D. Prendergast and W. C. Chueh, *Nature Communications*, 2017, **8**, 2091.

4. J. J. Marie, R. A. House, G. J. Rees, A. W. Robertson, M. Jenkins, J. Chen, S. Agrestini, M. Garcia-Fernandez, K. J. Zhou and P. G. Bruce, *Nature Materials*, 2024, **23**, 818-825.

5. T. Cui, J. Xu, X. Wang, L. Liu, Y. Xiang, H. Zhu, X. Li and Y. Fu, *Nature Communications*, 2024, **15**, 4742.

6. R. A. House, U. Maitra, M. A. Perez-Osorio, J. G. Lozano, L. Jin, J. W. Somerville, L. C. Duda, A. Nag, A. Walters, K. J. Zhou, M. R. Roberts and P. G. Bruce, *Nature*, 2020, **577**, 502-508.

7. Z. Yang, J. Zhong, J. Feng, J. Li and F. Kang, *Advanced Functional Materials*, 2021, **31**, 2103594.

8. E. J. Kim, P. A. Maughan, E. N. Bassey, R. J. Clément, L. A. Ma, L. C. Duda, D. Sehrawat, R. Younesi, N. Sharma and C. P. Grey, *Advanced Energy Materials*, 2022, **12**, 2102325.

9. M. Ke, M. Wan, W. Dong, T. Wei, H. Dou and X. Zhang, *Next Materials*, 2025, **6**, 100480.

10. Y. Li, G. Liu, J. Che, L. Chen, X. Wang, G. Wang, L. Lei, J. Hou, S. Li, J. Wang, Y. Xu and Y. Zhao, *Interdisciplinary Materials*, 2025, **4**, 24-51.

11. J. Rodriguez-Carvajal and T. Roisnel, *IUCr Newsletter*, 1998.

12. T. Roisnel and J. Rodríguez-Carvajal, *R. Delhez E J. Mittenmeijer*, 2000, 118-123.

13. K. Momma and F. Izumi, *Applied Crystallography*, 2011, **44**, 1272-1276.

14. C. Delmas, C. Fouassier and P. Hagenmuller, *Physica B+C*, 1980, **99**, 81-85.

15. N. Yabuuchi, R. Hara, M. Kajiyama, K. Kubota, T. Ishigaki, A. Hoshikawa and S. Komaba, *Advanced Energy Materials*, 2014, **4**.

16. J. W. Somerville, A. Sobkowiak, N. Tapia-Ruiz, J. Billaud, J. G. Lozano, R. A. House, L. C. Gallington, T. Ericsson, L. Häggström and M. R. Roberts, *Energy & Environmental Science*, 2019, **12**, 2223-2232.

17. V. Saïbi, L. Castro, I. Sugiyama, S. Belin, C. Delmas and M. Guignard, *Chemistry of Materials*, 2023, **35**, 8540-8550.

18. F. Tournadre, L. Croguennec, I. Saadoune, D. Carlier, Y. Shao-Horn, P. Willmann and C. Delmas, *Journal of Solid State Chemistry*, 2004, **177**, 2790-2802.

19. Y. H. Luo, Q. L. Pan, H. X. Wei, Y. D. Huang, L. B. Tang, Z. Y. Wang, C. Yan, J. Mao, K. H. Dai, Q. Wu, X. H. Zhang and J. C. Zheng, *Advanced Energy Materials*, 2023, **13**, 2300125.

20. L. Mu, D. Hou, E. E. Foley, M. Dai, J. Zhang, Z. Jiang, M. M. Rahman, Y. Fu, L. Ma, E. Hu, S. Sainio, D. Nordlund, J. Liu, J. M. Hu, Y. Liu, R. J. Clément and F. Lin, *Journal of the American Chemical Society*, 2024, **146**, 26916-26925.

21. J. M. Paulsen, R. A. Donaberger and J. R. Dahn, *Chemistry of Materials*, 2000, **12**, 2257-2267.

22. C. Delmas, J. J. Braconnier and P. Hagenmuller, *Materials Research Bulletin*, 1982, **17**, 117-123.

23. A. R. Armstrong and P. G. Bruce, *Nature*, 1996, **381**, 499-500.

24. M. D. Radin and A. Van der Ven, *Chemistry of Materials*, 2016, **28**, 7898-7904.

25. J. Hadler-Jacobsen and S. K. Schnell, *Advanced Materials Interfaces*, 2022, **9**, 2200014.

26. K. Kang and G. Ceder, *Physical Review B*, 2006, **74**, 094105.

27. G. Assat and J. M. Tarascon, *Nature Energy*, 2018, **3**, 373-386.

28. A. Tsuchimoto, X. M. Shi, K. Kawai, B. Mortemard de Boisse, J. Kikkawa, D. Asakura, M. Okubo and A. Yamada, *Nature Communications*, 2021, **12**, 631.

4

The Role of High-Valent d^0 Metal in the Electrochemistry of Disordered Rock-Salt Cathode

Contents

4.1 Introduction

The increasing demand for advanced energy storage systems has intensified the search for next-generation cathode materials of rechargeable batteries with enhanced performance, safety, and affordability. DRX materials have emerged as promising candidates to cathode materials due to their high energy density and versatility in TM selection, moving beyond reliance on cobalt and nickel.[1-5] DRX cathodes are characterized by the $Fm\bar{3}m$ space group with random occupancy of cations (AM and TM ions) in the octahedral 4*a* sites.[5, 6] TM ions are composed of redox-active and d^0 metals, the latter serving to accommodate octahedral distortions since they have no valence electrons.[1, 7, 8] Lithium diffusion in these cathodes occurs predominantly via percolating 0-TM channels, necessitating an excess amount of lithium.[4, 9]

A persistent challenge in DRX as cathodes for LIBs is the occurrence of irreversible oxygen redox reactions triggered by excess lithium content, which leads to structural degradation and electrochemical instability.[6, 10, 11] To address this issue, incorporating fluorine and high-valent d^0 metals has been demonstrated as an effective strategy to broaden the TM redox reservoir and therefore stabilize the cathode structure.[1, 12-16] Mn-based oxyfluorides have garnered significant research interest due to their advantageous redox potentials, economic feasibility, and environmental friendliness.[2, 14, 17, 18]

In this context, $Li_2Mn_{0.75}W_{0.25}O_2F$ (LMWOF) is designed as a DRX oxyfluoride in which high-valent W^{6+} acts as a charge compensator to stabilize divalent Mn^{2+}. This design enables a double-electron Mn^{2+}/Mn^{4+} redox process, thereby increasing the TM redox reservoir while reducing reliance on oxygen redox, which is typically less reversible.

In this chapter, the influence of incorporating high-valent d^0 metals, specifically W^{6+}, into Mn-based DRX oxyfluoride is systematically investigated. The composition LMWOF is studied with comparison to Li_2MnO_2F (LMOF) which has been widely studied as a model reference compound.[19, 20] The primary objectives of this work are to (i) elucidate the structural modifications induced by W^{6+} incorporation into the LMOF framework, (ii) understand the associated redox behaviour, and (iii) examine the influence of structural modifications on the lithium diffusion during cycling. Furthermore, this study aims to quantify the trade-offs arising from such substitutions, specifically the balance between enhanced redox activity and the potential reduction in lithium diffusion efficiency due to structural distortion or modified ion hopping networks. Through this investigation, we seek to provide deeper insight into the role of high-valent d^0 metal incorporation in DRX-type cathodes and to inform the rational design of next-generation cathodes with improved specific capacity and cycling stability.

4.2 Experimental Section

4.2.1 Material Synthesis

LMWOF and LMOF were synthesized via a mechanochemical ball-milling method. The precursors used were Li_2O (Alfa Aesar, 99.5%), LiF (Alfa Aesar, 99.99%) and MnO (Fisher Scientific UK Ltd, 99.99%), together with WO_3 (Sigma-Aldrich, 99.995%) for LMWOF ,and Mn_2O_3 (Fisher Scientific UK Ltd, 99.99%) for LMOF. A 10% excess of Li_2O, along with stoichiometric amounts of the other precursors (approximately 1.2 g total), was loaded into 15-ml ZrO_2 jars in an Ar-filled glovebox. The mixture was then ball-milled for

40 hours at 450 rpm in a Fritsch Pulverisette 7 planetary ball mill, using 80 ZrO_2 balls (5 mm in diameter) as the grinding media. The milling process was conducted in 5-minute intervals with 12-minute resting periods between each cycle to prevent overheating.

4.2.2 Composition Analysis

The composition of the as-prepared material was confirmed using three methods: ICP-OES, F^--ISE, and Iodometry Titration.

ICP-OES: Approximately 5 mg of the as-prepared material was dissolved in concentrated hydrochloric acid overnight and then diluted 100 times with a 2% nitric acid solution. ICP-OES measurements were performed by the author using a Perkin Elmer Optima 8000 instrument, employing external calibration with a series of standards of known concentrations to establish a linear calibration curve, under the supervision of a trained instrument superuser.

F^--ISE: The dissolved sample was mixed with 29 parts of 15% sodium acetate in deionized water to adjust the pH, followed by the addition of 30 parts of TISAB II solution. The total volume of sample solution was 150 mL. The fluoride concentration was measured using a Mettler Toledo perfectION™ combination fluoride electrode, equipped with a SevenExcellence™ benchtop meter, employing the Known Addition method. Known Addition is a convenient technique for measuring the total concentration of an ion in the presence of a large excess of a complexing agent without calibration curve.The potential was measured before and after the addition of 2 mL of 100 mg/L standard fluoride solution.

Iodometry Titration: The valence of Mn was determined by iodometric titration. Approximately 15 mg of LMWOF was dissolved in 10 mL of concentrated hydrochloric

acid, which had been degassed with argon. Around 10 times excess of fresh potassium iodide was added to the solution, and the mixture was continuously purged with argon while being vigorously stirred. The titration was carried out using a syringe pump to add 0.01 M fresh sodium thiosulfate precisely. A few drops of starch indicator were added near the end point when the dark blue colour of the mixture began to fade. The titration continued until the mixture became completely colourless.

4.2.3 Morphology

SEM images and EDX mapping were captured using a Carl Zeiss Merlin field emission analytical scanning electron microscope at an operating voltage of 10 keV. Pristine and pulverized LMWOF powders were mounted on a stub using carbon tape. The sample holder was transferred using an iLoad chamber to avoid air exposure.

TEM images and electron diffraction patterns were recorded by a high vacuum JEOL 3000F analytical TEM under 200 kV. The sample was transported to the TEM column by means of a Gatan vacuum transfer holder, completely avoiding contact with air and moisture.

4.2.4 Structural characterization

PXRD pattern of the as-prepared material was collected using a Rigaku SmartLab diffractometer using Cu $K_{\alpha 1}$ radiation (λ = 1.54051 Å) equipped with a Ge(220) double bounce monochromator. The diffraction data were analysed using the Rietveld refinement method with GSAS2 software.[21] XPDF data of LMWOF and LMOF at different SOCs were collected at the I15-1 beamline of Diamond Light Source. The mixture of active material

and acetylene black was used to assemble the coin cells. After cycling, the powder was recovered, washed with DMC and dried before being loaded into the 0.7-mm silica glass capillary tubes and sealed in the Ar-filled glovebox. X-ray total scattering data were processed with the Q_{max} of 24 $Å^{-1}$ after subtracting the background of acetylene black. XPDF fitting was carried out using the PDFgui software.[22]

4.2.5 X-ray Spectroscopy

XANES and EXAFS were measured at B18 Diamond Light Source in transmission mode. sXAS spectra (including TEY, TFY, PFY, IPFY) were acquired on three synchrotron sources, including the BL27SU beamline of the RIKEN/JASRI Spring8 synchrotron, the I10 beamline at Diamond Light Source and the 11A beamline of Taiwan Light Source. *Ex-situ* cathode samples were mounted on adhesive carbon tape and measured under 10^{-6} Pa high-vacuum conditions. High-resolution RIXS was carried out at the I21 beamline of Diamond Light Source and the U41-PEAXIS beamline of BESSY II, using excitation energies of 530.75 eV and 531eV, respectively.[23]

4.2.6 Electrochemistry

To prepare the cathode film, 420 mg of raw materials and 120 mg of acetylene black (Alfa Aesar, 99.9+%) were mixed for 6 hours at 300 rpm in Ar-filled 15-ml ZrO_2 jars using 80 ZrO_2 balls (5 mm in diameter) as grinding media in a Fritsch Pulverisette 7 planetary ball mill. This treatment further pulverizes particles and promotes uniform carbon mixing. The milling process was conducted in 5-minute intervals with 1-minute resting periods. Carbon mixing could also be performed using a mortar and pestle, which is a conventional

method. However, in this chapter, the electrochemistry was conducted using the pulverized active material, unless otherwise specified. PTFE (Imperial Chemical Industries, grade G1) was then added to the mixture as a binder, and the mixture was manually combined using a mortar and pestle before being calendared to a thickness of approximately 0.1 mm. The resulting free-standing cathode film consisted of active material, acetylene black, and PTFE in a weight ratio of 7:2:1, with sample loadings typically between 5-10 mg cm^{-2}. Coin cells (CR2032) were assembled using a Li-metal disk (MTI) as a negative electrode and two glass microfibre separators (Whatman) soaked in 140 µL of 1M $LiPF_6$ in EC: EMC = 30:70 vol% electrolyte (DodoChem). All procedures were performed in an Ar-filled glove box. Unless specified, all the cells were cycled at room temperature. For *ex-situ* XRD and XPDF characterization, a mixture of active material and acetylene black was used to assemble the coin cells. Galvanostatic charge-discharge measurements were performed between 1.5 V and 4.8 V at a current density of 10 $mA.g^{-1}$ using a Maccor Series 4000.

DEMS analysis was carried out to study the different gases generated during cell cycling. The set up consisted of a quadrupole mass spectrometer (Thermo Fischer) equipped with a turbomolecular pump (Pfeiffer Vacuum) and mass-flow controllers (Bronkhorst). Two electrode type cells (ECC-Std from EL-CELL) with gas inlet and outlet ports were used for the operando measurements. The cell consisted of the cathode film, Li metal anode, 2 glass microfiber separators soaked in electrolyte (1M $LiPF_6$ in PC). The cell was cycled at a current density of 50 mA/g and a voltage window of 1.5–4.8 V. Ultrapure Ar was used as carrier gas with a purge gas flow of 1 mL/min. The detection limits of the DEMS are below 1 ppm.

4.2.7 Monte Carlo Simulation

The quantification of the tetrahedra-occupied W^{6+} influence on the Li diffusion and percolation was performed by the Monte Carlo simulation. The Dribble package is an open-access GitHub script from the contributors Alexander Urban *et. al*. [24] It is a lattice-model Monte Carlo method for simulating ionic transport in atomic structures, which solves the site percolation problem based on a defined set of percolation rules. For DRX materials, lithium diffusion is widely understood to proceed via so-called 0-TM diffusion channels.[4] In this work, a site-rule criterion was implemented to evaluate Li diffusion pathways. Specifically, the intermediate tetrahedral sites were considered accessible only when coordinated by four Li ions or vacancies, corresponding to 0-TM environments. To apply this criterion, atomic structure files in VASP's POSCAR format were modified to explicitly include tetrahedral sites, and the analysis was performed based on the occupancy of these sites rather than their chemical identity.

Unless otherwise stated, the material synthesis, electrochemical testing, and data analysis presented in this chapter were performed by the author. Specific contributions from collaborators are identified in the relevant sections, particularly for advanced characterization measurements and external analytical services. The interpretation and integration of the results were carried out by the author.

4.3 Results and Discussion

4.3.1 Material Characterization

LMWOF was successfully synthesized via a mechanochemical ball-milling method.

The final composition of the as-synthesized sample was determined from the combined results of ICP-OES (cation ratios), F^--ISE analysis (fluorine content), and iodometric titration (Mn oxidation state). The measured Mn valence was 2.07, consistent with predominantly divalent Mn, while the fluorine content was determined to be 0.121 (mass fraction). Combining these results yields a composition of $Li_{2.017}Mn_{0.731}W_{0.252}O_{2.041}F_{0.953}$, which is in close agreement with the targeted stoichiometry. Detailed measurement data are provided in Tables S4.1–S4.3. These results confirm that the intended charge compensation by W^{6+} successfully stabilizes Mn in a low oxidation state.

PXRD was employed to confirm the phase purity and crystallographic structure of the synthesized materials. As shown in **Figure 4.1(a)**, the diffraction pattern was

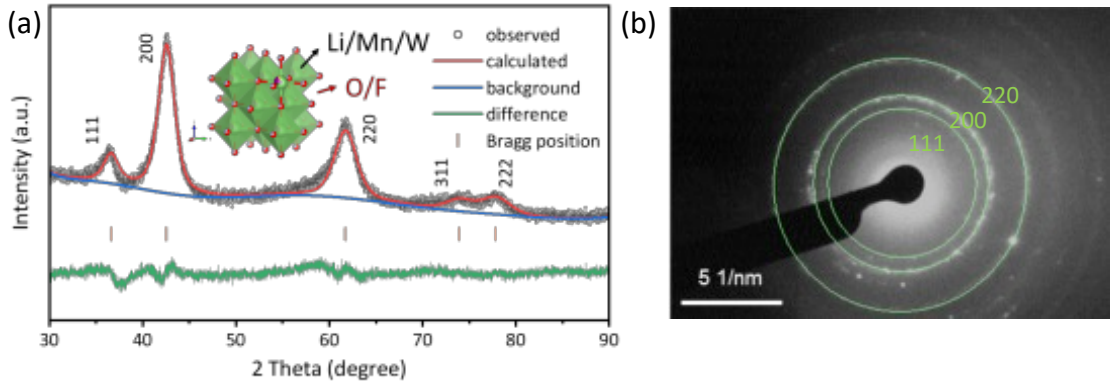

Figure 4.1: (a) Rietveld refinement of the PXRD pattern of pristine LMWOF, which is well described by the $Fm\bar{3}m$ space group. The inset structural scheme highlights the disordered cation distribution and mixed O/F anion occupation. (b) ED pattern of pristine LMWOF exhibiting diffraction rings indexed to (111), (200), and (220) planes, consistent with nanocrystalline DRX structure.

successfully refined and indexed to the $Fm\bar{3}m$ space group, with a refined unit cell parameter of 4.2382(4) Å (refinement details in **Table 4.1**). The inset in Figure 4.1(a) displays a structural model of the DRX, highlighting the random cation distribution across the rock-salt lattice with O/F anions randomly occupying the anion sublattice.

Table 4.1: Structural parameters for LMWOF from Rietveld refinement of PXPD data. Site occupancies were fixed to the analysis result from **Table S4.3**.

Atom	Wyckoff site	x	y	z	Uiso	Occ
Li	4*a*	0	0	0	0.0151(6)	0.672
Mn	4*a*	0	0	0	0.0151(6)	0.244
W	4*a*	0	0	0	0.0151(6)	0.084
O	4*b*	0.5	0.5	0.5	0.0112(9)	0.680
F	4*b*	0.5	0.5	0.5	0.0112(9)	0.318
Space Group: $Fm\bar{3}m$; wR = 4.41%; GOF = 1.13 $a = b = c = 4.2382(4)$ Å; $\alpha = \beta = \gamma = 90°$; $V = 76.127(20)$ Å^3						

Complementary ED pattern (**Figure 4.1(b)**) shows diffraction rings corresponding to the (111), (200), and (220) planes. The presence of rings, rather than intensity spots, indicates the nanoscale grain size typical for DRX synthesized by ball-milling. This is confirmed by morphological analysis using SEM (**Figure 4.2(a–b)**) that reveals nanosized

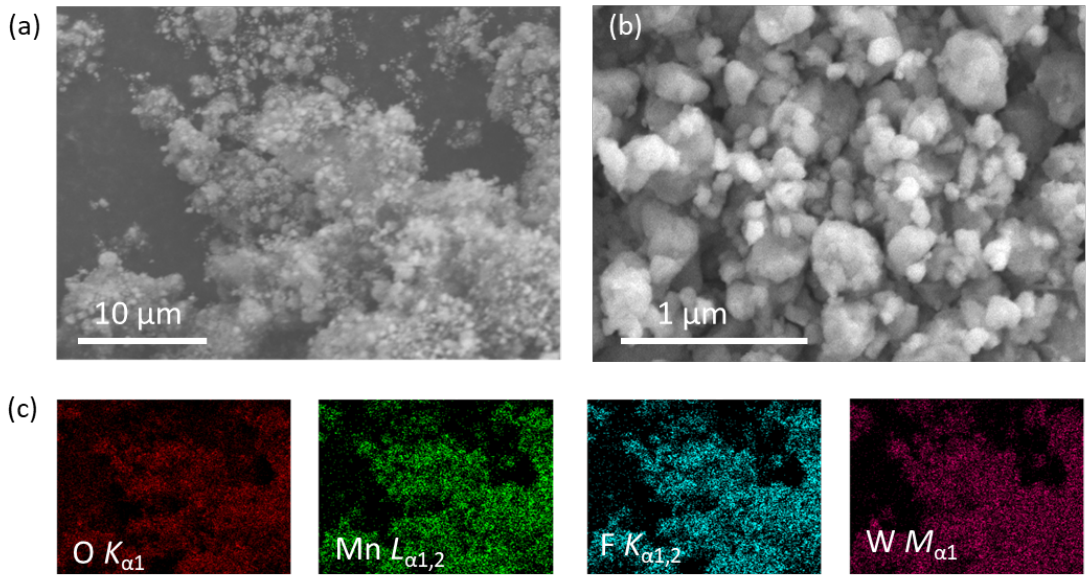

Figure 4.2: (a-b) SEM images of LMWOF at different magnifications, showing agglomerated secondary particles composed of nanocrystalline primary grains. (c) EDX mapping of the area in (a), confirming uniform distribution of O, Mn, F, and W throughout the sample.

primary particles (~200 nm) aggregate to form larger secondary particles of approximately

1 μm. EDX mapping (**Figure 4.2(c)**) confirms a homogeneous distribution of Mn, W, O, and F throughout the sample, suggesting no large-scale phase segregation or inhomogeneity in the bulk composition.

In summary, the combined results from PXRD, ED, and SEM/EDX confirm the successful synthesis of a homogeneous single-phase DRX material with the targeted composition, particle morphology, and nanostructure.

4.3.2 Electrochemistry

The electrochemical performance of LMWOF was evaluated and compared to its W-free analogue LMOF to assess the effect of high-valent W^{6+} substitution on redox chemistry and cycling behavior (**Figure 4.3**). Both materials were tested using electrodes composed of pulverized active materials to improve conductivity and Li^+ accessibility.

Figure 4.3(a) shows the first galvanostatic charge-discharge profile of LMWOF at a current density of 10 mA g^{-1}. A sloping voltage curve typical of DRX cathodes was observed, with a total charge capacity of 266 mAh g^{-1}. This value corresponds to the extraction of approximately 1.5 Li^+ per formula unit, aligning well with the theoretical capacity from the full Mn^{2+}/Mn^{4+} redox, represented by the dashed line in **Figure 4.3(a)**. The electrochemical behavior indicates that substituting W^{6+} effectively introduce Mn^{2+} into the pristine material, facilitating a reversible two-electron redox process upon cycling.

In comparison, LMOF (**Figure 4.3(b)**) delivered an even higher initial charge capacity (~330 mAh g^{-1}), substantially exceeding the theoretical one-electron Mn^{2+}/Mn^{3+} redox limit (~224 mAh g^{-1}). This surplus capacity arises from the activation of additional oxygen

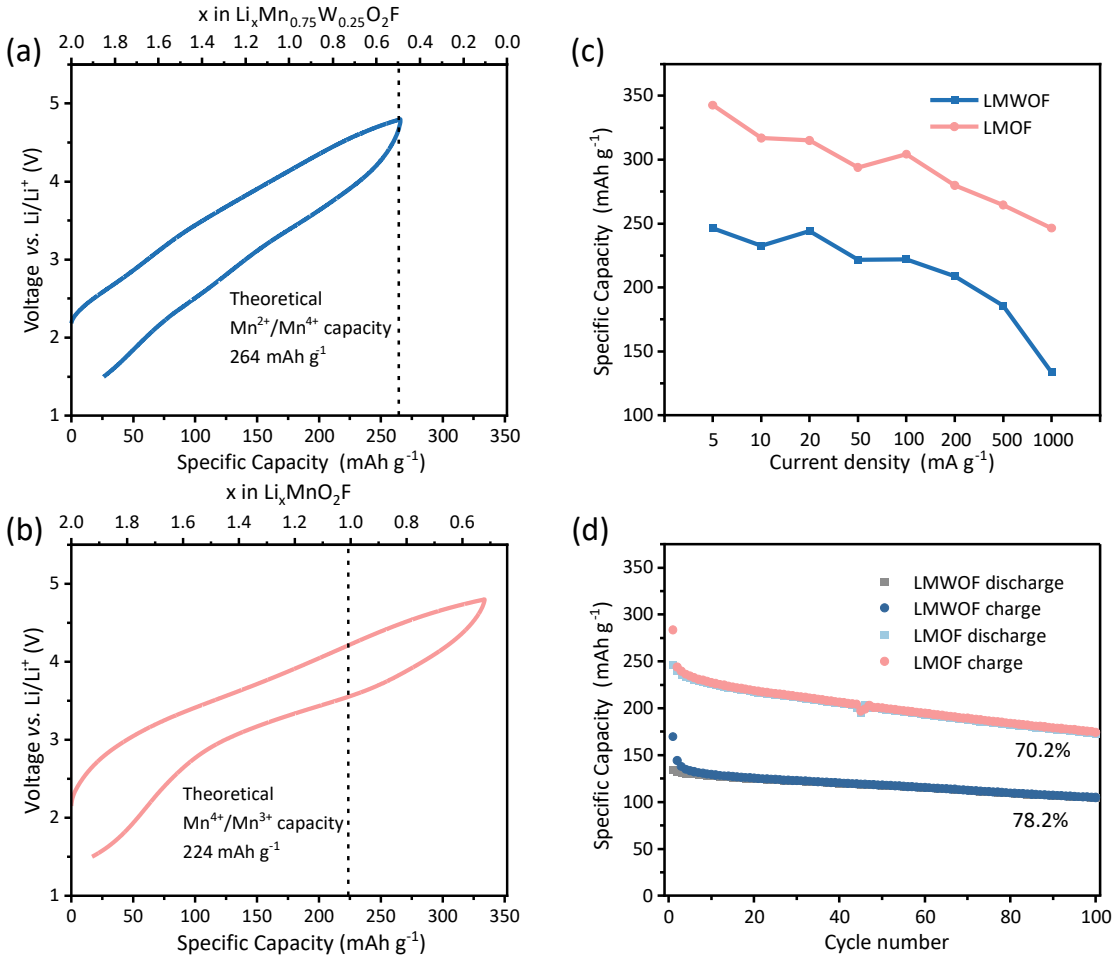

Figure 4.3: Electrochemical comparison of LMWOF and LMOF. (a-b) First galvanostatic charge/discharge voltage profiles of LMWOF and LMOF at a current density of 10 mA g^{-1}. (c) Rate capability of LMWOF and LMOF at the current densities from 5-1000 mA g^{-1}, showing the slightly superior kinetics of LMOF. (d) Long-term cycling performance at a current density of 1000 mA g^{-1}, demonstrating improved capacity retention for LMWOF due to stable Mn^{2+}/Mn^{4+} redox behavior.

redox processes at voltages above 4.3 V, as has been widely reported for DRX-type cathodes lacking redox-inactive dopants.[19, 25-27] However, such high-voltage oxygen activity often correlates with structural instability and long-term degradation.

The rate performance comparison (**Figure 4.3(c)**) showed that LMOF retained slightly higher capacities at elevated current densities, indicating faster electrochemical kinetics. Nevertheless, the long-term cycling results (**Figure 4.3(d)**) revealed that LMWOF

maintains superior capacity retention at a current density of 1000 mA g^{-1}. After 100 cycles, LMWOF retained ~78.2% of its initial capacity, while LMOF dropped to 70.2%. This pronounced contrast reflects the enhanced stability of cationic Mn-based redox chemistry in LMWOF, attributed to suppression of irreversible oxygen activity and structural degradation.

To further probe the influence of the voltage window, the electrochemical performance of LMWOF was evaluated under varied upper cut-off voltages, as shown in **Figure 4.4**. The electrochemistry results show that increasing the cut-off to 5.0 V enhances the initial

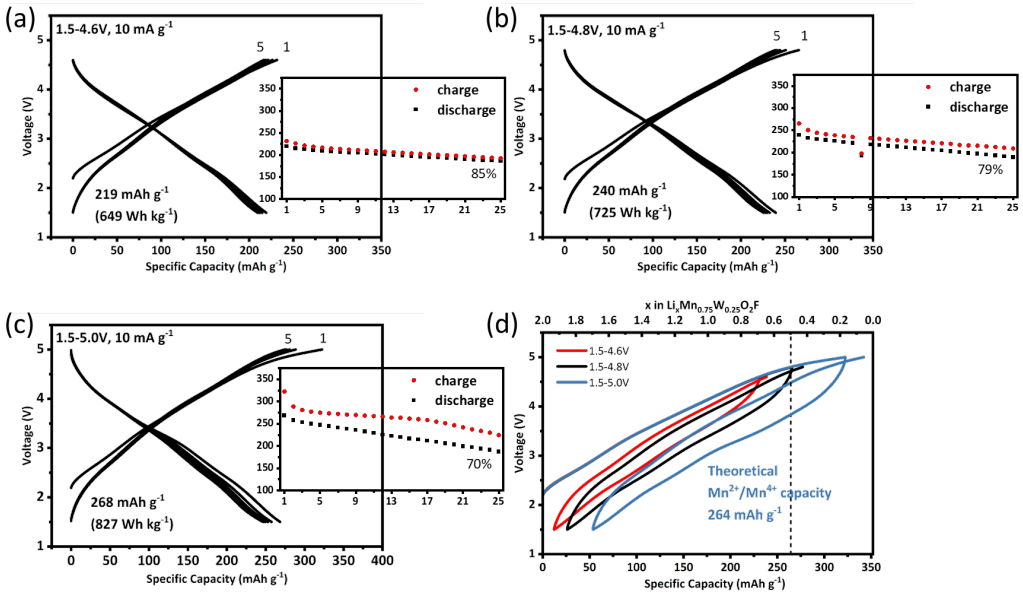

Figure 4.4: (a-c) The first 5 load curves of LMWOF cycled within different voltage windows with initial discharge capacities and energy densities annotated, attached with the corresponding long-term cycling performance; (d) Comparison of cyclic voltammetry curves of LMWOF under various upper cut-off voltages, highlighting the impact of voltage range on redox behavior and capacity utilization.

capacity due to oxygen redox activation, but leads to faster capacity fading during cycling, indicating a trade-off between energy density and stability. It is worth noting that the electrochemical performance is closely associated with electron conductivity of electrode.

As shown in **Figure 4.5**, pulverization via ball milling with acetylene black was used to enhance interparticle contact and electrode consistency.[28] While XRD confirmed that this treatment did not alter the bulk structure, contributing to more reliable electrochemical performance compared to unprocessed samples.

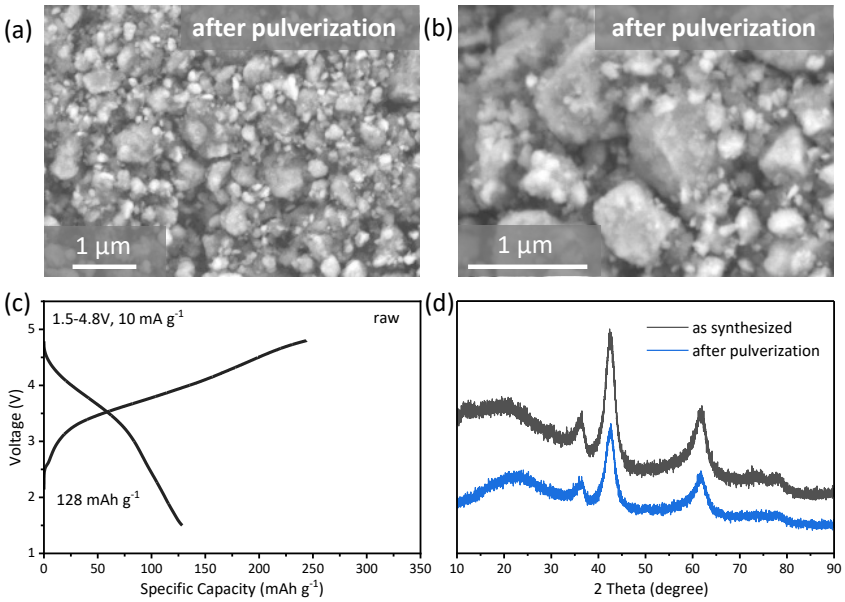

Figure 4.5: (a-b) SEM images at different magnifications of LMWOF after pulverization as ball-milling the as-synthesized material with acetylene black. (c) First load curve of as-synthesized LMWOF without pulverization, indicating limited capacity due to poor conductivity. (d) PXRD patterns of LMWOF before and after pulverization, illustrating the preservation of bulk structure post-pulverization.

4.2.3 Charge Compensation Analysis from Bulk to Surface

A series of spectroscopic characterizations were performed at key SOCs over the first cycle, as marked on the galvanostatic load curve of LMWOF in **Figure 4.6(a)**. By using TEY, PFY and IPFY, we have been able to probe the evolution of oxidation states of TM and oxygen during cycling, revealing the depth dependence in the charge-compensation process.

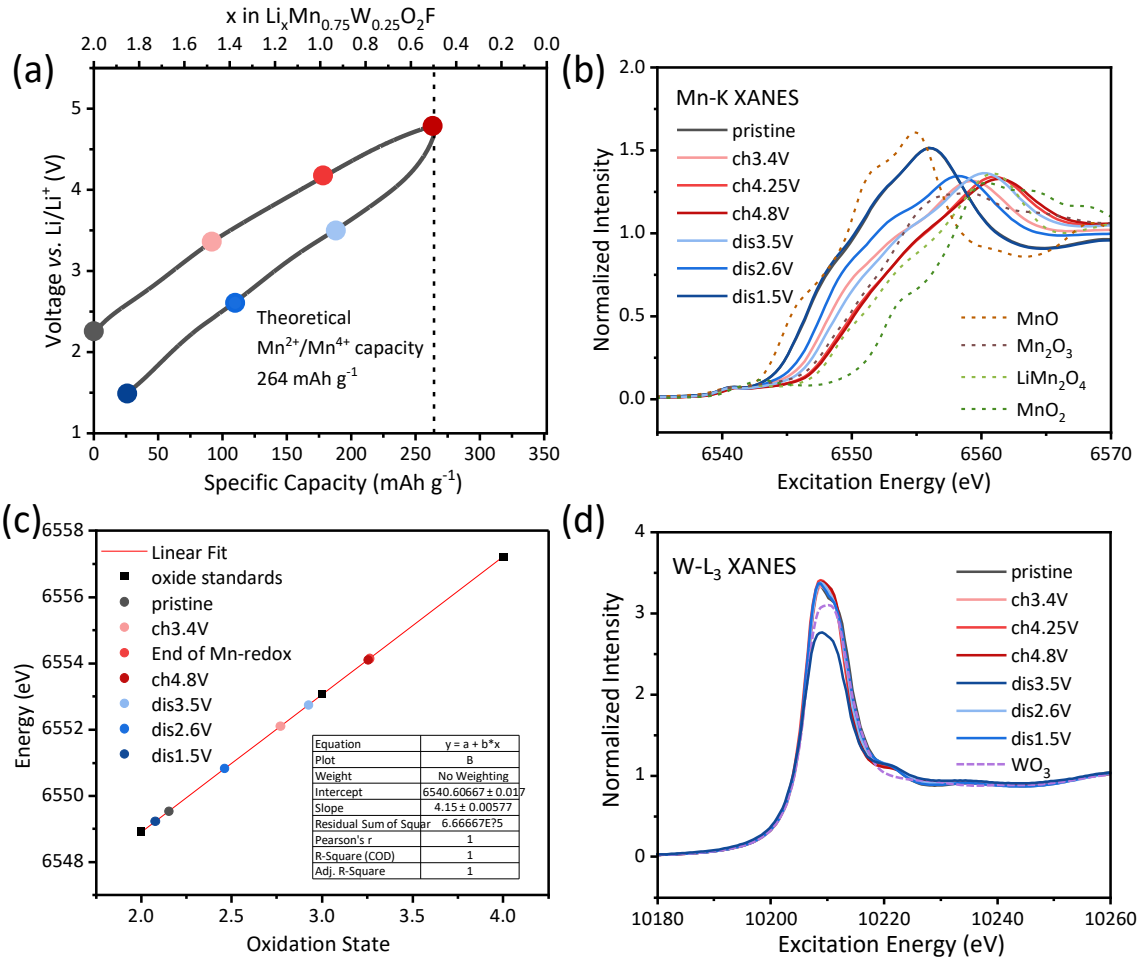

Figure 4.6: (a) Galvanostatic load curve of LMWOF (1.5–4.8 V, 10 mA g^{-1}) with key SOCs over the first cycle for *ex-situ* spectroscopic measurements; (b) Mn K-edge XANES spectra of LMWOF at key SOCs along with standard samples; (c) Linear fit correlating the Mn oxidation states with the energy of the absorption edge for the key SOCs;[29] (d) W L_3-edge XANES spectra of LMWOF at key SOCs, along with WO_3 as a standard sample, showing W remains in +6 oxidation state.

Mn K-edge XANES spectra in **Figure 4.6(b)** reveals a gradual shift of the absorption edge to higher energy during charge up to 4.25 V, consistent with progressive Mn oxidation. The spectrum at 4.25 V approaches close to that of the $LiMn_2O_4$ standard (Mn in +3.5 oxidation state). Charging further to 4.8 V produces negligible additional shift, indicating that Mn redox is essentially complete by 4.25 V, with subsequent capacity arising from oxygen redox (discussed below). Upon full discharge, the edge returns to its pristine

position. Linear fitting (**Figure 4.6(c)**) quantifies an average Mn oxidation state increase from +2 to ~+3.3, confirming multielectron Mn redox as the primary contributor to capacity below 4.25 V. In contrast, W-L_3 edge spectra (**Figure 4.6(d)**) remain unchanged, verifying that W^{6+} is electrochemically inactive.

Combining various detection modes in sXAS at the Mn $L_{3,2}$-edge, which corresponds to the 2*p*-3*d* electron transition, further clarifies the distribution of Mn redox activity as a function of sample depth (**Figure 4.7**). Bulk-sensitive IPFY spectra (several micrometers

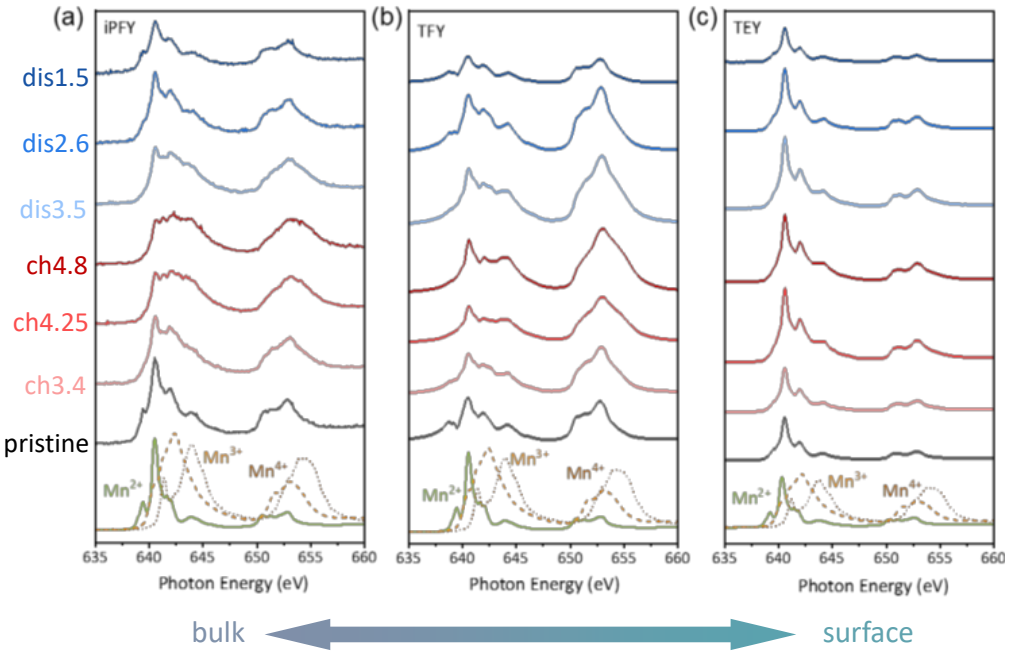

Figure 4.7: Mn $L_{3,2}$-edge spectra of LMWOF at key SOCs during the first cycle obtained in (a) inverse partial fluorescence yield (IPFY), (b) total fluorescence yield (TFY) and (c) total electron yield (TEY) detection modes, together with standard spectra of Mn^{2+} (MnO), Mn^{3+} ($LaMnO_3$), and Mn^{4+} (Li_2MnO_3).

probe depth) reveal clear $Mn^{2+} \rightarrow Mn^{3+}$/ Mn^{4+} oxidation during charge, fully reversed on discharge.[30] TFY spectra (~100 nm probe depth) indicate less oxidation and higher residual Mn^{2+} at TOC (4.8V), while TEY spectra (~5 nm probe depth) display no clear shift,

indicating the surface remains predominantly Mn^{2+}.[31] These results demonstrate that Mn redox is bulk dominated, with the surface acting as a reductive, electrochemically inert passivation layer.

Above 4.25 V, Mn oxidation plateaus while the oxygen redox becomes dominant. The O K-edge PFY spectra shown in **Figure 4.8(a)** capture the evolution of oxygen states.

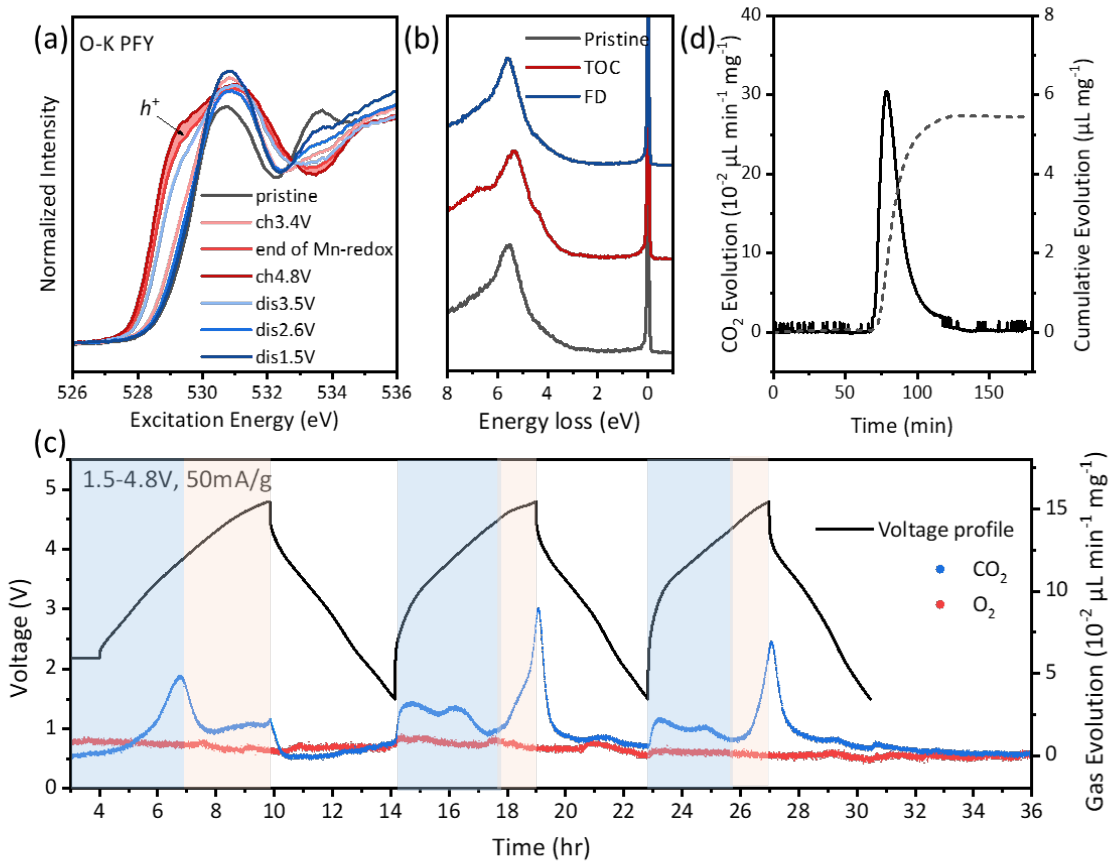

Figure 4.8: (a) O K-edge PFY spectra of LMWOF at key SOCs. (b) O K-edge RIXS spectra of pristine, TOC and FD at an excitation energy of 531 eV. (c) DEMS of LMWOF during the first three cycles within the voltage window of 1.5–4.8V at a current density of 50 mA g^{-1}. The release of O_2 and CO_2 is represented by red and blue dots, respectively, as a function of time. (d) Acid titration test on the electrode using an excess of phosphoric acid, showing CO_2 release and its cumulative evolution.

Below 4.25 V, the pre-edge feature around 529 eV increases in intensity, in correlation

with the removal of electrons from the hybridized Mn 3*d*-O 2*p* orbitals, consistent with Mn oxidation.[19] Above 4.25 V (red region), the intensity of the pre-edge continues to rise without additional Mn oxidation, indicating the formation of electron-hole (h^+) states on lattice oxygen.[32, 33] Upon discharge, the pre-edge returns to its original state. The peak at ~533.5 eV in both pristine and FD spectra is assigned to transitions from *1s* core hole to π* (C=O) orbital, which originates from surface carbonate species.[34]

Depth-dependent analysis of oxygen states was performed using O K-edge TFY and TEY spectra, as shown in **Figure S4.1**. The TFY exhibited similar trend to the PFY data with highlighted area in **Figure 4.8(a)**. In contrast, the TEY spectra showed minimal changes, reinforcing the conclusion that oxygen redox primarily occurs in the bulk, with minimal surface participation.

To investigate whether high-voltage oxygen oxidation leads to the formation of O–O dimers, high-resolution O K-edge RIXS was performed. This technique allows for the differentiation of oxidized oxygen species by analyzing the initial spacing of the vibrational progression peaks arising in the low energy loss region, which serve as a unique fingerprint.[32, 35] O K-edge RIXS spectra of LMWOF, measured at an excitation energy of 531 eV (**Figure 4.8(b)**), do not exhibit any vibrational progression peaks at TOC, excluding the formation of O_2 or other peroxo-like species. This contrasts with Li_2MnO_2F (**Figure S4.2**), where the O K-edge RIXS spectra display significant energy-loss peaks at TOC with initial spacing of 0.2 eV which correspond to molecular O_2 (1.2 Å, 1556 cm^{-1}).

Gas evolution measurements via DEMS investigated if there was oxygen loss upon charge that accounted for the charge capacity. **Figure 4.8(c)** displays that O_2 release was

negligible over the first three cycles. In contrast, 7.39 μL mg^{-1} CO_2 is released in the first cycle peaking at 3.8 V, well below the voltage required for electrolyte decomposition. This aligns with the electrochemical decomposition of surface carbonates.[36] Acid titration (**Figure 4.8(d)**) quantifies the carbonate content at ~1.99 wt% (5.46 μL mg^{-1} CO_2), accounting for ~74% of the CO_2 released in the first cycle. The remaining CO_2 originates from electrolyte oxidation above 4.5 V, which has been observed to derive from the chemical reaction between the electrolyte and released singlet oxygen.[37] In subsequent cycles, CO_2 evolution occurs at lower voltages, consistent with decomposition of CEI-derived carbonates formed during the first charge.[37]

In summary, Li extraction from LMWOF occurs through a sequential charge compensation process involving bulk $Mn^{2+} \rightarrow Mn^{3+}/Mn^{4+}$ redox up to ~4.25 V, followed by the formation of hole states h^+ on lattice oxygen at higher voltages. The oxygen redox is bulk-confined, preventing O_2 release from the surface or the formation of other oxidized oxygen species, and is stabilized by an electrochemically inert passivation layer on the surface.

4.2.4 Long-Range and Short-Range Structural Evolution

The evolution of the long-range crystal structure of LMWOF during the first charge–discharge cycle was tracked using *ex-situ* XRD, as presented in **Figure 4.9**. The diffraction patterns confirm the structural stability of the DRX phase throughout cycling, with no formation of any new crystalline phases. This behavior is typical of DRX materials due to their isotropic and topologically disordered framework, which resists long-range phase transitions even under significant lithium removal.[1]

Upon charging, the diffraction peaks gradually shift toward higher angles, indicating a contraction of the unit cell as lithium ions are extracted. The smallest unit cell volume is observed at 4.8 V. During discharge, the unit cell expands, returning close to its original volume by the fully discharged state. This reversible lattice breathing reflects a solid-

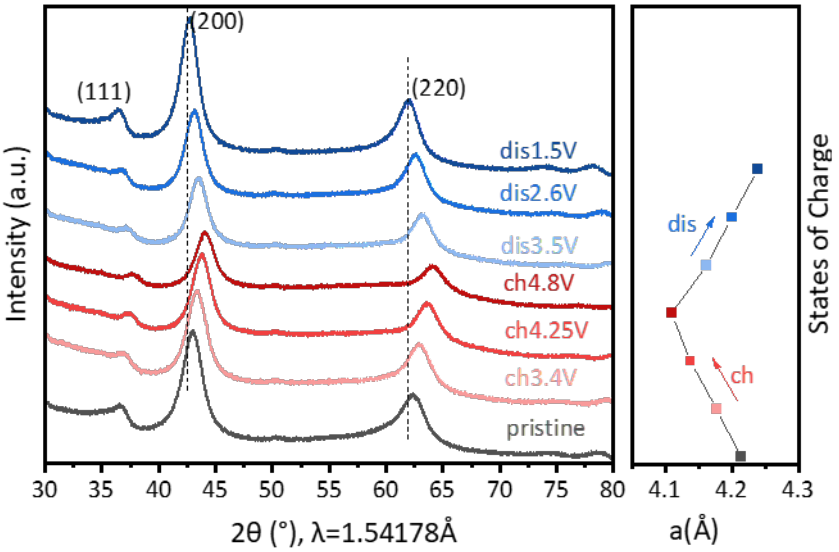

Figure 4.9: *Ex-situ* XRD patterns of LMWOF collected at key SOCs during the first cycle. Refined unit cell parameters are annotated for each state, indicating the reversible lattice contraction and expansion upon (de)lithiation.

solution behavior rather than a phase transition, further supporting the structural robustness of LMWOF during electrochemical cycling.

To probe the short-range structural features of pristine LMWOF, both *ex-situ* XPDF and EXAFS analyses were carried out. The XPDF refinement results, shown in **Figure 4.10(a–b)**, reveal that a structural model combining a DRX matrix with spinel-type local ordering (R_{wp}= 0.23) provides a significantly better fit in the low-*r* region than a pure DRX model (R_{wp}= 0.44). The refinement results for both models are summarized in **Table S4.4**. Notably, the combined model successfully reproduces the peak at ~3.7 Å, which the DRX-

only model fails to capture. This peak corresponds to the interatomic distance between cations located in an octahedral site and a neighboring tetrahedral site, thereby supporting the presence of local tetrahedral coordination.

The proposed spinel-type structure is illustrated schematically in **Figure 4.10(d)**. In this model, Li and W occupy the tetrahedral 8*a* sites, while Mn and Li reside in the octahedral 16*d* sites, consistent with the nominal formula $(Li_xW_{1-x})(Mn_{1-y}Li_y)_2O_4$. The presence of this short-range spinel-like motif embedded within the DRX matrix provides a structural rationale for the unique electrochemical behavior of LMWOF.

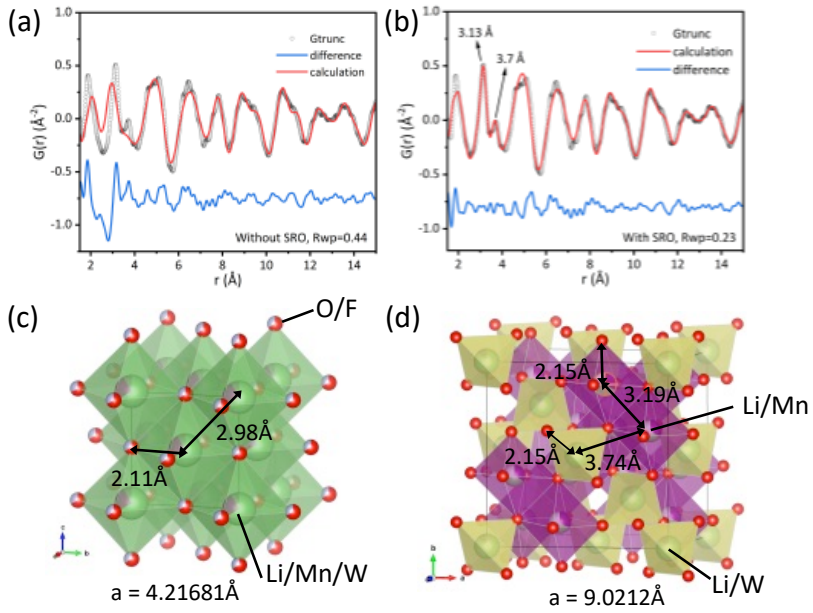

Figure 4.10: XPDF analysis of the pristine LMWOF. (a) Fitting using a pure DRX model, showing poor agreement in the low-r region (R_{wp}= 0.44). (b) Fitting using a combined DRX and $(Li_xW_{1-x})(Mn_{1-y}Li_y)_2O_4$ spinel model, significantly improving the fit in the short-range region (R_{wp}= 0.23), especially around 3.7 Å. (c) Structural model of the DRX phase. (d) Local spinel environment with tetrahedral (8*a*) sites occupied by Li and W, and octahedral (16*d*) sites by Li and Mn.

Although X-rays have limited sensitivity to light elements such as Li, the XPDF refinements were carried out with Li allowed to occupy both the 8*a* and 16*d* sites with

freely refined occupancies. Despite the uncertainty regarding Li distribution, the refinement clearly indicates that W preferentially occupies the tetrahedral 8*a* sites, and Mn is mainly located at the octahedral 16*d* sites. All alternative configurations resulted in significantly poorer fits or conflicted with independent EXAFS data discussed later.

Importantly, this spinel-type SRO observed in LMWOF is absent in the analogue LMOF, as shown in **Figure 4.11** and **Table 4.2**. In that case, using only the DRX model provides an excellent fit across the full range, with no significant local structural evolution observed during cycling.

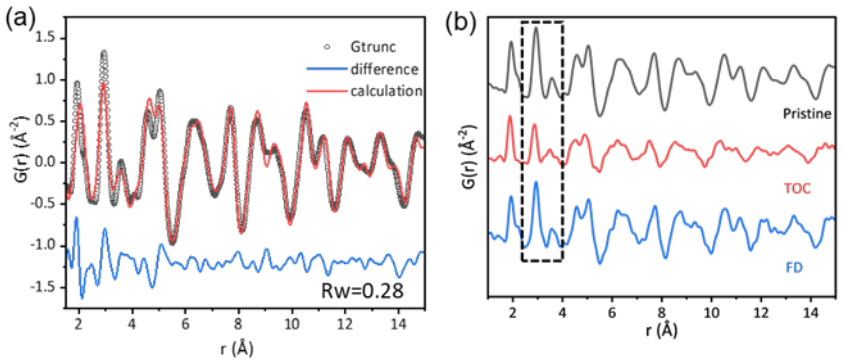

Figure 4.11: (a) XPDF refinement of pristine LMOF using only a DRX model shows a good fit across the measured range; (b) Comparison of low-*r* peaks at key SOCs (Pristine, TOC, FD) shows no significant changes during cycling.

Table 4.2: Structural parameters of pristine LMOF from the fit of XPDF data.

Pristine $R_w = 0.280$	Atom Occupancies		Isotropic temperature factors		Lattice parameter	Particle diameter
DRX ($Fm\bar{3}m$)	4*a*	4*b*	4*a*	4*b*	4.13505(0.0066)	27.7734(5)
	Li: 0.67	O: 0.67	0.0366323 (0.0086)	0.00970483 (0.0025)		
	Mn: 0.33	F: 0.33				

In contrast, for LMWOF, a notable evolution of local structure is observed during electrochemical cycling. As highlighted in **Figure 4.12(a)**, the relative intensities of low-r peaks change with state of charge, indicating dynamic rearrangement of local atomic environments. Occupancy analysis, as summarized in **Figure 4.12(b–c)**, reveals that the W

occupancy at the spinel 8*a* sites increased from 12% in the pristine state to 19% at the TOC, corresponding to a 58% relative increase. This implies that a fraction of W migrates from octahedral DRX sites to tetrahedral spinel sites during delithiation. By the end of discharge, the W occupancy in the spinel 8*a* sites decreases back to 13%, indicating that this migration is largely reversible.

In parallel, Mn occupancy at the 16*d* sites significantly decreases during charge. This is likely due to Mn migration into the DRX 4*a* sites, which become vacant as Li is extracted. Such cation rearrangement contributes to the local structural evolution and potentially affects Li diffusion and redox kinetics.

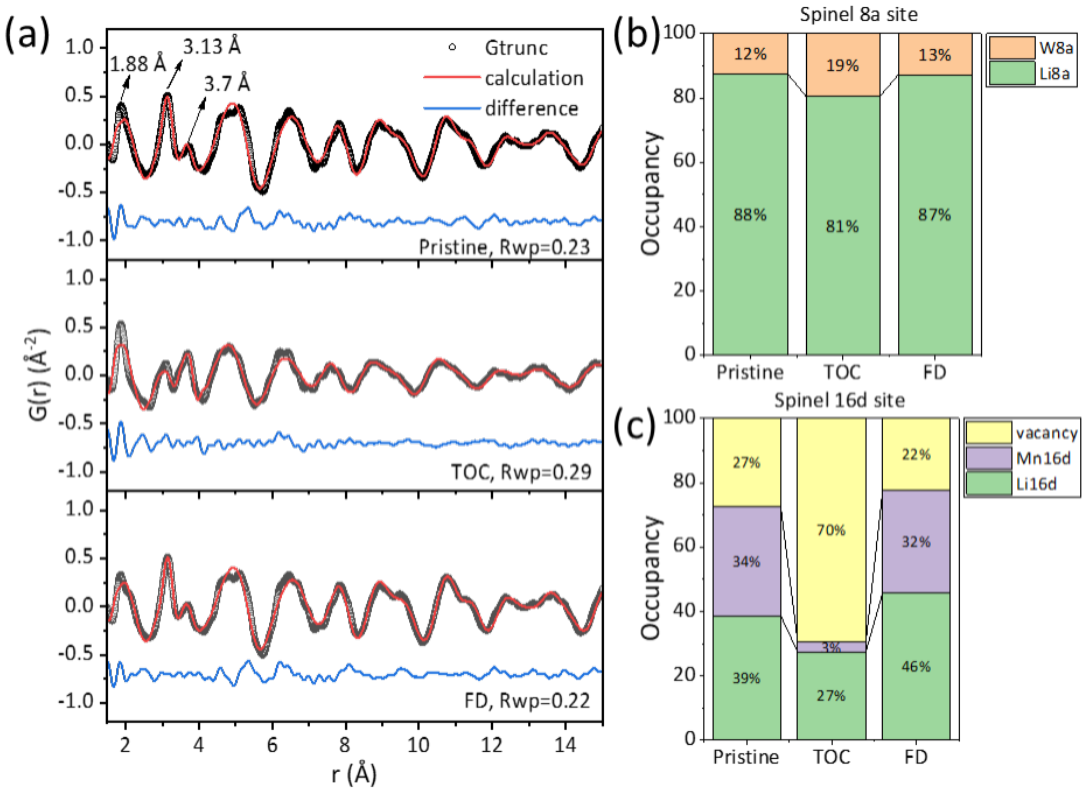

Figure 4.12: (a) XPDF refinement of LMWOF at key SOCs: Pristine, TOC, and FD; (b-c) Occupancy distribution of the (b) 8*a* and (c) 16*d* sites in the spinel structure of LMWOF at key SOCs.

The evolution of short-range structure in LMWOF was further investigated using

phase-corrected Mn K-edge and W L_3-edge EXAFS, as shown in **Figure 4.13**. Upon charging, the first peak in the Mn EXAFS, attributed to the Mn-O bond, shifts to lower R and increases in intensity. This indicates a contraction of the Mn-O bond due to Mn oxidation and reduced local disorder following Li extraction. In contrast, the first-shell peak of the W L_3-edge EXAFS, attributed to the W-O bond, remains nearly unchanged, confirming that $W^{6+}$is redox-inactive, in agreement with XANES data.

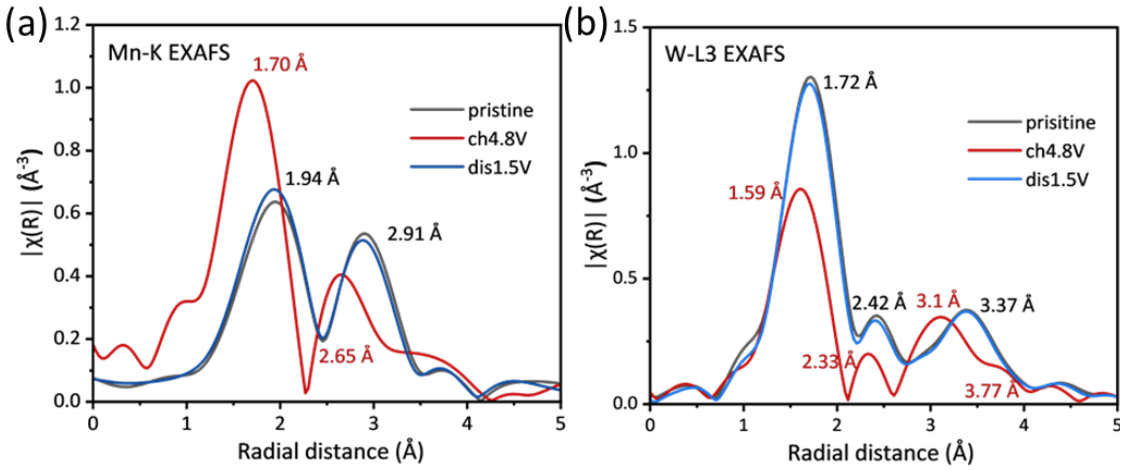

Figure 4.13: Phase-corrected (a) Mn K-edge and (b) W L_3-edge EXAFS spectra of LMWOF during the first cycle, showing bond distance evolution with SOCs.

However, at the higher R region, the W L_3-edge EXAFS exhibits a peak splitting into two components at approximately 3.1 Å and 3.77 Å. These values match 16*d*–16*d* and 8*a*–16*d* bond distances in the spinel structure, as revealed by XPDF analysis. The findings support the presence of W at the tetrahedral 8*a* sites rather than Mn. EXAFS pathway fitting (**Figure 4.14**) further confirms this by demonstrating increased contributions from W_{tet}-Mn and W_{tet}-O interatomic distances upon charging. These results align with XPDF findings, which indicate increased W occupancy at 8*a* sites at the TOC. Due to phase shifts, the apparent R values in EXAFS fitting are ~0.5 Å shorter than the actual interatomic distances.

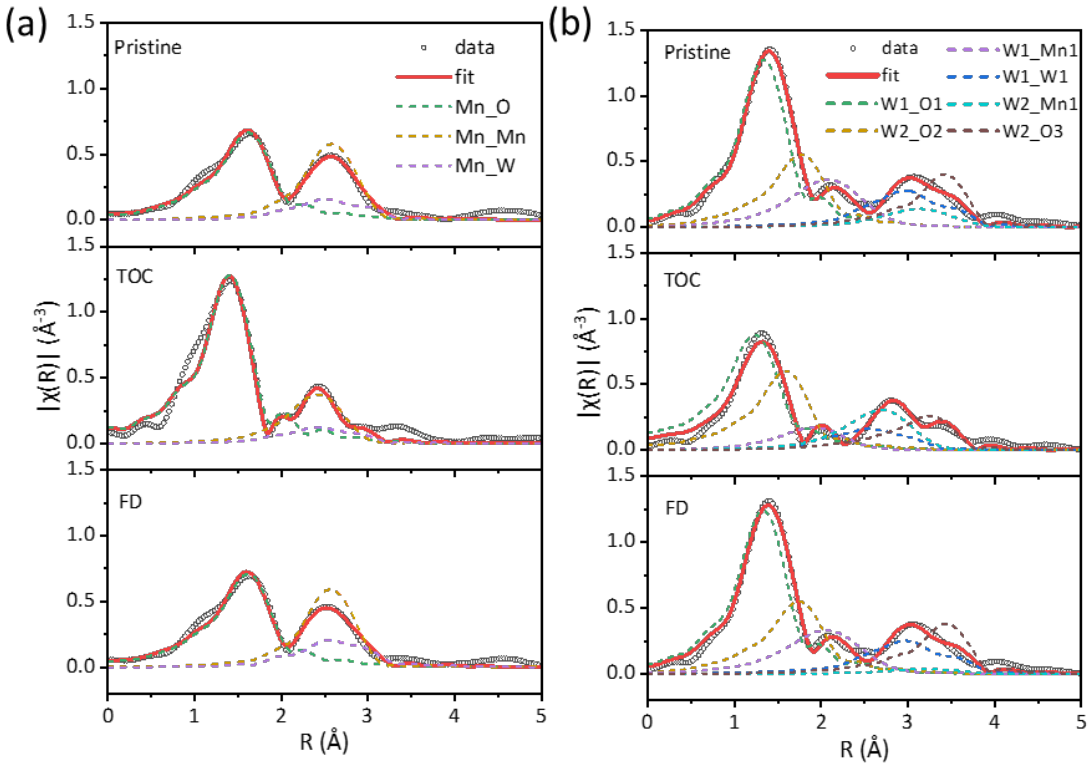

Figure 4.14: (a) Mn K-edge and (b) W L_3-edge EXAFS fitting of LMWOF at key states during the first cycle using the model generated by XPDF refinement. The phase shift is ~0.5 Å.

A schematic structure model of LMWOF is shown in **Figure 4.15**. The overall structure adopts a DRX framework ($Fm\bar{3}m$), within which spinel-like domains ($Fd\bar{3}m$) are

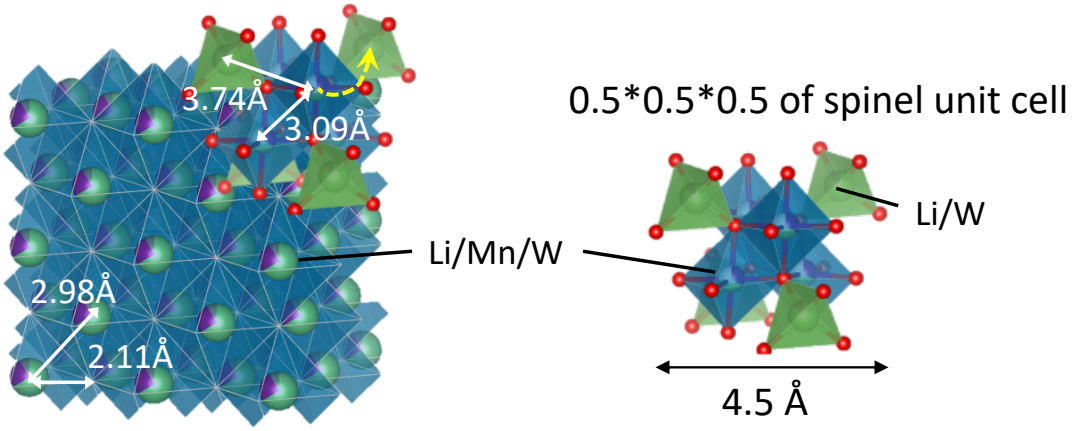

Figure 4.15: Schematic illustration of the LMWOF structure, which features a DRX matrix containing embedded spinel-like domains.

embedded. The local structure evolves through the migration of W^{6+} ions from octahedral 4*a* sites in the DRX lattice to tetrahedral 8*a* sites within spinel regions, forming Frenkel-type defects. This migration becomes more pronounced at the TOC, consistent with both EXAFS and XPDF observations.

4.2.5 Monte Carlo Simulation

To further assess the impact of W^{6+} migration on electrochemical performance, specifically regarding in Li-ion transport, Monte Carlo simulations were conducted using the Dribble package.[24] The simulations evaluated the accessibility of Li^+ and percolation pathways within supercells of LMWOF (with spinel domains) compared with LMOF (without spinel domains).

Accessible Sites:

Even in percolating structures, not all Li sites are connected to the diffusion network. Dribble quantifies the fraction of inaccessible (isolated) Li sites. The input file for LMWOF is given in **Figure S4.3**. In the structure file, the initial occupancies of octahedral and tetrahedral sites were the variables for the simulation. The fully disordered DRX structure for LMOF allows a straightforward configuration, as shown in **Table 4.3**.

Table 4.3: The initial site occupancies of the input file for LMOF used for the Monte Carlo simulation to assess the inaccessible Li sites.

Initial Occupancies in LMOF	
tetrahedral sites	Vac: 1
Octahedral sites	TM/Li: 1

For LMWOF, refined as $Li_{0.672}Mn_{0.244}W_{0.084}O_{0.68}F_{0.32}$, there is 0.084 W per formula

unit. While the W distribution derived from XPDF analysis was 0.0714 in DRX 4*a* sites and 0.1189 in spinel 8*a* sites. Due to the different unit cell sizes between DRX and spinel phase, normalization must be performed based on the anion sites, setting the unit FCC box having 32 octahedral anion sites. For the cation sites, there are 32 octahedral sites and 64 tetrahedral sites. The DRX structure has 32*a* and 32*b* sites (2*2*2) and the spinel structure has 8*a*, 16*d*, and 32*e* sites (1*1*1). For the unit FCC box, if it has an *x* ratio of spinel domains, the amount of W migrated from DRX to spinel is calculated as below:

$$32 \times (0.084-0.0714) = x \times 8 \times 0.1189$$

$$x = 0.4239$$

The initial occupancies in LMWOF can then be derived from the calculated *x* value, as shown in **Table 4.4**.

Table 4.4: The initial occupancies of the input file for LMWOF used for the Monte Carlo simulation to determine the inaccessible Li sites.

Initial Occupancies of LMWOF	
tetrahedral sites	Vac: 0.9937 = 1−0.4239×0.1189×8/64
octahedral sites	TM/Li: 0.9874 = 1−0.0126

Figure 4.16 shows the simulation results for inaccessible Li^+ across different Li occupancies, corresponding to different SOCs. At the pristine state (~0.67 Li occupancy), LMWOF exhibited 14.4% inaccessible Li sites, compared to 12.6% in LMOF. The gap widened at lower occupancies, suggesting that spinel domains in LMWOF introduces greater local constraints on Li percolation and could impact rate performance.

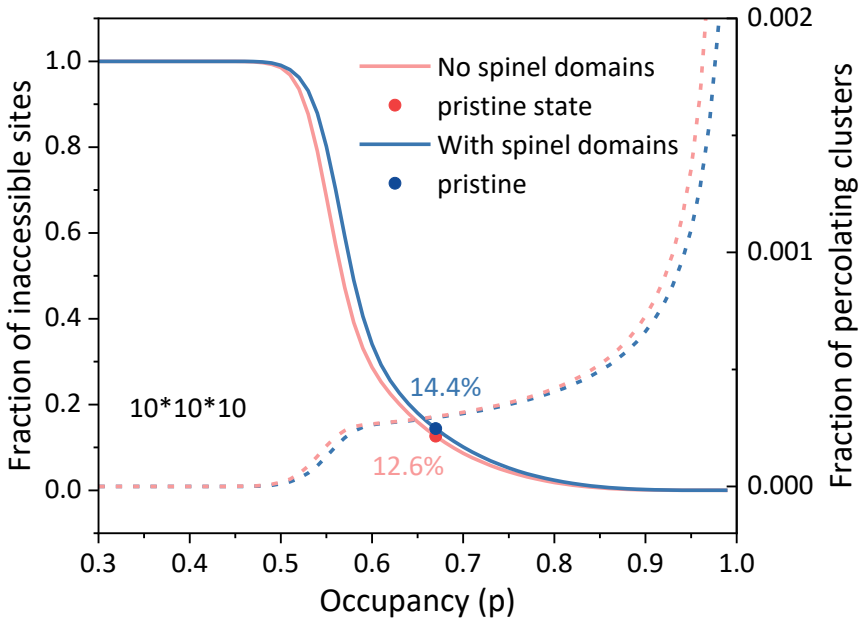

Figure 4.16: Results of the Monte Carlo simulation of Li^+ transport in LMWOF (with spinel domains) and LMOF (without spinel domains) 10×10×10 supercells. Dashed lines show the fraction of percolating Li clusters and the solid lines show the proportion of inaccessible Li sites. LMWOF exhibits more constrained Li accessibility due to the partial occupation of tetrahedral sites by W.

Tortuosity:

Tortuosity τ quantifies how much Li^+ diffusion paths deviate from a straight line in a percolating structure. It is defined as:

$$\tau = \frac{L}{D} \tag{4.1}$$

where L is the actual diffusion path length between two periodic images of the same site, and D is the direct distance between them. A tortuosity value of 1 represents an ideal straight path, while larger values indicate more tortuous (less efficient) diffusion.

In the case of DRXs, tortuosity is closely tied to Li-ion transport kinetics and thus affects rate capability. Using Dribble, tortuosity simulations were performed based on the same structure inputs described previously (**Figure S4.3**).

As shown in **Figure 4.17**, tortuosity increased as Li content decreased, indicating more constrained pathways upon delithiation. Across all Li occupancies, LMWOF exhibited

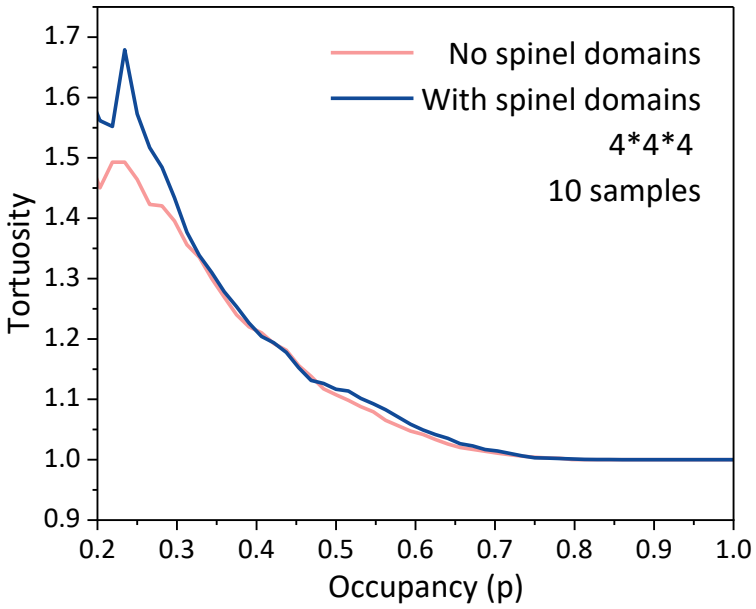

Figure 4.17: Simulated tortuosity of Li^+ diffusion as a function of Li site occupancy in LMWOF (with spinel domains) and LMOF (without spinel domains), using a 4*4*4 supercell and 10 Monte Carlo samples per data point. LMWOF shows higher tortuosity across all states, consistent with hindered Li transport.

consistently higher tortuosity than LMOF, especially at low Li occupancy (high state of charge). This aligns with the inferior rate performance observed for LMWOF.

Monte Carlo simulations were employed to compare the Li^+ site accessibility and diffusion tortuosity between LMWOF and LMOF based on site-percolation rules. The results reveal that a key structural feature of LMWOF, the partial occupation of tetrahedral sites by W^{6+}, significantly disrupts the percolating Li diffusion network by blocking critical hopping pathways. As illustrated in **Figure 4.18**, W^{6+} occupancy at tetrahedral sites interrupts the O_h–T_d–O_h diffusion channels, increasing the number of inaccessible Li sites and thereby enhancing the overall tortuosity of Li^+ transport pathways.

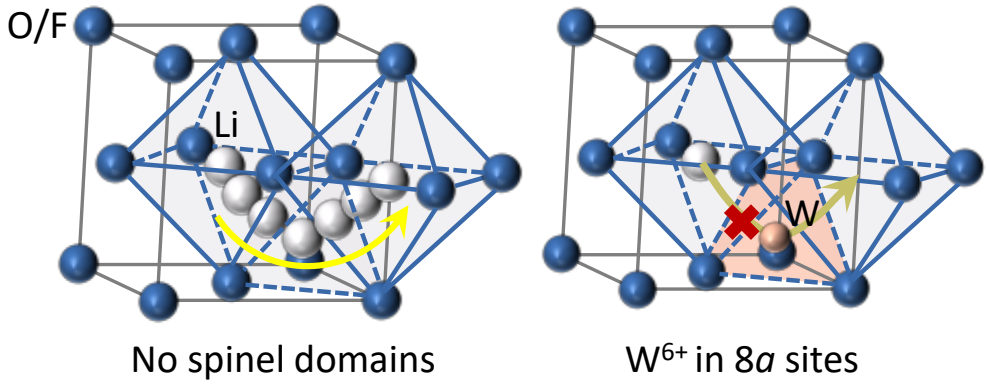

Figure 4.18: Schematic illustration of Li^+ hopping between neighbouring octahedral sites with and without W^{6+} occupying the intermediate tetrahedral sites. W^{6+} occupation blocks the O_h–T_d–O_h pathways, hindering Li percolation.

This disruption provides a mechanistic explanation for the reduced Li-ion mobility observed experimentally in LMWOF compared to LMOF. While the incorporation of W^{6+} expands the TM redox reservoir and stabilizes the structure, it simultaneously introduces kinetic limitations by hindering Li percolation. These findings highlight an intrinsic trade-off in DRX systems between improving redox stability and maintaining efficient Li-ion transport, emphasizing the importance of carefully optimizing cation distribution and site occupancy.

4.4 Conclusion

This chapter systematically investigated the influence of high-valent d^0 cations, specifically W^{6+}, on the electrochemical behavior and structural evolution of Mn-based DRX oxyfluoride cathodes. The combined spectroscopic, structural, and Monte Carlo results show that W^{6+} substitution improves redox stability by stabilizing cationic Mn redox and suppressing irreversible oxygen release or dimerization, but at the same time introduces local structural features that hinder Li percolation and reduce rate capability.

Spectroscopic analyses confirmed the activation of multi-electron Mn redox processes and the formation of electron holes on lattice oxygen during charging in LMWOF. No evidence of irreversible oxygen release or dimerization was observed. The stabilization of electron holes contributed to improved cycling stability compared with LMOF. Structural studies further revealed that in LMWOF, W^{6+} migrates from DRX octahedral sites to spinel tetrahedral sites, resulting in the formation of local Frenkel-type defects. This leads to the existence of spinel-type domains embedded within the DRX matrix, which is unique to LMWOF. The presence of tetrahedral W^{6+} sites disrupts percolation pathways and increases diffusion tortuosity, which aligns with both the observed reduced rate performance and the results of Monte Carlo modelling.

More importantly, this study provides a broader conceptual advance for the understanding of d^0-metal substitution in DRX cathodes. In the literature, high-valent d^0 cations such as Ti^{4+}, Nb^{5+}, Mo^{6+}, and W^{6+} are often introduced primarily to stabilize the lattice by accommodating local octahedral distortions and mitigating TM migration.[38-43] In contrast, the present results show that their role extends beyond passive structural stabilization. Through the site preference, local coordination effects, and strong electrostatic interactions, these cations can actively reshape defect chemistry and Li-ion transport topology. This provides a new perspective on how d^0 metals influence the balance between redox chemistry, structural robustness, and transport kinetics in DRX systems.

From a materials-design perspective, these findings suggest that d^0 cations should be selected not only for their ability to stabilize the framework, but also for how they modify local migration pathways and percolation networks. Future design of DRX cathodes should

therefore aim to optimize both the identity and concentration of inactive high-valent cations to maximize reversible redox capacity while minimizing kinetic penalties. This perspective may be broadly relevant for the development of next-generation high-energy DRX cathodes with improved cycling stability and practical rate performance.

4.5 Appendix

Table S4.1: Oxidation state for Mn in as-prepared LMWOF measured via Iodometric Titration.

	Mass of sample (mg)	Volume of $Na_2S_2O_3$ (μL, 0.01M)	Mn valence state (average)
1	13.1	491.517	
2	14.8	530.377	
3	14.4	491.495	2.0749
4	16.9	603.961	
5	16.0	600.391	

Table S4.2: The F mass fraction in as-prepared LMWOF obtained from F^--Ion Selective Electrode.

	Mass of sample (mg)	Before addition (mV)	After addition (mV)	F mass fraction (average)
1	7.4	57.7	47.9	
2	5.3	65.1	53.1	
3	6.8	59.1	49.1	0.121134
4	6.2	62.0	51.2	
5	7.6	56.3	47.5	

$$C_{sample} = Q \times C_{standard}$$

$$C_{standard} = 100 \text{ mg/L}$$

$$Q = \frac{p}{\left[(1+p)10^{\frac{\Delta E}{S}}\right]-1}$$

$p = 1/75$ (volume of standard / volume of sample)

S = 58.1 mV (slope of the electrode)

Table S4.3: Target and measured composition of LMWOF.

Target	$Li_2Mn_{0.75}W_{0.25}O_2F$
Measured	$Li_{2.017}Mn_{0.731}W_{0.252}O_{2.041}F_{0.953}$

The atomic ratio between Li, Mn and W was determined by ICP-OES. By combining the measured F mass fraction and the valence state of Mn, the content of O and F was calculated.

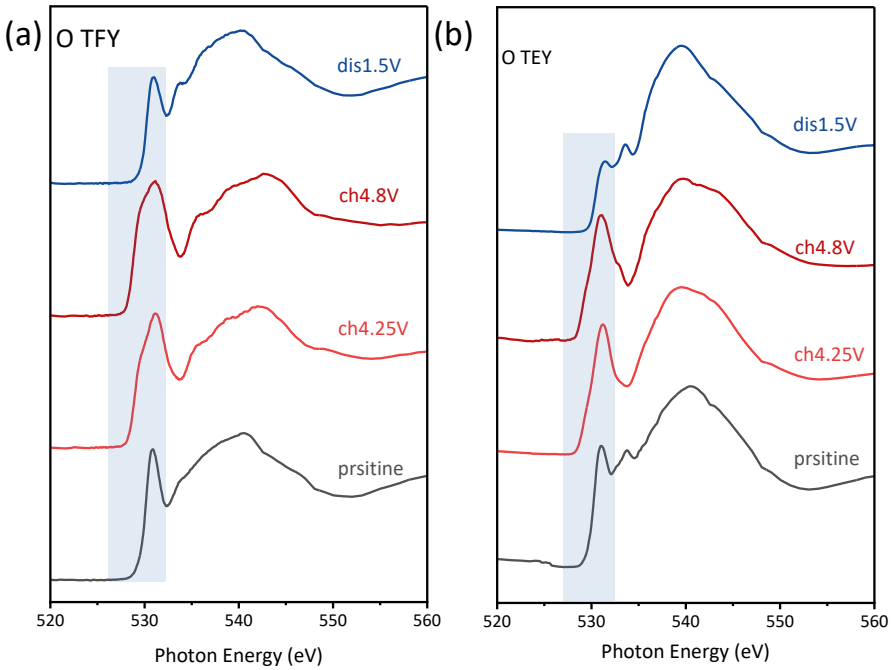

Figure S4.1 :O K-edge spectra of LMWOF during the first cycle obtained in (a) TFY and (b) TEY detection modes.

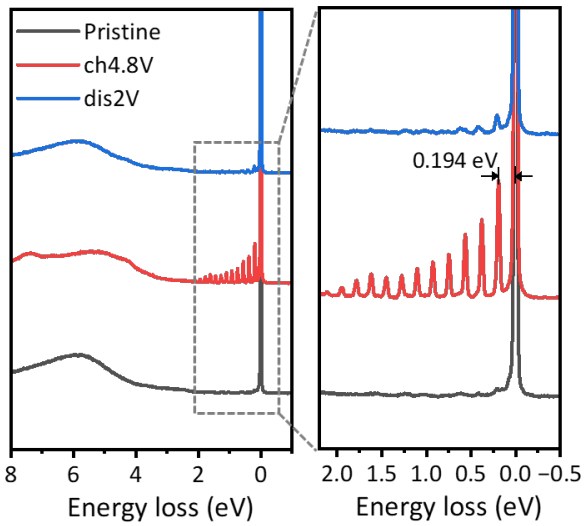

Figure S4.2: O K-edge RIXS spectra of LMOF at different SOCs. The zoomed-in TOC spectrum shows the vibrational progression peaks with an initial peak spacing of 0.194 eV.

Table S4.4: XPDF refinement results of LMWOF using either a pure DRX model or a combined model at selected SOCs.

Pristine R_w = 0.472	Atom Occupancies		Anisotropic temperature factors		Lattice parameter	Particle diameter
DRX ($Fm\bar{3}m$)	4*a*	4*b*	4*a*	4*b*	4.21968(0.019)	38.4971(27)
	Li: 0.672	O: 0.68	0.0373533 (0.016)	0.0460165 (0.031)		
	Mn: 0.244	F: 0.318				
	W: 0.084					

Pristine R_w = 0.240	Atom Occupancies			Isotropic temperature factors			Lattice parameter	Particle diameter
DRX ($Fm\bar{3}m$)	4*a*		4*b*	4*a*		4*b*	4.21671(0.02)	30.761(15)
	Li: 0.672		O: 0.68	0.0379511 (0.017)		0.0616882 (0.039)		
	Mn: 0.2033		F: 0.318					
	W: 0.0714							
Spinel ($Fd\bar{3}m$)	8*a*	16*d*	32*e*	8*a*	16*d*	32*e*	9.01642(0.22)	4.2073 (0.46)
	Li: 0.881134 (5.9e+05)	Mn: 0.354908 (1.8e+06)	O:1.04654 (3.8e+06)	0.0115871 (0.04)	0.00838616 (0.012)	0.371433 (0.25)		
	W: 0.118866 (5.9e+05)	Li: 0.384485 (9e+06)						

TOC R_w = 0.296	Atom Occupancies			Isotropic temperature factors			Lattice parameter	Particle diameter
DRX ($Fm\bar{3}m$)	4*a*		4*b*	4*a*		4*b*	4.13019(0.034)	24.5969(11)
	Li: 0.475367 (2.2e+07)		O: 0.68	0.0598299 (0.049)		0.0418955 (0.079)		
	Mn: 0.383161 (3.2e+07)		F: 0.318					
	W: 0.141472 (9.8e+06)							
Spinel ($Fd\bar{3}m$)	8*a*	16*d*	32*e*	8*a*	16*d*	32*e*	8.86736(0.41)	4.17708 (0.36)
	Li: 0.412189 (9.7e+06)	Mn: 0.0837146 (1.1e+06)	O: 0.999165 (0.091)	0.00449133 (0.026)	0.0144188 (0.024)	0.389969 (0.18)		
	W: 0.163121 (3.9e+05)	Li: 0.463276 (9.3e+06)						

<table>
<tr><td rowspan="2">FD
R_w= 0.216</td><td colspan="3">Atom Occupancies</td><td colspan="3">Isotropic temperature factors</td><td>Lattice parameter</td><td>Particle diameter</td></tr>
<tr><td colspan="2">4a</td><td>4b</td><td colspan="2">4a</td><td>4b</td><td rowspan="4">4.22914(0.019)</td><td rowspan="4">37.4112(21)</td></tr>
<tr><td rowspan="3">DRX
($Fm\bar{3}m$)</td><td colspan="2">Li: 0.586815 (2.7e+06)</td><td>O: 0.68</td><td colspan="2" rowspan="3">0.0421206
(0.02)</td><td rowspan="3">0.0467295
(0.041)</td></tr>
<tr><td colspan="2">Mn: 0.312088 (3.9e+06)</td><td rowspan="2">F: 0.318</td></tr>
<tr><td colspan="2">W: 0.101098 (1.2e+06)</td></tr>
<tr><td rowspan="3">Spinel
($Fd\bar{3}m$)</td><td>8a</td><td>16d</td><td>32e</td><td>8a</td><td>16d</td><td>32e</td><td rowspan="3">9.02742 (0.16)</td><td rowspan="3">4.23533
(0.39)</td></tr>
<tr><td>Li:
0.877112
(0.038)</td><td>Mn:
0.288889
(0.13)</td><td rowspan="2">O:1.03469
(0.24)</td><td rowspan="2">0.017545
6 (0.03)</td><td rowspan="2">0.007167
21
(0.0066)</td><td rowspan="2">0.370499
(0.099)</td></tr>
<tr><td>W:
0.122888
(0.038)</td><td>Li:
0.413851
(1.5)</td></tr>
</table>

```
{
    "structure": "LiMO2+tet-rotated.vasp",
    "formula_units": 1,
    "cutoff": 2.0,
    "sublattices": {
        "tet": {
            "description": "tetrahedral site",
            "sites": [3, 4, 5, 6],
            "initial_occupancy": {"Vac": 0.9937, "W":0.0063},
            "site_rules": [
                ["NeighborShellSR",
                 {"stable_nb_shells": [[
                     {"oct": [{"min": 4, "species": ["Li"]}]}
                   ]]
                 }
                ]
            ]
        },
        "oct": {
            "description": "octahedral site",
            "sites": [1, 2],
            "initial_occupancy": {"TM": 0.9874, "Vac": 0.0126}
        },
        "oxygen": {
            "description": "oxygen sites",
            "sites": {"species": ["O"]},
            "ignore": true
        }
    },
    "bonds": [{"sublattices": ["oct", "tet"]}],
    "percolating_species": ["Li", "Vac"],
    "static_species": ["Vac", "W"],
    "flip_sequence": [["TM", "Li"]]
}
```

Figure S4.3: The input file for LMWOF used for Monte Carlo simulations to calculate the inaccessible Li sites with the highlighted variables.

4.6 References

1. R. J. Clément, Z. Lun and G. Ceder, *Energy & Environmental Science*, 2020, **13**, 345-373.

2. H. Li, R. Fong, M. Woo, H. Ahmed, D.-H. Seo, R. Malik and J. Lee, *Joule*, 2022, **6**, 53-91.

3. H. M. Hau, T. Holstun, E. Lee, B. L. D. Rinkel, T. P. Mishra, M. M. DiPrince, R. S.

Mohanakrishnan, E. C. Self, K. A. Persson, B. D. McCloskey and G. Ceder, *Advanced Materials*, 2025, 2502766.

4. J. Lee, A. Urban, X. Li, D. Su, G. Hautier and G. Ceder, *Science*, 2014, **343(6170)**, 519-522.

5. D. Chen, J. Ahn and G. Chen, *ACS Energy Letters*, 2021, **6(4)**, 1358-1376.

6. T. Li, T. S. Geraci, K. P. Koirala, A. Zohar, E. N. Bassey, P. A. Chater, C. Wang, A. Navrotsky and R. J. Clément, *Journal of the American Chemical Society*, 2024, **146**, 24296-24309.

7. H. Song, W. Xie, Y. Tian, M. Guo, T. Wang, D. Kang, M. Jia and X. Zhang, *Journal of Materials Chemistry A*, 2024, **12**, 15154-15162.

8. A. Urban, A. Abdellahi, S. Dacek, N. Artrith and G. Ceder, *Physical Review Letters*, 2017, **119**, 176402.

9. A. Urban, J. Lee and G. Ceder, *Advanced Energy Materials*, 2014, **4(13)**, 1400478.

10. D. H. Kwon, J. Lee, N. Artrith, H. Kim, L. Wu, Z. Lun, Y. Tian, Y. Zhu and G. Ceder, *Cell Reports Physical Science*, 2020, **1**, 100187.

11. L. Huang, P. Zhong, Y. Ha, Z. Cai, Y. W. Byeon, T. Y. Huang, Y. Sun, F. Xie, H. M. Hau, H. Kim, M. Balasubramanian, B. D. McCloskey, W. Yang and G. Ceder, *Advanced Energy Materials*, 2023, **13**, 2202345.

12. Z. Lun, B. Ouyang, D. A. Kitchaev, R. J. Clément, J. K. Papp, M. Balasubramanian, Y. Tian, T. Lei, T. Shi, B. D. McCloskey, J. Lee and G. Ceder, *Advanced Energy Materials*, 2019, **9**, 1802959.

13. S. Ren, R. Chen, E. Maawad, O. Dolotko, A. A. Guda, V. Shapovalov, D. Wang, H. Hahn and M. Fichtner, *Advanced Science*, 2015, **2**, 1500128.

14. J. Lee, D. A. Kitchaev, D. H. Kwon, C. W. Lee, J. K. Papp, Y. S. Liu, Z. Lun, R. J. Clement, T. Shi, B. D. McCloskey, J. Guo, M. Balasubramanian and G. Ceder, *Nature*, 2018, **556**, 185-190.

15. D. A. Kitchaev, Z. Lun, W. D. Richards, H. Ji, R. J. Clément, M. Balasubramanian, D. H. Kwon, K. Dai, J. K. Papp, T. Lei, B. D. McCloskey, W. Yang, J. Lee and G. Ceder, *Energy & Environmental Science*, 2018, **11**, 2159-2171.

16. J. Lee, J. K. Papp, R. J. Clément, S. Sallis, D. H. Kwon, T. Shi, W. Yang, B. D. McCloskey and G. Ceder, *Nature Communications*, 2017, **8**, 981.

17. H. M. Hau, T. Mishra, C. Ophus, T. Y. Huang, K. Bustilo, Y. Sun, X. Yang, T. Holstun, X. Zhao, S. Wang, Y. Ha, G. H. Lee, C. Song, J. Turner, J. Bai, L. Ma, K. Chen, F.

Wang, W. Yang, B. D. McCloskey, Z. Cai and G. Ceder, *Nature Nanotechnology*, 2024, **19**, 1831-1839.

18. Y. Wang, W. Choe, Y. Ding, R. Liu, D. Nordlund and D. Chen, *Journal of the American Chemical Society*, 2025, **147**, 13437-13446.

19. R. A. House, L. Jin, U. Maitra, K. Tsuruta, J. W. Somerville, D. P. Förstermann, F. Massel, L. Duda, M. R. Roberts and P. G. Bruce, *Energy & Environmental Science*, 2018, **11**, 926-932.

20. R. Sharpe, R. A. House, M. J. Clarke, D. Forstermann, J. J. Marie, G. Cibin, K. J. Zhou, H. Y. Playford, P. G. Bruce and M. S. Islam, *Journal of the American Chemical Society*, 2020, **142**, 21799-21809.

21. B. H. Toby and R. B. Von Dreele, *Journal of Applied Crystallography*, 2013, **46**, 544-549.

22. C. Farrow, P. Juhas, J. Liu, D. Bryndin, E. Božin, J. Bloch, T. Proffen and S. Billinge, *Journal of Physics: Condensed Matter*, 2007, **19**, 335219.

23. C. Schulz, K. Lieutenant, J. Xiao, T. Hofmann, D. Wong and K. Habicht, *Synchrotron Radiation*, 2020, **27**, 238-249.

24. A. Urban, in *Computational Design of Battery Materials*, Springer, 2024, 169-185.

25. X. Xu, L. Pi, J. J. Marie, G. J. Rees, C. Gong, S. Pu, R. A. House, A. W. Robertson and P. G. Bruce, *Journal of the Electrochemical Society*, 2021, **168**, 080521.

26. R. Chen, S. Ren, M. Knapp, D. Wang, R. Witter, M. Fichtner and H. Hahn, *Advanced Energy Materials*, 2015, **5**, 1401814.

27. R. Chen, S. Ren, M. Yavuz, A. A. Guda, V. Shapovalov, R. Witter, M. Fichtner and H. Hahn, *Physical Chemistry Chemical Physics*, 2015, **17**, 17288-17295.

28. H. Ahmed, M. Woo, N. Dumaresq, P. Trevino Lara, R. Fong, S. J. Lee, G. Lazaris, N. Mubarak, N. Brodusch, D. H. Seo, R. Gauvin, G. P. Demopoulos and J. Lee, *Nature Communications*, 2025, **16**, 5806.

29. A. J. Berry, G. M. Yaxley, A. B. Woodland and G. J. Foran, *Chemical Geology*, 2010, **278**, 31-37.

30. R. A. Ahmed, K. P. Koirala, G. H. Lee, T. Li, Q. Zhao, Y. Fu, L. Zhong, J. D. Daddona, M. Zuba and C. Siu, *Advanced Energy Materials*, 2024, **14**, 2400722.

31. F. de Groot, *Chemical Reviews*, 2001, **101**, 1779-1808.

32. R. A. House, U. Maitra, M. A. Perez-Osorio, J. G. Lozano, L. Jin, J. W. Somerville, L. C. Duda, A. Nag, A. Walters, K. J. Zhou, M. R. Roberts and P. G. Bruce, *Nature*,

2020, **577**, 502-508.

33. J. J. Marie, M. Jenkins, J. Chen, G. Rees, V. Cellorio, J. Choi, S. Agrestini, M. Garcia-Fernandez, K. J. Zhou, R. A. House and P. G. Bruce, *Advanced Energy Materials*, 2024, **14**, 2401935.

34. R. Qiao, Y. D. Chuang, S. Yan and W. Yang, *Plos One*, 2012, **7**, e49182.

35. R. A. House, G. J. Rees, M. A. Pérez-Osorio, J. J. Marie, E. Boivin, A. W. Robertson, A. Nag, M. Garcia-Fernandez, K. J. Zhou and P. G. Bruce, *Nature Energy*, 2020, **5**, 777-785.

36. D. Cao, C. Tan and Y. Chen, *Nature Communications*, 2022, **13**, 4908.

37. A. T. S. Freiberg, M. K. Roos, J. Wandt, R. de Vivie-Riedle and H. A. Gasteiger, *The Journal of Physical Chemistry A*, 2018, **122**, 8828-8839.

38. N. Yabuuchi, Y. Tahara, S. Komaba, S. Kitada and Y. Kajiya, *Chemistry of Materials*, 2016, **28**, 416-419.

39. N. Yabuuchi, M. Takeuchi, S. Komaba, S. Ichikawa, T. Ozaki and T. Inamasu, *Chemical Communications*, 2016, **52**, 2051-2054.

40. J. Lee, A. Urban, X. Li, D. Su, G. Hautier and G. Ceder, *Science*, 2014, **343**, 519-522.

41. N. Yabuuchi, M. Takeuchi, M. Nakayama, H. Shiiba, M. Ogawa, K. Nakayama, T. Ohta, D. Endo, T. Ozaki, T. Inamasu, K. Sato and S. Komaba, *Proceedings of the National Academy of Sciences of the United States of America*, 2015, **112**, 7650-7655.

42. H. Shigemura, M. Tabuchi, H. Sakaebe, H. Kobayashi and H. Kageyama, *Journal of the Electrochemical Society*, 2003, **150**, A638.

43. K. Zhou, S. Zheng, H. Liu, C. Zhang, H. Gao, M. Luo, N. Xu, Y. Xiang, X. Liu and G. Zhong, *ACS Applied Materials & Interfaces*, 2019, **11**, 45674-45682.

5

Ni-Based Disordered Rock-Salt Oxide Cathodes

Contents

5.1 Introduction

DRX cathode materials have emerged as promising candidates for next-generation high-capacity Li-ion batteries due to their compositional flexibility, robust structural frameworks, and ability to access multi-electron redox reactions.[1-3] However, a persistent challenge in DRX cathode development is the pronounced voltage hysteresis and the frequent appearance of low-voltage plateaus during discharge, which fundamentally limit their energy efficiency and practical applicability.[1, 3, 4] Several different hypotheses regarding the origin of this voltage hysteresis have been proposed in the literature, with attractions centering on TM migration and irreversible oxygen redox, including lattice oxygen loss.[5-8]

To address these open questions, this chapter systematically investigates the correlation between cation substitution, band structure, and redox chemistry in two Ni-based DRX systems: $Li_{1.2}\overset{+2}{Ni}_{0.4}\overset{+5}{Nb}_{0.4}O_2$ (LNNO) and $Li_{1.2}\overset{+2}{Ni}_{0.5}\overset{+6}{W}_{0.3}O_2$ (LNWO), which were synthesized for the first time in this thesis. Combining advanced structural characterization, comprehensive electrochemical measurements, and a suite of spectroscopic techniques, we explored how substituting high-valent d^0 cations, Nb^{5+} and W^{6+}, modifies the redox behavior, oxygen activity, and cycling stability of Ni-based DRXs. In particular, we focus on unraveling the mechanistic origin of voltage hysteresis in relation to the electronic structure and charge compensation pathways.

5.1.1 Material Design

The high theoretical capacity of Ni-based DRX cathodes originates from the

possibility of accessing multi-electron Ni^{2+}/Ni^{4+} redox although full utilization is challenging due to the competition with oxygen redox.[1] Usually in Li-rich layered or DRX materials, the pristine Ni oxidation state is often around +3, thereby limiting the available Ni redox window.[9-11] To enhance Ni-based capacity, a key design principle is to reduce Ni oxidation state in the pristine material and maintain structural integrity during cycling.

Two major strategies have been explored to achieve this goal illustrated in **Figure 5.1**:

1. Anion substitution with fluorine: Partial replacement of oxygen with fluorine reduces the overall anion charge, thus lowering the required Ni oxidation state for charge balance. The limit of this strategy is that high-content fluorination is hard to achieve via solid-state method.[12, 13] Thus, most of oxyfluorides with high F content were made by ball-milling which lacks the scale-up possibility.[9, 14, 15]

2. Cation substitution with high-valent d^0 metals: Introducing d^0 metals with oxidation state above +3 into the DRX framework compensates for charge neutrality, enabling a larger fraction of Ni to remain in the +2 state.[16-18] This is feasible by solid-state and molten-salt methods.

Building upon this rationale, we designed and investigated two Li-rich Ni-based DRX oxides with high-valent d^0 metals: $Li_{1.2}\overset{+2}{Ni}_{0.4}\overset{+5}{Nb}_{0.4}O_2$ and $Li_{1.2}\overset{+2}{Ni}_{0.5}\overset{+6}{W}_{0.3}O_2$. These materials enable a comparative study of how different high-valent d^0 substitutions influence the resulting electrochemistry and the coupling between oxygen participation and cycling stability. This material design framework establishes the foundation for the following sections, where we systematically investigate the band structures and redox mechanisms of LNNO and LNWO.

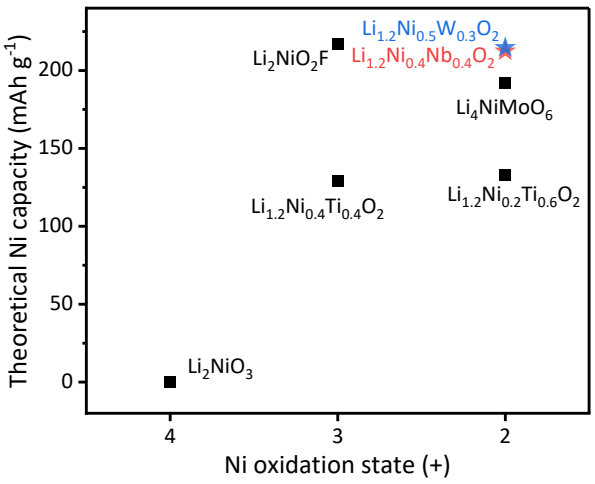

Figure 5.1: Theoretical Ni-redox capacities of various Ni-based cathode materials as a function of their pristine Ni oxidation states.

5.2 Experimental Section

5.2.1 Material Synthesis and Composition Analysis

The text originally presented here cannot be made freely available via ORA because of pending publication and commercially sensitive information.

For compositional analysis, the as-prepared powders were sent to Butterworth Laboratories for ICP-OES analysis via a mail-in service. Sample preparation (powder dissolved in hydrochloric acid) and measurements were carried out by the laboratory, while

the author performed the subsequent data analysis.

5.2.2 Electron Microscopy

SEM images and EDX mapping were collected using a Carl Zeiss Merlin field emission analytical SEM at an operating voltage of 10 keV. As prepared and pulverized powders were mounted on a stub using carbon tape.

TEM images and ED patterns were recorded by a high vacuum JEOL 3000F analytical TEM under 200 kV.

5.2.3 Structural Characterization

Synchrotron PXRD and XPDF at different SOCs were performed at I15-1 beamline of Diamond Light Source. The mixture of active material and acetylene black in 70:20 wt% were used for assembling the coin cells and cycling. The powders were collected from the disassembled cells, washed by DMC to remove the $LiPF_6$ salt and loaded into the 0.7mm silica glass capillary tubes which were sealed in the Ar-filled glovebox.

NPD was collected at D4 beamline of Institute Laue-Langevin. The mixture of active material and acetylene black in 90:10 wt% were cycled in the scale-up cells, collected and washed by DMC, then dried overnight in the vacuum chamber at 60 °C to remove residual solvent containing hydrogen, which scatters severely with neutrons. The dry powders were loaded into the ϕ5mm vanadium cans and sealed in the Ar-filled glovebox. The accumulation time for each sample was 90 min.

The diffraction data were analysed using the Rietveld method of refinement with GSAS2 software.[19] The XPDF refinement was carried out using the PDFgui software.[20]

5.2.4 Redox Mechanism Characterization

XANES and EXAFS were performed at 44A beamline of Taiwan Photon Source and B18 beamline of Diamond Light Source in transmission mode. Electrode films were sealed using the Kapton tape. sXAS spectra (including TEY, TFY, PFY, IPFY) were acquired at 11A beamline of Taiwan Light Source and BL27SU of the RIKEN/JASRI Spring8 synchrotron. The sample films were transferred with a vacuum holder to avoid air exposure.

RIXS experiments were conducted at beamline U41-PEAXIS at BESSY II, located at Helmholtz-Zentrum Berlin (HZB).[21] A vacuum suitcase was used to transfer the sample from an N_2-filled glovebox to the test chamber. The spectrometer was positioned at specular conditions relative to 60° scattering angle and was optimized to a combined resolution of 90 meV using a carbon tape. The O K-edge RIXS spectra of the samples were collected at an excitation energy of 531.0 eV. The acquisition time for each pattern was 30 min.[21]

Continuous wave EPR (CW-EPR) data were collected at X-band ~9.4 GHz at the Centre for Advanced ESR (CAESR) of the Department of Chemistry, University of Oxford. The X-band spectrometer was a Bruker EMXmicro with a Premium bridge, utilizing a Bruker ER4122SHQE-W1 resonator. Temperature was maintained with an Oxford Instruments ITC-503s temperature controller and LLT-600 transfer line controlling flow from a liquid nitrogen dewar. EPR simulations were performed with the EasySpin routines written for scripting in the MATLAB environment (The MathWorks, Inc, Natick NJ).[22]

5.2.5 Electrochemistry

The text originally presented here cannot be made freely available via ORA because

of pending publication and commercially sensitive information.

A Li-metal disk (MTI) was used as a negative electrode with two glass microfibre separators (Whatman) soaked in 140 µL of 1M $LiPF_6$ in EC: EMC = 30:70 vol% electrolyte (DodoChem). Unless specific notes, all the cells were tested at room temperature of 30 °C.

DEMS analysis was carried out to trace the different gases generated during cell cycling. The set up consisted of a quadrupole mass spectrometer (Thermo Fischer)

equipped with turbomolecular pump (Pfeiffer Vacuum) and mass-flow controllers (Bronkhorst). Two electrode type cells (ECC-Std from EL-CELL) with gas inlet and outlet ports were used for the operando measurements. The cell consisted of Li anode, electrolyte (1M $LiPF_6$ in PC) and the same cathode as described above. The cell was cycled with the current density of 20 mA/g and voltage window of 1.5-4.8V. Ultrapure Ar was used as carrier gas. The purge gas flow was 1 mL/min. Detection limits are below 1 ppm.

Unless otherwise stated, the synthesis of materials, electrochemical testing, and subsequent data analysis presented in this chapter were performed by the author. Where measurements, sample preparation, or analytical services were carried out by collaborators or external laboratories, this is explicitly stated in the relevant sections. The scientific interpretation and integration of the results were carried out by the author.

5.3 Results and Discussion

5.3.1 Structure and Electrochemistry of LNNO

Based on the material design rationale in **Figure 5.1**, Nb^{5+} was selected as a high-valent d^0 metal to lower the average Ni oxidation state and increase the fraction of electrochemically active Ni, amplifying utilization of Ni redox in LNNO. ICP-OES (**Table 5.1**) confirmed the practical composition as $Li_{1.24}Ni_{0.38}Nb_{0.38}O_2$, corresponding to an average Ni oxidation state of +2.26, assuming Nb remains +5 as intended. EDX mappings (**Figure 5.2**) exhibited homogeneous elemental distribution at micrometer level.

Table 5.1: Target and measured composition of LNNO and LNWO.

Target	$Li_{1.2}Ni_{0.4}Nb_{0.4}O_2$	$Li_{1.2}Ni_{0.5}W_{0.3}O_2$
Measured	$Li_{1.24}Ni_{0.38}Nb_{0.38}O_2$	$Li_{1.20}Ni_{0.49}W_{0.31}O_2$

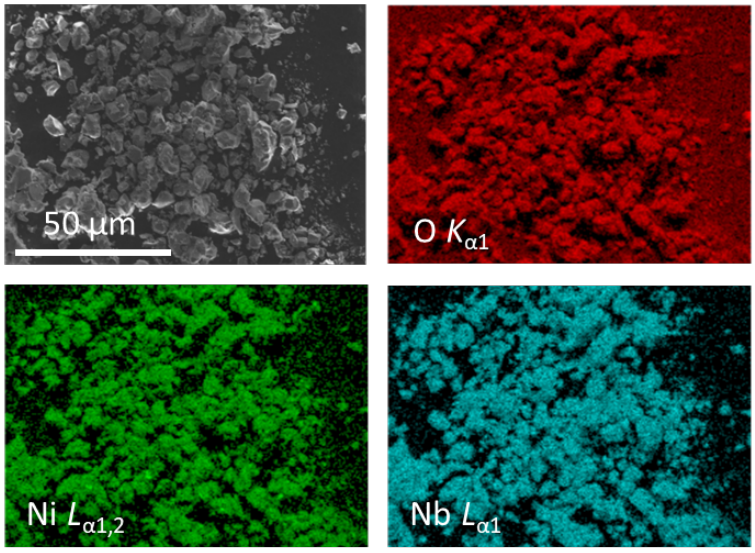

Figure 5.2: SEM image and EDX mappings of LNNO.

To confirm the formation of the targeted DRX phase and evaluate cation distribution, PXRD and PND measurements were performed. The complementary sensitivity of X-rays to Ni/Nb and neutrons to Li allowed robust structural analysis. Joint Rietveld refinement, shown in **Figure 5.3(a-b)**, confirms LNNO crystallizes in a single-phase DRX structure

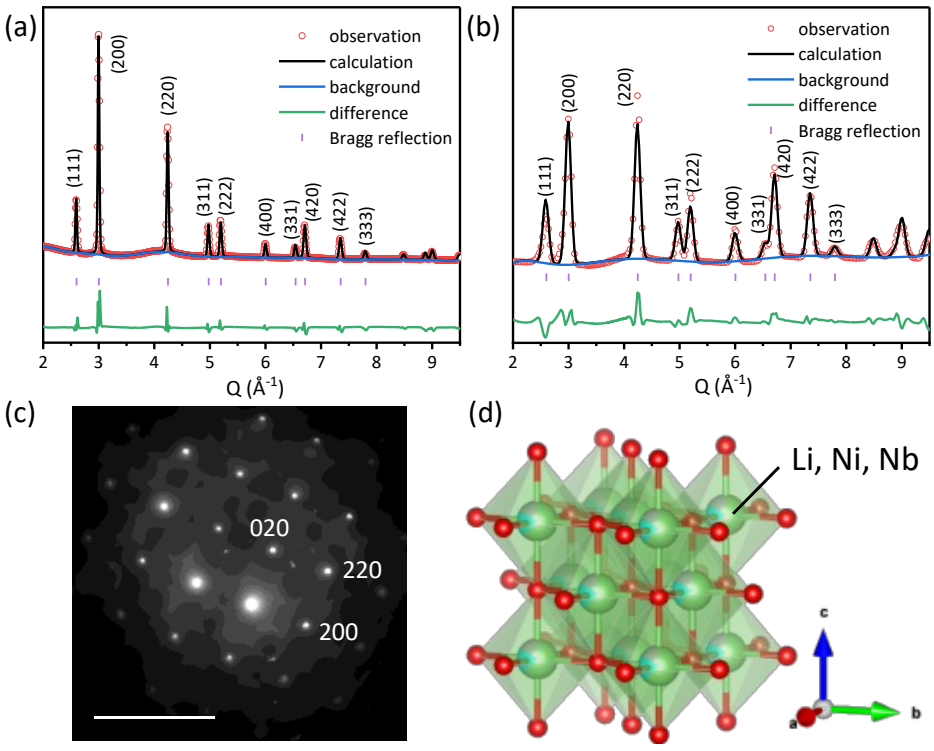

Figure 5.3: Joint Rietveld refinement of (a) PXRD and (b) PND patterns of pristine LNNO,

confirming a single-phase DRX structure with space group $Fm\bar{3}m$. (c) ED pattern along the [001] zone axis showing the characteristic DRX reflections with square spots while the diffuse scattering derives from the local arrangement of Li and TM. (d) Schematic illustration of the pristine LNNO structure, where Li, Ni, and Nb randomly occupy the octahedral sites within the DRX framework.

indexed with space group $Fm\bar{3}m$, without impurity phases or superstructure reflections. The joint refinement results are summarized in **Table 5.2**, yielding the lattice parameter of 4.186 Å. The ED pattern along the [001] zone axis in **Figure 5.3(c)** further confirms the DRX framework, exhibiting sharp square diffraction spots characteristic of cubic symmetry. The diffuse scattering arises from local SRO associated with Li/TM coordination tendencies. The schematic in **Figure 5.3(d)** illustrates the long-range cation disorder, with Li, Ni, and Nb randomly occupying the octahedral 4*a* sites.

Table 5.2: Joint Rietveld refinement result of LNNO.

Atom	Wyckoff site	x	y	z	Uiso	Occ
Li	4*a*	0	0	0	0.00157(42)	0.6400
Ni	4*a*	0	0	0	0.00157(42)	0.1900
Nb	4*a*	0	0	0	0.00157(42)	0.1700
O	4*b*	0.5	0.5	0.5	0.01291(26)	1.0000
Space Group: $Fm\bar{3}m$; wR = 6.37%; GOF = 9.38						
$a = b = c = 4.18602(32)$ Å; $\alpha = \beta = \gamma = 90°$; $V = 73.350(17)$ Å^3						

The electrochemical performance of LNNO was evaluated by galvanostatic cycling at room temperature within a voltage window of 1.5–4.8 V at a current density of 10 mA g^{-1}. The cathode was prepared from pulverized active materials with acetylene black and PTFE. The pulverization process is essential to enhance the kinetics of DRX materials, as discussed in the previous chapter. **Figure 5.4** shows that particle size is significantly reduced (from ~10 μm to ~0.2 μm) after pulverization, without altering the DRX structural

framework.

As presented in **Figure 5.5(a)**, the first charge curve exhibits a steep initial slope followed by a broad sloping region, typical for DRX cathodes. LNNO delivers an initial charge capacity of 278.2 mAh g^{-1} (corresponding to 1.05 Li^{+} removal per formula unit)

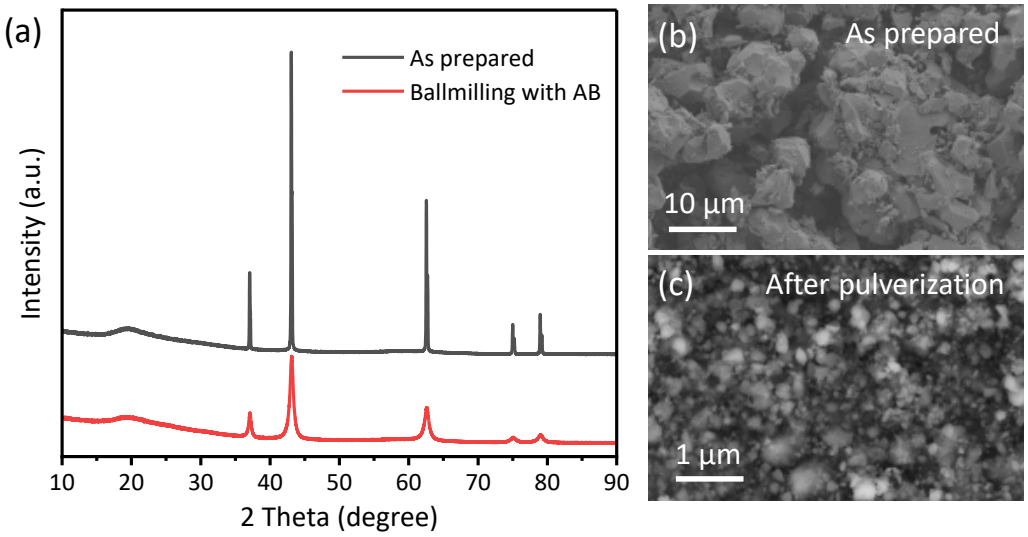

Figure 5.4: (a) XRD patterns of LNNO before and after pulverization (ball milling with acetylene black). (b-c) SEM images of LNNO before and after pulverization.

Figure 5.5: *The figure originally presented here cannot be made freely available via ORA because of pending publication and commercially sensitive information.*

which exceeds the theoretical Ni^{2+}/Ni^{4+} redox capacity of 212.4 mAh g^{-1}. This points to a

significant contribution from oxygen redox at high voltage. The first discharge features a two-stage sloping profile with a moderate hysteresis of ~1 V, resulting in a discharge capacity of 272.2 mAh g^{-1} and an energy density of 769 Wh kg^{-1}. Over 25 cycles (**Figure 5.5(b)**), LNNO shows a gradual and steady capacity fade, retaining 175 mAh g^{-1} after 25 cycles.

Importantly, the voltage hysteresis of LNNO (~1 V) is significantly lower than that of other reported Ni-based DRXs, such as $Li_{1.3}Ni_{0.27}Ta_{0.43}O_2$ (2V), $Li_{1.33}Ni_{0.33}Mo_{0.33}O_2$ (1.9 V) and $Li_{1.2}Ni_{0.33}Ti_{0.33}Mo_{0.13}O_2$ (1.5 V).[16, 23, 24] The origin of this reduced hysteresis will be discussed in the following sections.

5.3.2 Redox Mechanism of LNNO

To elucidate the charge-compensation mechanism of LNNO during cycling, a combination of bulk- and surface-sensitive X-ray spectroscopies was performed for the cycled materials at selected SOCs, as marked in **Figure 5.6(a)**.

The Ni K-edge XANES spectra in transmission mode shown in **Figure 5.6(b)** reveal a clear shift of white line toward higher energies during charging from the pristine state to 4.8 V, indicating progressive oxidation of Ni. Upon discharge, the Ni edge position returns to its original value, confirming a reversible redox process. Compared to Ni standard materials, the highest Ni valence achieved at 4.8 V slightly exceeds +3, suggesting that the Ni^{2+}/Ni^{3+} redox couple is primarily accessed, similar to the reported Ni redox-based DRXs.[23-25] This accounts for roughly half of the theoretical Ni^{2+}/Ni^{4+} redox capacity (~106 mAh g^{-1}). Previous computational studies have shown that cation disorder in DRX materials can raise the Ni^{3+}/Ni^{4+} redox potential,[26] which might explain the incomplete

utilization of Ni redox observed here. The additional capacity observed upon charging must therefore originate from oxygen redox, which will be discussed in the following section.

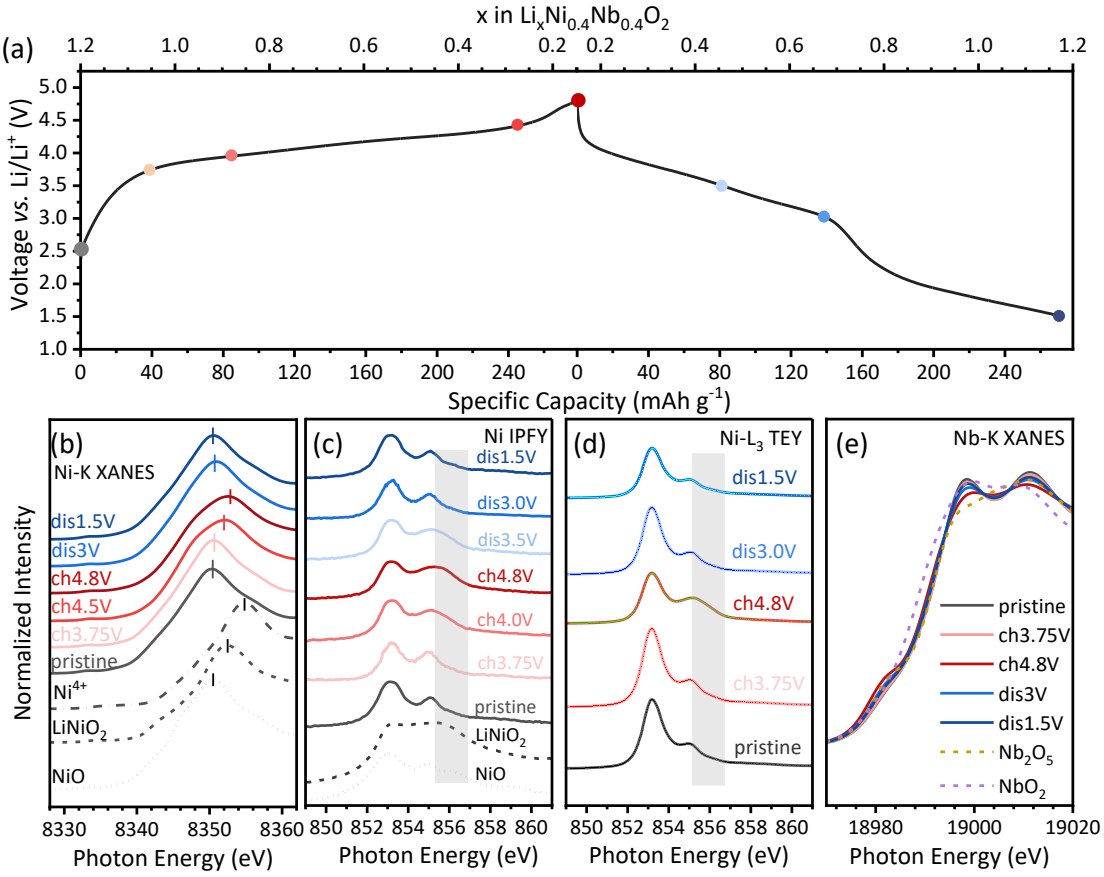

Figure 5.6: (a) First galvanostatic load curve of LNNO (1.5–4.8 V, 10 mA/g), with selected SOCs marked for spectroscopic measurements in **Figure 5.6 and 5.7**. (b) Ni K-edge XANES spectra of LNNO with white lines marked at different SOCs, shown together with reference standards. (c) Ni L-edge IPFY spectra of LNNO revealing the bulk evolution of Ni. (d) Ni L_3-edge TEY spectra of LNNO probing surface-sensitive Ni valence evolution. (e) Nb K-edge XANES of LNNO at various states, confirming that Nb remains in the +5 oxidation state throughout cycling.

To further probe the electronic structure, Ni L_3-edge IPFY spectra (**Figure 5.6(c)**) were collected to track bulk changes in unoccupied Ni 3*d* states without self-absorption effects, while Ni L-edge TEY spectra (**Figure 5.6(d)**) provide complementary surface-sensitive information. Both spectra exhibit a continuous growth of the high-energy component (highlighted in grey) during charging, which reverses upon discharge,

indicating reversible Ni redox process occurring in both the bulk and surface regions.

In contrast, the Nb K-edge XANES (**Figure 5.6(e)**) remain unchanged throughout cycling, with no detectable edge shift or spectral variation. This confirms that Nb maintains its +5 oxidation state as designed and acts strictly as an electrochemically inactive d^0 stabilizer, enabling Ni multi-electron redox without contributing directly to capacity.

The role of oxygen in the electrochemical reaction and the nature of oxidized oxygen species in LNNO were investigated using a combination of XAS, RIXS, EPR and DEMS, as shown in **Figure 5.7**.

The O K-edge PFY spectra (526–534 eV) in **Figure 5.7(a)** reveal bulk-sensitive electronic transitions from O1*s* to O 2*p*–Ni 3*d* hybridized states. A distinct pre-edge feature at ~528.5 eV emerges when charging beyond 4.0 V and grows further upon charging to 4.8 V. In principle, both Ni oxidation and the formation of electron holes (h^+) on O^{2-} (that is, O^{n-} where n<2) can give rise to a pre-edge feature at ~527–530 eV, lower in energy than the main ~531 eV peak corresponding to TM–O anti-bonding bands.[27, 28] However, since Ni oxidation occurs continuously throughout charging in both bulk and surface regions, as evidenced by the IPFY and TEY Ni XAS results in **Figure 5.6**, a solely Ni-driven origin would result in parallel evolution in both PFY and TEY O-K spectra.

Experimentally, however, this ~528.5 eV pre-edge feature appears abruptly only at high voltage and is pronounced in the bulk-sensitive PFY, but is nearly absent in TEY (**Figure 5.7(b)**). This bulk-surface contrast indicates that the feature predominantly arises from bulk-localized O h^+ states, rather than changes in Ni valence.

To further clarify the nature of oxidized oxygen species, *ex-situ* high-resolution RIXS

(**Figure 5.7(c)**) was performed at an excitation energy of 531 eV. Notably, no vibrational

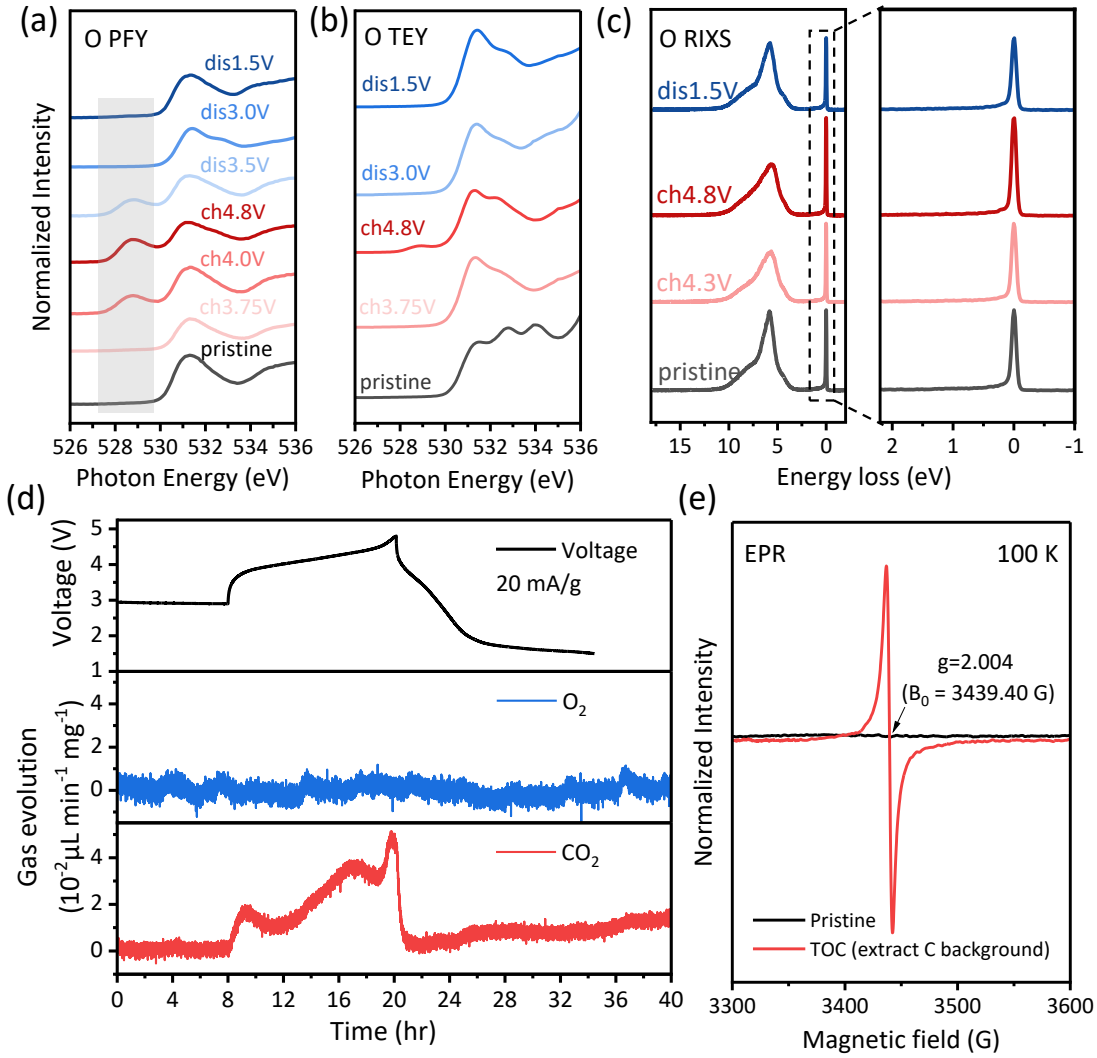

Figure 5.7: Oxygen redox behavior in LNNO during cycling. (a) O K-edge PFY and (b) TEY XAS spectra at selected SOCs, showing evolution of unoccupied O 2*p*-Ni 3*d* hybridized states in the bulk and at the surface, respectively. (c) O K-edge RIXS spectra at an excitation energy of 531 eV for selected SOCs. (d) DEMS profiles of LNNO during the first cycle (1.5–4.8 V, 20 mA g^{-1}), showing the release of O_2 (blue) and CO_2 (red) as a function of time. (e) EPR spectra of pristine LNNO and TOC LNNO (4.8 V) showing oxygen-related radical signatures.

progression peaks associated with O–O dimer formation were observed at TOC, ruling out the formation of molecular O_2 or peroxo-like species within the bulk.[28, 29] DEMS measurements in **Figure 5.7(d)** showed negligible O_2 gas release during the first charge. A minor CO_2 evolution was observed, likely originating from electrolyte decomposition at

the surface.[8, 23]

Finally, *ex-situ* EPR spectra provide additional evidence for the formation of electron-hole (h^+) states on oxygen, as displayed in **Figure 5.7(e)**. The charged sample (TOC at 4.8 V) displays a pronounced g ≈ 2.004 signal, characteristic of paramagnetic O-centered radical species (O^{n-}), which are absent in the pristine sample.[30-32] Given that O–O dimer formation has been excluded by RIXS, this EPR result confirms the generation of O h^+ states at high voltage.

In summary, LNNO exhibits a cooperative Ni–O redox mechanism that underpins its high capacity beyond the theoretical Ni redox limit. Ni redox occurs reversibly in both bulk and surface throughout cycling, while bulk lattice oxygen redox, enabled by strong O 2*p*–Ni 3*d* hybridization, provides additional capacities at high voltages. Importantly, oxygen redox proceeds without significant O_2 gas release or peroxo-like dimer formation, facilitating lattice integrity and cycling stability.

5.3.3 Structure and Electrochemistry of LNWO

The chemical composition of LNWO, with W^{6+} serving as the high-valent charge compensator, was determined by ICP-OES (**Table 5.1**) as $Li_{1.20}Ni_{0.49}W_{0.31}O_2$. EDX mappings (**Figure 5.8**) uniform distribution of all constituent elements across the particles.

The crystal structure of pristine LNWO was analyzed using combined PXRD and PND to verify the formation of a DRX phase. As shown in **Figures 5.9(a–b)**, joint Rietveld refinement confirmed that LNWO adopts a single-phase DRX structure indexed with space group $Fm\bar{3}m$ (a= 4.147 Å, see **Table 5.3)** with no evidence of secondary phases or cation ordering reflections.

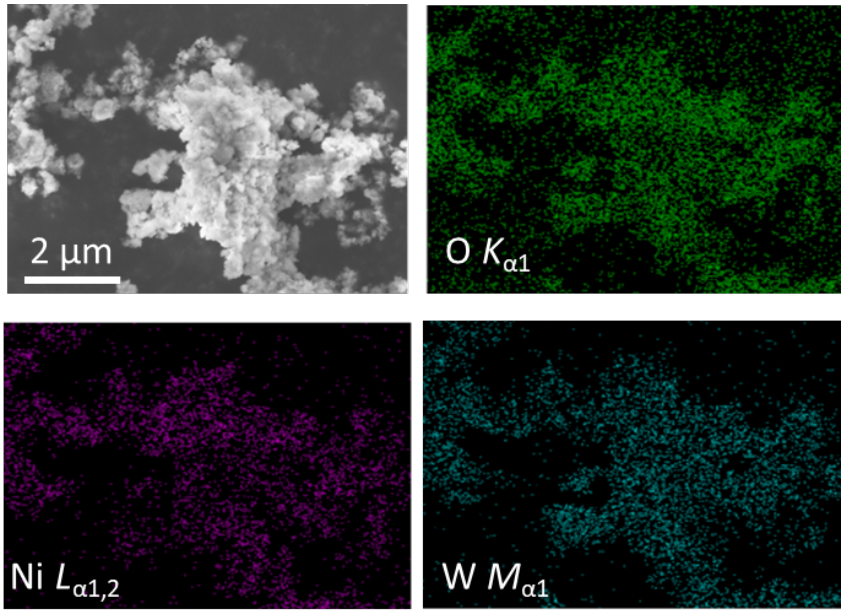

Figure 5.8: SEM image and EDX mappings of LNWO.

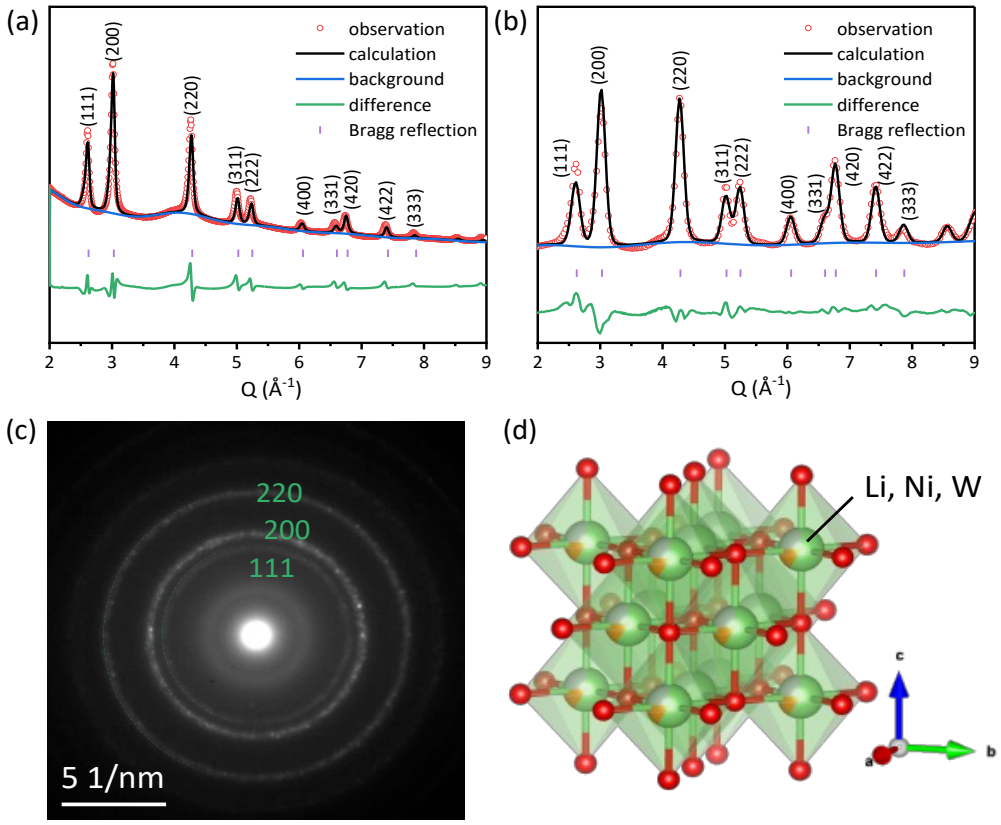

Figure 5.9: Joint Rietveld refinement of (a) PXRD and (b) PND patterns for LNWO, confirming a single-phase DRX structure of space group $Fm\bar{3}m$. (c) ED pattern of LNWO, exhibiting diffraction rings indexed to (111), (200), and (220) planes. (d) Schematic of the pristine LNWO structure, where Li, Ni, and W randomly occupy octahedral 4*a* sites.

Table 5.3: Joint Rietveld refinement results of LNWO.

Atom	Wyckoff site	x	y	z	Uiso	Occ
Li	4*a*	0	0	0	0.02026(58)	0.5980
Ni	4*a*	0	0	0	0.02026(58)	0.2460
W	4*a*	0	0	0	0.02026(58)	0.1550
O	4*b*	0.5	0.5	0.5	0.01296(19)	1.0000

Space Group: $Fm\bar{3}m$; wR = 4.23%; GOF = 6.65
$a = b = c = 4.14712(48)$ Å; $\alpha = \beta = \gamma = 90°$; $V = 71.325(24)$ Å^3

ED pattern collected along the [001] zone axis, show in **Figure 5.9(c)**, displays continuous diffraction rings, characteristic of highly polycrystalline DRX materials with nanoscale particle size. This morphology is further confirmed by SEM imaging in **Figure 5.8** The schematic in **Figure 5.9(d)** illustrates the long-range cation disorder, where Li, Ni, and W are randomly distributed on the octahedral 4*a* sites, consistent with the inherent configurational disorder of DRX phases.

To evaluate the electrochemical properties of LNWO, galvanostatic cycling was performed within a voltage window of 1.5–4.8 V at a current density of 10 mA g^{-1}. Pulverized active material blended with acetylene black was used as the cathode. **Figure 5.10** shows SEM images of LNWO before and after pulverization, indicating that while primary particle size remains nearly unchanged, aggregation results in larger secondary particles. The DRX phase of LNWO retained after pulverization.

The first cycle charge–discharge profile, shown in **Figure 5.11(a)**, exhibits a sloping shape typical of DRX cathodes. The initial charge capacity reached 243.6 mAh g^{-1}, corresponding to the extraction of approximately 1.15 Li^+ per formula unit, slightly exceeding the theoretical Ni^{2+}/Ni^{4+} redox capacity of 214.7 mAh g^{-1}. The first discharge

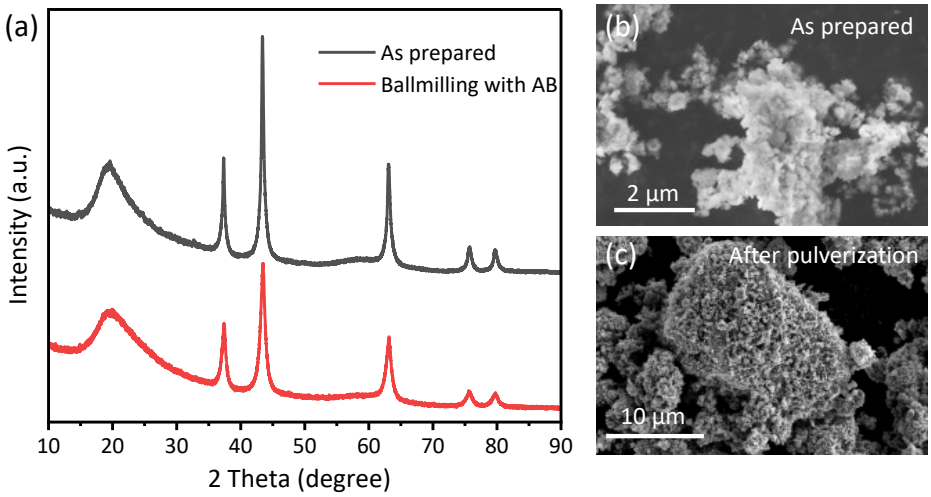

Figure 5.10: (a) XRD patterns of LNWO before and after pulverization (ball milling with acetylene black). (b-c) SEM images of LNWO before and after pulverization.

capacity was 203.2 mAh g^{-1}, delivering an initial energy density of 474.6 Wh kg^{-1}. Compared with LNNO, the discharge profile of LNWO exhibits a noticeably larger voltage hysteresis (2.3 V), implying increased polarization and slower reaction kinetics.[24]

Figure 5.11: *The figure originally presented here cannot be made freely available via ORA because of pending publication and commercially sensitive information.*

The cycling stability is presented in **Figure 5.11(b)**. LNWO undergoes a mild activation process during the first five cycles, where the discharge capacity gradually rises before entering a steady decline. After 25 cycles, the capacity drops to ~75 mAh g^{-1},

demonstrating much poorer cycling stability than LNNO. The limited reversibility of LNWO is explored in the following sections.

5.3.4 Redox Mechanism of LNWO

Figure 5.12 demonstrates the TM redox behavior in LNWO during the first cycle. As shown in **Figure 5.12(a)**, the first charge–discharge profile highlights the SOCs at which *ex-situ* spectroscopic analyses were conducted. The Ni K-edge XANES spectra in transmission mode, shown in **Figure 5.12(b)**, display a shift of the white line to higher energies upon charging. Comparison with standard references (NiO and $LiNiO_2$) confirms that Ni was oxidized from +2 in the pristine state to just below +3 at TOC, signifying a lower degree of Ni redox utilization in LNWO compared to LNNO. The Ni L_3-edge sXAS spectra in IPFY mode (**Figure 5.12(c)**), which provides shallower probing depth than transmission XANES, exhibit only minor spectral evolution during cycling. This subdued Ni redox signature may be attributed to partial TM reduction and surface densification associated with O_2 gas release, as reported previously.[23] Further discussion and supporting evidence for this hypothesis are provided in the next section. Upon discharge, the Ni edge returns toward its initial position, consistent with a largely reversible Ni^{2+}/Ni^{3+} redox process. The W L_3-edge XANES spectra, presented alongside a WO_3 standard in **Figure 5.12(d)**, remain unchanged throughout the cycle, confirming that W^{6+} functions as a redox-inactive charge compensator in LNWO.

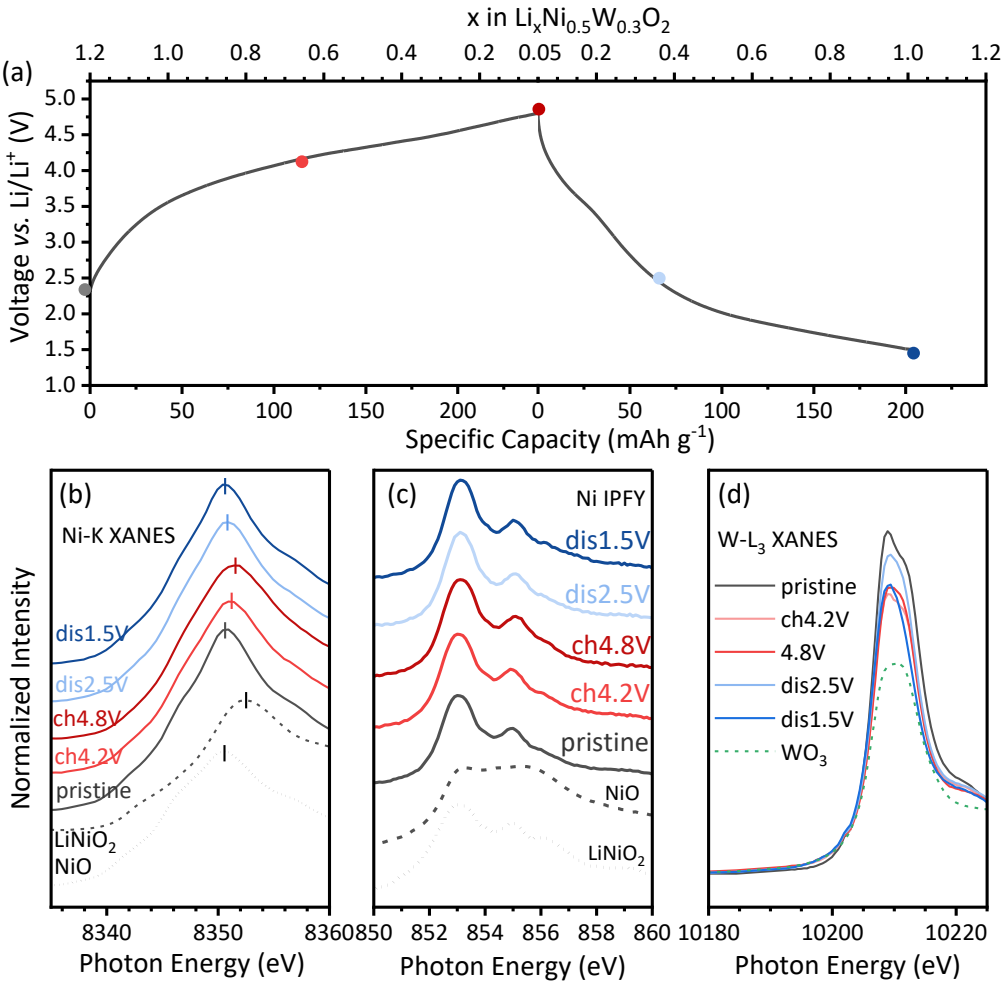

Figure 5.12: (a) First galvanostatic load curve of LNWO (1.5–4.8 V, 10 mA g^{-1}), with selected SOCs marked for spectroscopic measurements in **Figure 5.12 and 5.13**. (b) Ni K-edge XANES spectra of LNWO with white lines marked at different SOCs, shown together with reference standards. (c) Ni L-edge IPFY spectra of LNWO. (d) W L_3-edge XANES spectra confirming that W remains in the +6 oxidation state throughout cycling.

The oxygen redox activity in LNWO was systematically investigated in **Figure 5.13**. The *ex-situ* O K-edge PFY spectra (**Figure 5.13a)**) show a weak pre-edge feature at ~529 eV before the leading edge emerging at TOC (charged to 4.8 V), with noticeably lower intensity compared to LNNO. This indicates limited formation of electron holes (h^+) on individual oxide ions at high voltage.[27, 33] The evolution of the main absorption edge was subtle. For better visualization, the difference spectrum between TOC and pristine was

plotted in purple, revealing two principal peaks at ~530.2 eV and ~532.8 eV. The intensity increase at 530.2 eV is ascribed to Ni oxidation, in line with the Ni XANES results. The emerging feature at 532.8 eV correponds to transitions into antibonding (O–O)* orbitals which occur when lattice oxygen is oxidized beyond the stability of the rigid structure and begins to pair up with neighboring O atoms to lower the system energy at the cost of structural distortion (O–O distance shortening).[29, 34, 35]

Despite the presence of this feature, RIXS spectra in **Figure 5.13(b)** show no evidence of vibrational progression peaks at TOC that would indicate the formation of stable O–O dimers within the bulk.[28, 36] This absence suggests that any O–O dimers formed during charging are transient and likely escape from the open DRX structure as molecular O_2 gas,[33] rather than persisting as stabilized peroxo-like or molecular oxygen species within the bulk lattice. This interpretation is reinforced by the DEMS data in **Figure 5.13(c)**, which reveals the onset of O_2 gas release at ~4.4 V, with continuous accumulation during further charging to TOC, resulting in a total oxygen loss of ~4 μL/mg (equivalent to 2.4% oxygen loss). This is quite different from LNNO where there is no O_2 evolution. Concurrent, continuous CO_2 evolution is also observed during charging, likely stemming from electrolyte decomposition at elevated potentials.[23, 25]

Together, these results show that in LNWO, Ni redox utilization is limited, and oxygen redox dominates the high-voltage capacity. However, the oxidized oxygen is unstable, resulting in O_2 gas release rather than reversible lattice oxygen redox, ultimately leading to significant voltage hysteresis and poor cycling stability.[37, 38]

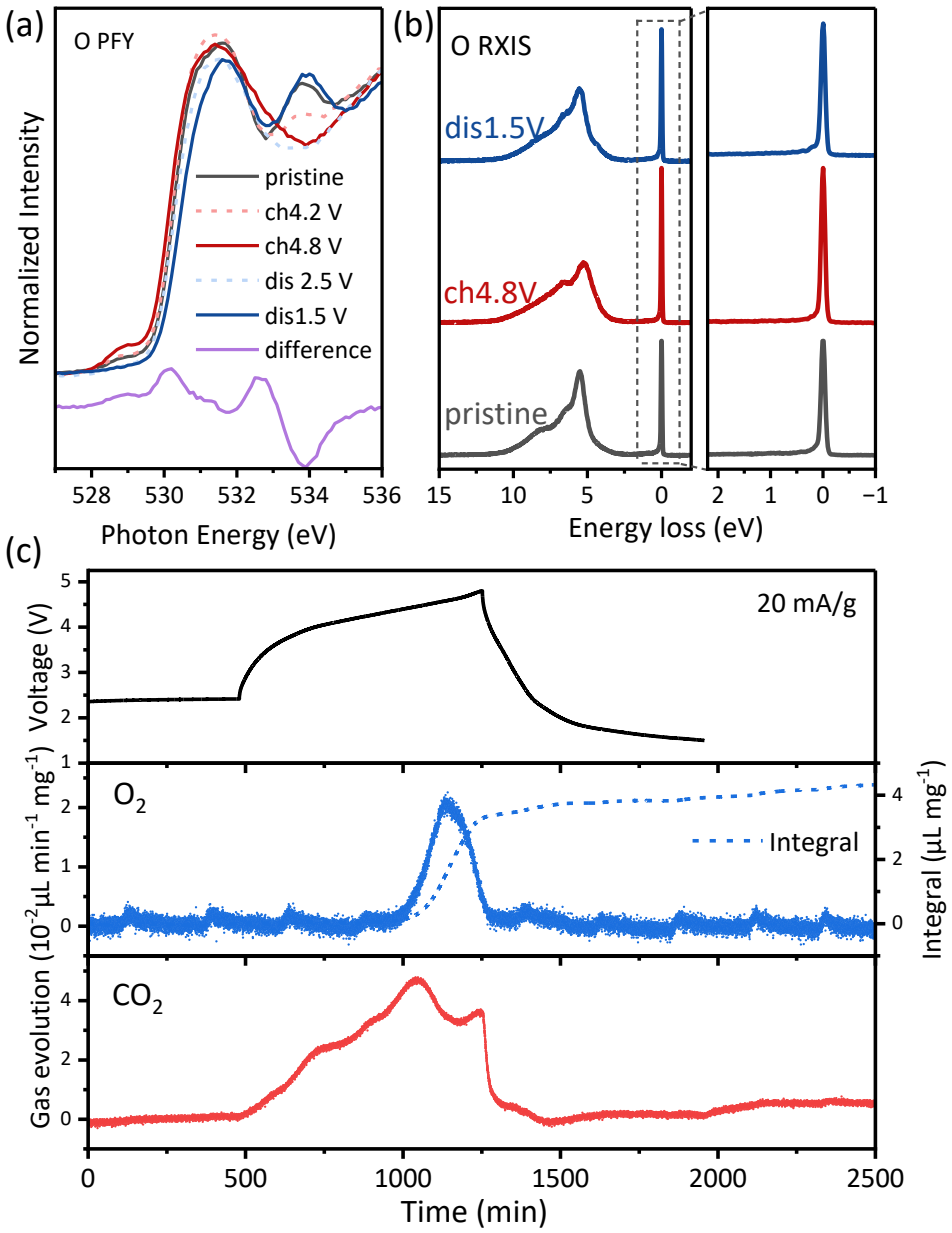

Figure 5.13: Oxygen redox behavior in LNWO during cycling. (a) O K-edge PFY XAS spectra at selected SOCs together with the difference between pristine and TOC (purple) for clear comparison. (b) O K-edge RIXS spectra at an excitation energy of 531 eV for selected SOCs. (c) DEMS profiles of LNWO during the first cycle (1.5–4.8 V, 20 mA g^{-1}), showing the release of O_2 and integrated volume (blue) together with release of CO_2 (red) as a function of time.

5.3.5 Band Structure Driven Redox Chemistry

The experimental results reveal that, despite having similar lithium content and initial Ni valence, LNNO and LNWO exhibit markedly different electrochemical profiles and

redox mechanisms. As shown in **Figure 5.14**, LNNO displays a significantly lower voltage hysteresis and superior cycling stability compared to LNWO. In LNNO, both Ni and O redox processes contribute substantially to the capacity, with electron holes (h^+) formed on O enabling reversible oxygen redox at high potential and minimal hysteresis (that is, O^{n-} can be reduced at high potential). In contrast, LNWO, after limited Ni redox activity, relies heavily on oxygen redox for capacity; however, the oxidized oxygen is unstable, readily forms transient O–O dimers, and escapes as O_2 gas, resulting in pronounced hysteresis and poor cycling stability.

Figure 5.14: *The figure originally presented here cannot be made freely available via ORA because of pending publication and commercially sensitive information.*

The fundamental origins of these distinctions lie in the intrinsic band structure and cation chemistry for LNNO and LNWO. As depicted in **Figure 5.15(a)**, the Li-rich DRX structure features a 6-coordinated oxygen environment. Since the cations are randomly distributed in the same 4*a* sites with 60% of Li, majority of oxygen have a 2*p* orbital that is weakly bonded due to the small overlap with the Li 2*s* orbital, resulting in the emergence of O 2*p* non-bonding states (O_{NB}) in the band structure.[39] These states are

situated just above the bonding (M–O) band and below the antibonding (M–O)* band, playing a crucial role in charge compensation at high states of delithiation.

The schematic band diagrams for LNNO and LNWO in **Figures 5.15(b–c)** illustrate how d^0 metal selection (Nb^{5+} in LNNO *vs*. W^{6+} in LNWO) fundamentally alters the electronic structure and, consequently, oxygen redox chemistry.[40, 41] Within the Mott–Hubbard framework, the TM *d* band splits into upper and lower Hubbard bands (UHB and LHB), where *U* (*d*-*d* Coulomb interaction term) describes the on-site electron repulsion within the *d* orbitals. Δ (charge transfer term) is the effective energy difference between TM *d* levels and O 2*p* levels, which is closely related to the electronegativity difference between TM and O (electronegativity of 3.44).[39]

In the DRX structure, all cations occupy equivalent crystallographic sites, in contrast to layered materials where TMs and Li reside in alternating layers with the Li layer serving as a "buffer".[23] This structural arrangement in DRXs leads to stronger repulsive interactions between neighboring TMs, resulting in a relatively larger *U* compared to layered frameworks. Especially in the present case of half-filled Ni^{2+} ($t_{2g}^6e_g^2$) with strong electronic stabilization (displaying large *U*),[23] the magnitude of Δ becomes a critical parameter that determines the alignment of the O_{NB} states with respect to the LHB of the TM *d* states.

The relative position of O_{NB} and LHB dictates the competition and interplay between Ni and O redox processes. When Δ is large, as in Nb^{5+}-substituted LNNO (with Nb electronegativity of 1.6), the O_{NB} overlaps with the bottom of LHB,[41] enabling a sequential redox process: Ni oxidation occurs first, followed by reversible bulk oxygen redox at higher potentials. This sequential mechanism is facilitated by strong O 2*p*–Ni 3*d* hybridization,

which stabilizes electron holes (h^+) on oxygen, suppresses O–O dimerization, and minimizes lattice oxygen loss. These features explain LNNO's low voltage hysteresis and superior cycling stability, as confirmed by spectroscopy and DEMS.

In contrast, a smaller Δ found in W^{6+}-substituted LNWO (with W electronegativity of 2.36) shifts the O_{NB} closer to the LHB, resulting in significant overlap and direct competition between Ni and O redox.[40] This electronic landscape limits Ni oxidation, destabilizes oxidized oxygen species, and favors the formation and rapid loss of O–O dimers as O_2 gas. Consequently, LNWO exhibits larger voltage hysteresis, poorer reversibility, and accelerated capacity fade, consistent with XAS and DEMS observations.

Figure 5.15: *The figure originally presented here cannot be made freely available via ORA because of pending publication and commercially sensitive information.*

5.4 Conclusion

In this chapter, the impact of high-valent d^0 cation selection on the electrochemical

and redox behavior of Ni-based DRX cathode materials was systematically investigated through a comparative study of LNNO and LNWO. Comprehensive structural characterizations confirmed that both LNNO and LNWO adopt single-phase DRX structures without long-range secondary phases. Despite their similar Li content and initial Ni valence, the two materials exhibited markedly different electrochemical properties and charge compensation mechanisms.

LNNO demonstrates a cooperative Ni–O redox process, in which enhanced utilization of Ni redox is coupled with reversible lattice oxygen redox at high voltage. In this case, oxygen redox proceeds through the formation of O-centered holes (O^{n-}, $n<2$) without triggering O–O dimerization or significant O_2 gas release, resulting in high reversible capacity, low voltage hysteresis, and superior cycling stability compared to other Ni-based DRX cathodes.

By contrast, LNWO shows limited Ni redox utilization and severer voltage hysteresis. Oxygen redox in LNWO is associated with unstable oxidized oxygen species that readily dimerize and tend to be released as O_2 gas, leading to rapid capacity fading and structural deterioration. The comparative band-structure analysis indicates that the higher electronegativity of W reduces the charge-transfer gap (Δ), shifts the oxygen non-bonding states closer to the lower Hubbard band, and thereby destabilizes lattice oxygen while intensifying direct competition between Ni and O redox.

More broadly, this study provides new insight into the design of Ni-based DRX cathodes. While prevailing strategies for DRX materials often treat high-valent d^0 cations primarily as charge compensators or structural stabilizers, the present results show that their

electronic character can fundamentally reshape the balance between TM redox and oxygen redox. In other words, the identity of the charge-compensating d^0 cation is not merely a structural variable, but also an electronic design parameter that governs redox reversibility, voltage hysteresis, and oxygen stability.

From a materials-design perspective, these findings establish an alternative strategy for developing high-capacity, low-hysteresis DRX cathodes: rather than simply suppressing oxygen redox in favor of TM redox, it is possible to realize stabilized and reversible oxygen redox through careful selection of the high-valent substituent and deliberate tuning of the electronic landscape. This provides a broader framework for designing next-generation DRX cathodes that simultaneously achieve high reversible capacity, minimal oxygen loss, and improved cycling stability.

5.5 References

1. R. J. Clément, Z. Lun and G. Ceder, *Energy & Environmental Science*, 2020, **13**, 345-373.

2. H. M. Hau, T. Holstun, E. Lee, B. L. D. Rinkel, T. P. Mishra, M. M. DiPrince, R. S. Mohanakrishnan, E. C. Self, K. A. Persson, B. D. McCloskey and G. Ceder, *Advanced Materials*, 2025, 2502766.

3. Z. Lun, B. Ouyang, D. H. Kwon, Y. Ha, E. E. Foley, T. Y. Huang, Z. Cai, H. Kim, M. Balasubramanian and Y. Sun, *Nature Materials*, 2021, **20**, 214-221.

4. N. Yabuuchi, K. Kubota, M. Dahbi and S. Komaba, *Chemical Reviews*, 2014, **114**, 11636-11682.

5. W. E. Gent, K. Lim, Y. Liang, Q. Li, T. Barnes, S. J. Ahn, K. H. Stone, M. McIntire, J. Hong, J. H. Song, Y. Li, A. Mehta, S. Ermon, T. Tyliszczak, D. Kilcoyne, D. Vine, J. H. Park, S. K. Doo, M. F. Toney, W. Yang, D. Prendergast and W. C. Chueh, *Nature Communications*, 2017, **8**, 2091.

6. D. H. Kwon, J. Lee, N. Artrith, H. Kim, L. Wu, Z. Lun, Y. Tian, Y. Zhu and G. Ceder, *Cell Reports Physical Science*, 2020, **1**, 100187.

7. J. Burns and K. A. Persson, *Chemistry of Materials*, 2023, **35**, 9127-9134.

8. J. Lee, J. K. Papp, R. J. Clément, S. Sallis, D. H. Kwon, T. Shi, W. Yang, B. D. McCloskey and G. Ceder, *Nature Communications*, 2017, **8**, 981.

9. X. Xu, L. Pi, J. J. Marie, G. J. Rees, C. Gong, S. Pu, R. A. House, A. W. Robertson and P. G. Bruce, *Journal of the Electrochemical Society*, 2021, **168**, 080521.

10. J. C. Knight and A. Manthiram, *Journal of Materials Chemistry A*, 2015, **3**, 22199-22207.

11. M. Juelsholt, J. Chen, M. A. Pérez-Osorio, G. J. Rees, S. De Sousa Coutinho, H. E. Maynard-Casely, J. Liu, M. Everett, S. Agrestini, M. Garcia-Fernandez, K. J. Zhou, R. A. House and P. G. Bruce, *Energy & Environmental Science*, 2024, **17**, 2530-2540.

12. W. D. Richards, S. T. Dacek, D. A. Kitchaev and G. Ceder, *Advanced Energy Materials*, 2018, **8**, 1701533.

13. L. Croguennec, J. Bains, M. Ménétrier, A. Flambard, E. Bekaert, C. Jordy, P. Biensan and C. Delmas, *Journal of the Electrochemical Society*, 2009, **156**, A349.

14. R. Chen, S. Ren, M. Knapp, D. Wang, R. Witter, M. Fichtner and H. Hahn, *Advanced Energy Materials*, 2015, **5**, 1401814.

15. R. A. House, L. Jin, U. Maitra, K. Tsuruta, J. W. Somerville, D. P. Förstermann, F. Massel, L. Duda, M. R. Roberts and P. G. Bruce, *Energy & Environmental Science*, 2018, **11**, 926-932.

16. N. Yabuuchi, Y. Tahara, S. Komaba, S. Kitada and Y. Kajiya, *Chemistry of Materials*, 2016, **28**, 416-419.

17. N. Yabuuchi, M. Takeuchi, M. Nakayama, H. Shiiba, M. Ogawa, K. Nakayama, T. Ohta, D. Endo, T. Ozaki, T. Inamasu, K. Sato and S. Komaba, *Proceedings of the National Academy of Sciences of the United States of America*, 2015, **112**, 7650-7655.

18. Y. Zhou, Y. Xu, H. Feng, J. Song, M. Yan, H. Jian, F. Zhuge and Q. Tan, *Journal of Materials Science*, 2023, **58**, 14440-14451.

19. B. H. Toby and R. B. Von Dreele, *Journal of Applied Crystallography*, 2013, **46**, 544-549.

20. C. L. Farrow, P. Juhas, J. W. Liu, D. Bryndin, E. S. Božin, J. Bloch, T. Proffen and S. J. L. Billinge, *Journal of Physics: Condensed Matter*, 2007, **19**, 335219.

21. C. Schulz, K. Lieutenant, J. Xiao, T. Hofmann, D. Wong and K. Habicht, *Synchrotron Radiation*, 2020, **27**, 238-249.

22. S. Stoll and A. Schweiger, *Journal of Magnetic Resonance*, 2006, **178**, 42-55.

23. Q. Jacquet, A. Iadecola, M. Saubanère, H. Li, E. J. Berg, G. Rousse, J. Cabana, M. L. Doublet and J. M. Tarascon, *Journal of the American Chemical Society*, 2019, **141**, 11452-11464.

24. J. Lee, D. H. Seo, M. Balasubramanian, N. Twu, X. Li and G. Ceder, *Energy & Environmental Science*, 2015, **8**, 3255-3265.

25. M. A. Cambaz, A. Urban, S. A. Pervez, H. Geßwein, A. Schiele, A. A. Guda, A. L. Bugaev, A. Mazilkin, T. Diemant, R. J. Behm, T. Brezesinski and M. Fichtner, *Chemistry of Materials*, 2020, **32**, 3447-3461.

26. A. Abdellahi, A. Urban, S. Dacek and G. Ceder, *Chemistry of Materials*, 2016, **28**, 3659-3665.

27. J. J. Marie, M. Jenkins, J. Chen, G. Rees, V. Cellorio, J. Choi, S. Agrestini, M. Garcia-Fernandez, K. J. Zhou, R. A. House and P. G. Bruce, *Advanced Energy Materials*, 2024, **14**, 2401935.

28. R. A. House, U. Maitra, M. A. Perez-Osorio, J. G. Lozano, L. Jin, J. W. Somerville, L. C. Duda, A. Nag, A. Walters, K. J. Zhou, M. R. Roberts and P. G. Bruce, *Nature*, 2020, **577**, 502-508.

29. R. A. House, G. J. Rees, M. A. Pérez-Osorio, J. J. Marie, E. Boivin, A. W. Robertson, A. Nag, M. Garcia-Fernandez, K. J. Zhou and P. G. Bruce, *Nature Energy*, 2020, **5**, 777-785.

30. H. Liu, C. Li, C. Zhao, W. Tong and B. Hu, *Energy Storage Materials*, 2022, **50**, 55-62.

31. M. Sathiya, J. B. Leriche, E. Salager, D. Gourier, J. M. Tarascon and H. Vezin, *Nature Communications*, 2015, **6**, 6276.

32. M. Tang, A. Dalzini, X. Li, X. Feng, P. H. Chien, L. Song and Y. Y. Hu, *The Journal of Physical Chemistry Letters*, 2017, **8**, 4009-4016.

33. T. Matsuhara, Y. Tsuchiya, K. Yamanaka, K. Mitsuhara, T. Ohta and N. Yabuuchi, *Electrochemistry*, 2016, **84**, 797-801.

34. M. Saubanère, E. McCalla, J. M. Tarascon and M. L. Doublet, *Energy & Environmental Science*, 2016, **9**, 984-991.

35. J. Hong, W. E. Gent, P. Xiao, K. Lim, D. H. Seo, J. Wu, P. M. Csernica, C. J. Takacs, D. Nordlund, C. J. Sun, K. H. Stone, D. Passarello, W. Yang, D. Prendergast, G. Ceder, M. F. Toney and W. C. Chueh, *Nature Materials*, 2019, **18**, 256-265.

36. R. Sharpe, R. A. House, M. J. Clarke, D. Forstermann, J. J. Marie, G. Cibin, K. J. Zhou, H. Y. Playford, P. G. Bruce and M. S. Islam, *Journal of the American Chemical Society*, 2020, **142**, 21799-21809.

37. R. A. House, J. J. Marie, M. A. Pérez-Osorio, G. J. Rees, E. Boivin and P. G. Bruce, *Nature Energy*, 2021, **6**, 781-789.

38. K. McColl, R. A. House, G. J. Rees, A. G. Squires, S. W. Coles, P. G. Bruce, B. J. Morgan and M. S. Islam, *Nature Communications*, 2022, **13**, 5275.

39. G. Assat and J. M. Tarascon, *Nature Energy*, 2018, **3**, 373-386.

40. D. Errandonea, F. Rodriguez, R. Vilaplana, D. Vie, S. Garg, B. Nayak, N. Garg, J. Singh, V. Kanchana and G. Vaitheeswaran, *The Journal of Physical Chemistry C*, 2023, **127**, 15630-15640.

41. S. Chakrabarti and A. K. Thakur, *Ionics*, 2025, **31**, 9041-9059.